Implementation of Adaptive Filter Algorithms for the Suppression of Thermoacoustic Instabilities

by

Aaron Greenwood

Thesis submitted to the faculty of Virginia Polytechnic Institute and State University in partial fulfillment of the requirements for the degree of

Master of Science in Mechanical Engineering

Committee Members

William R. Saunders
William T. Baumann
Donald J. Leo

February 5, 2003
Blacksburg, Virginia

Keywords: Thermoacoustic instability, active combustion control, adaptive filters, optimization

Implementation of Adaptive Filter Algorithms for the Suppression of Thermoacoustic Instabilities

Aaron Greenwood
Virginia Polytechnic Institute and State University
Advisor: William R. Saunders, Chair

Abstract:

The main goal of this work was to develop adaptive filter algorithms and test their performance in active combustion control. Several algorithms were incorporated, which are divided into gradient descent algorithms and pattern searches.

The algorithms were tested on three separate platforms. The first was an analog electronic simulator, which uses a second order acoustics model and a first order low pass filter to simulate the flame dynamics of an unstable tube combustor. The second was a flat flame, methane-air Rijke tube. The third can be considered a quasi-LDI liquid fuel combustor with a thermal output of approximately 30 kW.

Actuation included the use of an acoustic actuator for the Rijke tube and a proportional throttling valve for the liquid fuel rig. Proportional actuation, pulsed actuation, and subharmonic control were all investigated throughout this work.

The proportional actuation tests on the Rijke tube combustor have shown that, in general, the gradient descent algorithms outperformed the pattern search algorithms. Although, the pattern search algorithms were able to suppress the pressure signal to levels comparable to the gradient descent algorithms, the convergence time was lower for the gradient descent algorithms. The gradient algorithms were also superior in the presence of actuator authority limitations.

The pulsed actuation on the Rijke tube showed that the convergence time is decreased for this type of actuation. This is due to the fact that there is a fixed amplitude control signal and algorithms did not have to search for sufficient magnitude. It was shown that subharmonic control could be used in conjunction with the algorithms. Control was achieved at the second and third subharmonic, and control was maintained for much higher subharmonics.

The cost surface of the liquid fuel rig was obtained as the mean squared error of the combustor pressure as a function of the magnitude and phase of the controller. The adaptive algorithms were able to achieve some suppression of the pressure oscillations but did not converge to the optimal phase as shown in the cost surface. Simulations using the data from this cost surface were also performed. With the addition of a probing function, the algorithms were able to converge to a near-optimal condition.

Acknowledgements

I would like to acknowledge all those who have made this work possible.

No teacher in my career has had a larger influence on my development than Dr. Saunders. He has always had an open door for questions, comments, or discussion, which has made my experience in Blacksburg truly rewarding.

Dr. Baumann is one of the most knowledgeable and inquisitive engineers that I have met. His guidance on this work has been greatly appreciated.

Dr. Leo's control classes were some of the most insightful and rewarding classes that I have taken throughout college.

I would also like to thank Dr. Vandsburger, Dr. West, and the rest of the VACCG. I have been lucky to join such a group of intelligent and friendly engineers.

Finally, I would like to thank my family for their support during this process and throughout my life. Everything that I have and will accomplish is a direct reflection of their unending love and encouragement.

Table of Contents

List of Figures

List of Tables

Chapter 1 Introduction

This work considers active combustion control algorithms that do not rely on system models and have potential for suppressing thermoacoustic instabilities in gas turbine engines using non-model based techniques. Other members of the Virginia Active Combustion Control Group (VACCG) are currently exploring active control using models based on system identification theory. The suppression of thermoacoustic instabilities in this work is actuated by either a speaker or by the modulation of liquid fuel. Thus, the capability for both proportional and pulsed actuation is present. The control signal is constructed using several adaptive filtering algorithms that optimize the coefficients of an FIR filter.

1.1 Background

Recently, there has been a concerted effort to lower toxic emissions from the combustion process in gas turbine engines. One step that has been taken is running at leaner conditions. While this is successful in lowering the amount of NO_x and other pollutants emitted, it also promotes combustion instabilities. These instabilities are a result of a self-excited loop formed between heat release rate and pressure oscillations within a combustor. Figure 1.1 shows a block-diagram representation of the loop. This system is linearly unstable, but ultimately settles into a stable limit cycle due to nonlinearities in the heat release dynamics.

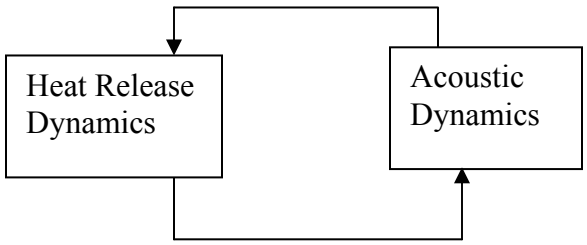

Figure 1.1 Self-excited loop

The interaction between heat release and pressure, which is the most common interaction causing acoustic instability, was described by Lord Rayleigh in the late 1800s. A brief discussion of the Rayleigh criterion is provided in the following section.

1.2 Rayleigh's Criterion

In 1878 Lord Rayleigh proposed a simple criterion for the presence of thermoacoustic instabilities, which involved unsteady pressure oscillations and the rate of change of heat release from a flame. He determined that if heat is added during the compression cycle of a standing acoustic wave or removed during expansion, the oscillations are amplified. If, however, the heat is added during expansion or removed during compression, the oscillations are discouraged. Simply stated, thermoacoustic instabilities are dependent on the relative phase between heat release rate and pressure oscillations.

Rayleigh's criterion can be expressed mathematically by introducing the Rayleigh index, G(x),

$$G(x) = \frac{1}{T}\int_{T} q'(x,t)\,p'(x,t)dt$$

where T is the period of oscillation, p' is the local pressure oscillation, and q' is the unsteady heat release rate. Oscillations are encouraged for field variables that exhibit positive values of the Rayleigh index and discouraged for negative values. This requires that q' and p' must be in-phase for an instability to be present.

In practice, thermoacoustic instabilities are quite undesirable. However, for this work it was necessary to have an unstable combustor to test the performance in suppressing the instability. Rayleigh's criterion was used in the design of the tube combustors involved in this work. The first of the combustors was a pre-mixed methane-air Rijke tube that was acoustically closed at the bottom and open at the top. The flame in this combustor was located at one-half the length of the tube, as consistent with Rayleigh's criterion discussed below. The system was actuated by a 3" speaker. A picture of the tube is shown in Figure 1.2. The second combustor was also a closed-open tube, which was fueled by liquid kerosene and actuated by a throttling valve, which modulated the fuel flow. More details of this combustor are given in Section 5.6.

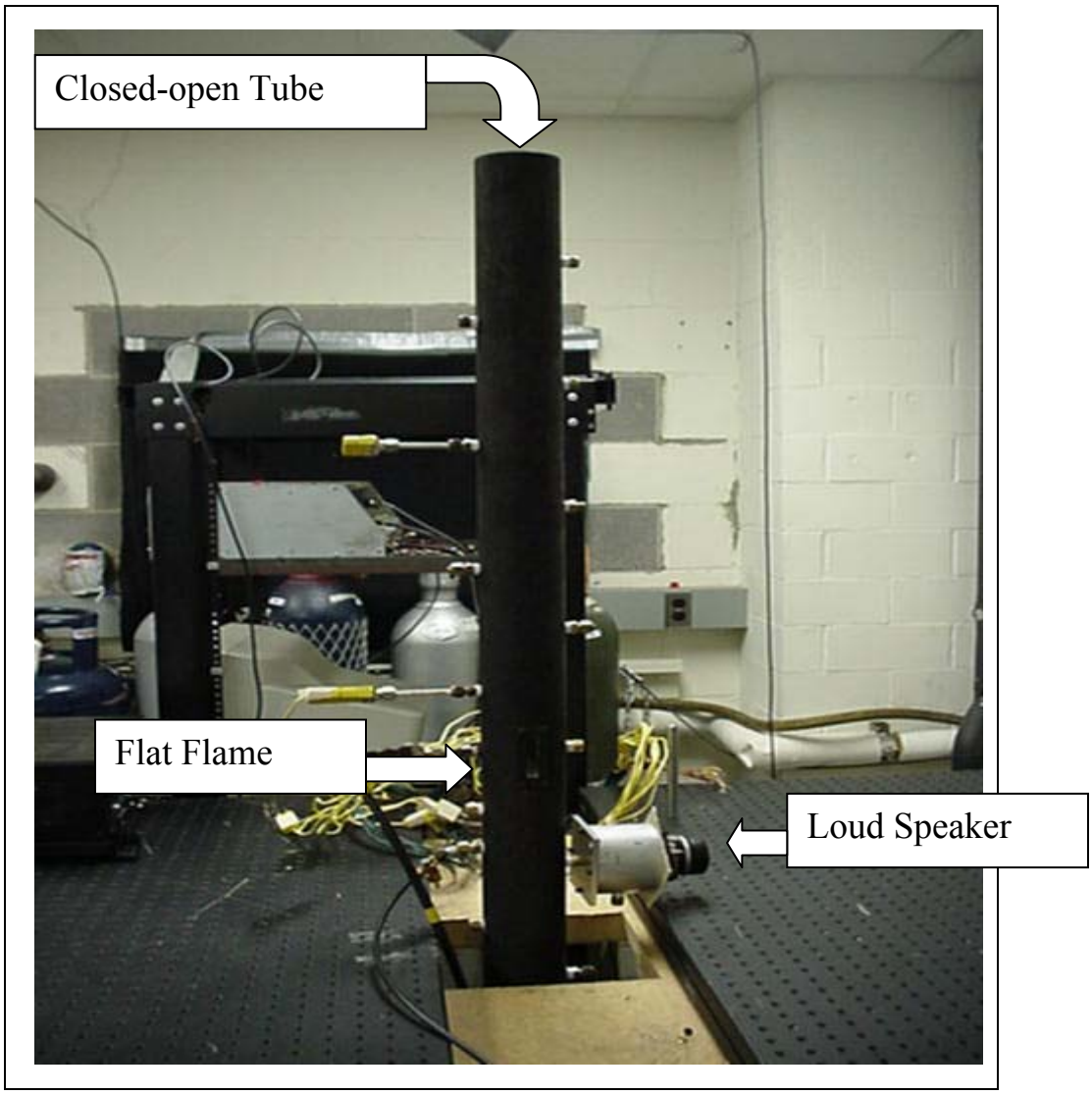

Figure 1.2 Rijke tube experimental set-up

Boundary conditions can be established for pressure and velocity. At the solid interface, pressure is a maximum and velocity is zero. At the open interface, pressure is atmospheric and the velocity is at a maximum. The waveforms shown in Figure 1.3 were established using Euler's equation,

$$\rho \frac{\partial v}{\partial t} = -\nabla P$$

By taking the Fourier transform of Equation 1, the derivative in time can be expressed as jω and the ∇ operator can be expressed as $\frac{dP}{dx}$ for this one-dimensional problem. The resulting equation relating pressure and velocity is,

$$v = \frac{j}{\rho\omega}\frac{dP}{dx}$$

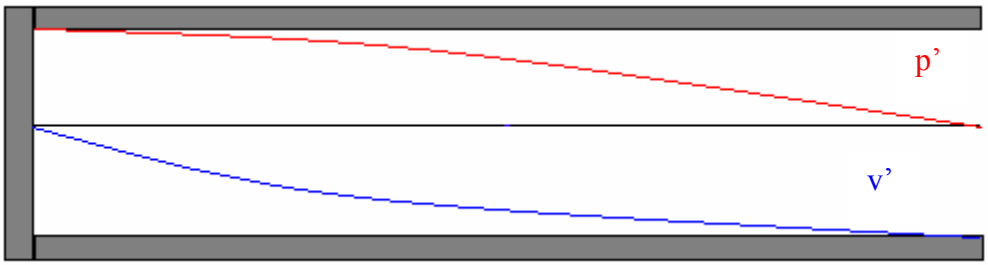

P = P_{max}
v' = 0

P = P_{atm}
v' = v'_{max}

Figure 1.3 Schematic of closed-open tube with quarter-wave

The standing pressure wave can be determined from the boundary conditions above, and the velocity field can then be found from the boundary conditions and Euler's equation. Figure 1.3 shows a quarter-wave, which is the lowest frequency waveform that fits the boundary conditions. It is important to note at this point that Euler's equation relates pressure and velocity, yet Rayleigh's criterion relates pressure and heat release. Therefore, a relationship between the unsteady velocity and the heat release rate must be known. Assuming a first-order relationship where the dynamics of the flame's response is slow compared to the acoustic dynamics, it can be assumed that velocity is proportional to heat release and lags at approximately 90°. Thus, velocity may be applied to Rayleigh's criterion with the j from the above expression of Euler's equation canceling the lag in phase.

It can be seen in Figure 1.3 that the quarter-wave resonance has no spatial location where pressure and velocity are in phase, thus the Rayleigh index will always have a negative value. This is supported by the fact that in the closed-open tube, there is no instability at the quarter-wave frequency.

The three-quarter wave is the next waveform that fits the boundary conditions. This can be seen in Figure 1.4. It is clear velocity and pressure are indeed in phase throughout sections of the tube. The maximum value of the Rayleigh index occurs at L/2, one half the length of the tube. This is the point at which instability is most probable, thus the flame is positioned at this point in the tube.

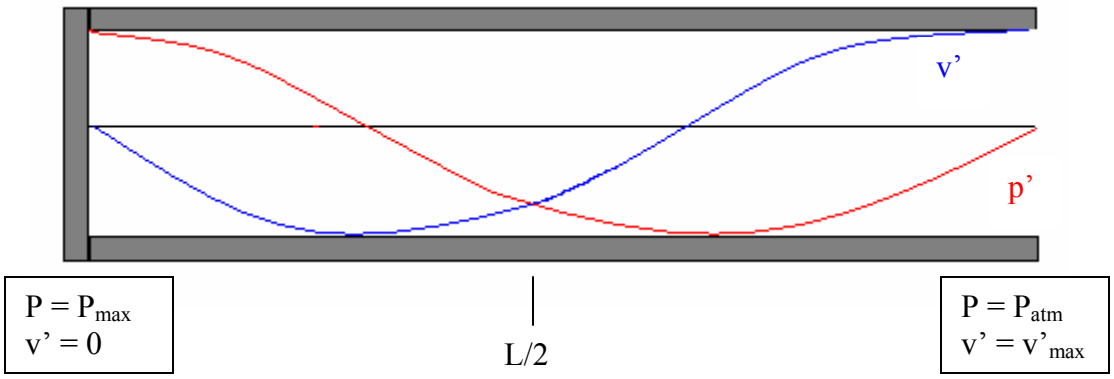

Figure 1.4 Schematic of closed-open tube with three-quarter wave

The power spectral density of the Rijke tube is shown in Figure 1.5. It is clear that the dominant source of energy for this system occurs at approximately 180 Hz, which is the second acoustic mode of the tube as described above. There is also a noticeable peak at approximately 360 Hz. This corresponds to a seven-quarter standing wave, which also has a maximum Rayleigh index at half the length of the tube. The first and third acoustic modes show slight peaks in the power spectrum at 90 and 270 Hz, respectively. An instability is not produced at this frequency, however, which is consistent with Rayleigh's criterion for the tube.

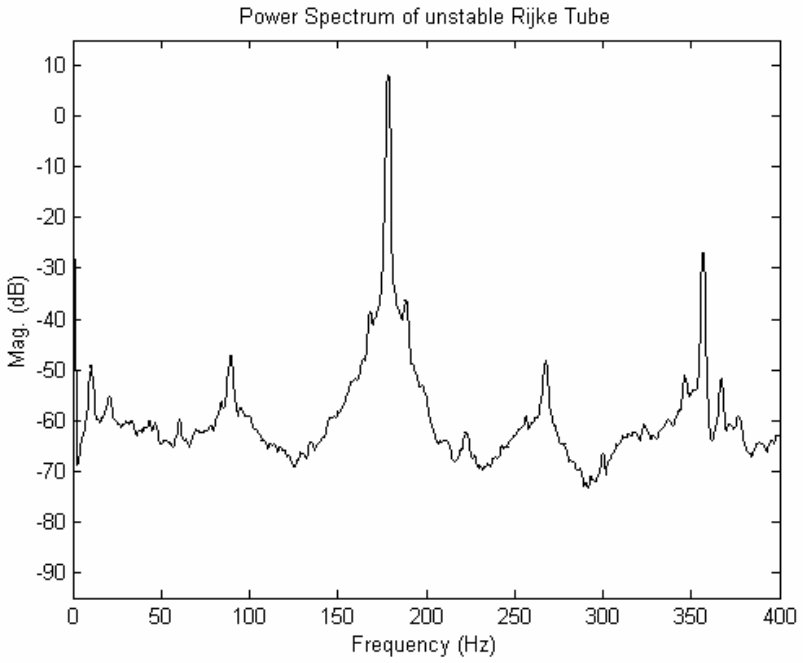

Figure 1.5 Power spectrum of the unstable Rijke tube

1.3 Adaptive Filtering

Due to changes in the system with time and operating conditions, fixed compensators have been met with only a limited amount of success for controlling thermoacoustic instabilities. Adaptive control, however, can be very effective for this application. The distinguishing properties of an adaptive system are non-linearity and time variance of the compensator parameters.

The classical feed-forward adaptive control is shown in Figure 1.6. In this set-up, the reference signal and the output signal are used by the adaptive algorithm to adjust the parameters of the compensator.

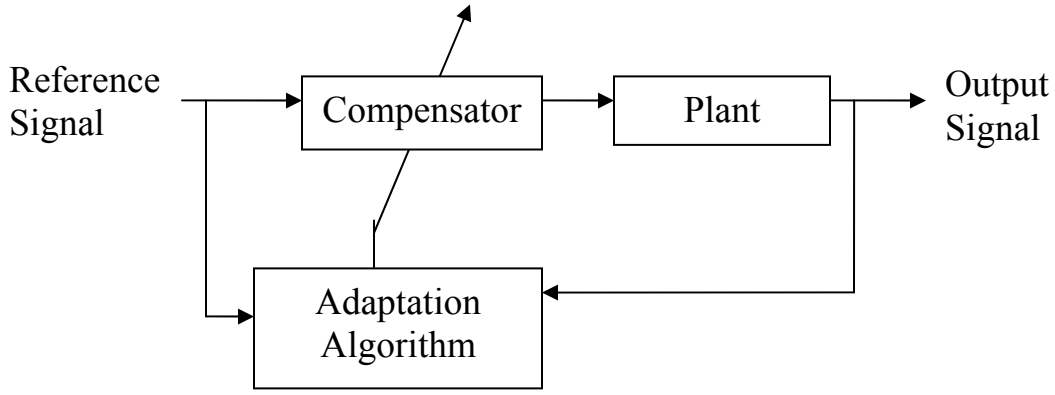

Figure 1.6 Feed-forward adaptive block diagram

This work has dealt with a more complicated system that requires feedback adaptive control, due to the fact that feed-forward control is not suitable for stabilizing an unstable system.

Figure 1.7 shows the block diagram of the control structure that was used in this work.

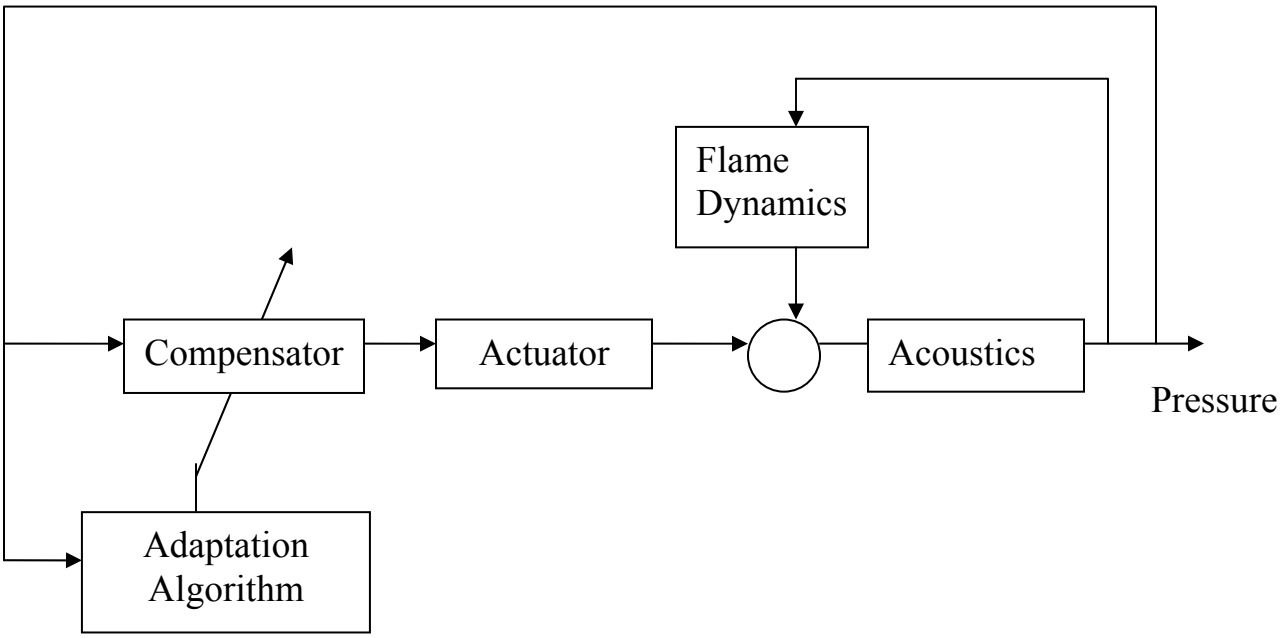

Figure 1.7 Feedback adaptive control block diagram

1.4 Research Goals

The fundamental goal of this work is to develop a tool for active combustion control (ACC) of thermoacoustic instabilities. This package is to be self-contained, with minimal input needed from the user. The scope of this tool is from the determination of a limit cycling instability to the ultimate suppression of that instability. This tool includes a digital bandpass filter, a tuning phase which automatically selects parameter values, several minimization algorithms with variable number of weights, proportional or pulsed control, and sub-harmonic control capabilities. The theory behind the various adaptive filtering algorithms that are incorporated in this work is provided in Chapter 3. These algorithms were used to adapt an FIR filter and also used for sub-harmonic pulsed control.

Tests of the algorithms were done on an analog electronic simulator, a premixed methane-air Rijke tube combustor, and a kerosene fuel tube combustor. The goal was to successfully control each unstable limit-cycling plant in a minimum amount of time. If complete control was not possible, maximum attenuation of the limit cycle amplitude was desired. Comparisons of different algorithms were conducted and documented in following chapters.

This work was developed for the specific application of active combustion control, but could be incorporated into other areas of active noise reduction or control of any self-excited system.

1.5 Document Overview

Following this introduction, Chapter 2 is a review of pertinent literature related to the topic of active combustion control and combustion instabilities.

A detailed explanation of each minimization algorithm is set forth in Chapter 3. This chapter also covers the implementation of these algorithms into a robust package, along with other front-end issues incorporated into this work.

Chapter 4 describes an analog electronic simulator that was used during the implementation and testing phases of the various algorithms. Results of these tests are also discussed in this chapter.

Chapter 5 outlines the work done on the Rijke tube combustor with a description of the experimental set-up. Results for the algorithms at varying equivalence ratios (Φ) using proportional actuation are discussed. Pulsed control and sub-harmonic control are also discussed for a single operating condition. Work on a liquid fuel combustor is also detailed in this chapter.

Chapter 6 draws some conclusions of this work, along with outlining some the future work that is to follow. The Appendix contains data on each test discussed above, providing transient responses, adaptive weights, the magnitude and phase of the controller, and power spectral density plots for controlled states.

Chapter 2 Literature Review

There has been a great deal of work done in the past concerning suppression of thermoacoustic instabilities using both passive and active techniques. Passive techniques include absorption linings, modifications in the fuel delivery system, or the design of the combustor geometry. These passive techniques are not discussed here; instead this chapter is an overview of previous work in the area of active combustion control (ACC), including work using adaptive techniques and those using modeling strategies.

2.1 Closed loop control – Phase Shifter

Several studies have shown success in controlling the instabilities in a Rijke tube combustor via closed-loop active control. The sensor signal, which could be the pressure signal from the combustor or light emission form CH radicals, was filtered and phase-shifted to drive an acoustic actuator and the end of the tube. The pressure oscillation associated with the speaker created an unsteady boundary condition at tube-end and, with the proper amount of phase-shift, caused a decrease in the acoustic energy of the instability wave [6].

2.2 Model-based control

Much of the work involved with thermoacoustic instabilities has involved the development of model-based control strategies. Annaswamy, et al. [9] have developed a model which includes flame dynamics, acoustics, and a loudspeaker as an actuator. The flame dynamics of this model were produced from the conservation equations of mass, momentum, and energy. The acoustics were modeled considering longitudinal modes and linear dynamics.

The model was verified using a bench-top combustor with a power output of approximately 1 kW and an instability frequency of 470 Hz. Two separate control schemes were used on this combustor: LQG-LTR control and H_∞ control.
The LQG-LTR control is a combined estimator-state feedback design, and has the form:

$$\dot{\hat{x}} = A\hat{x} + Bu + H(y - C\hat{x})$$

$$u = -K\hat{x}$$

where H and K are the estimator gain and state feedback gain, respectively, and are to be designed. The matrices A, B, and C are from the state-space model of the combustor. The dynamics of the loudspeaker were determined using a signal generator and a photo sensor, which measured the displacement of the speaker. From this a frequency analysis was conducted and a transfer function for the speaker was developed.

The use of this control scheme on the bench-top combustor resulted in a 45 dB attenuation of the limit-cycle frequency. Perturbations of the LQG parameters showed

that the design was also robust with respect to 20% errors in the model. This highlights a disadvantage of this controller, which is that the robustness cannot be computed a priori. An H_∞ controller was also incorporated in this work. This type of controller uses frequency domain specifications for performance evaluation. An advantage of this controller is that the robustness can be bounded a priori, however it cannot explicitly include time domain specifications such as actuator saturation limits.

This controller also proved to be effective in the attenuation of the instability in the bench top test rig. Overall, however, the LQG controller outperformed this controller.

The results of this paper showed that a linear design could be used to control this process although the limit-cycling behavior is nonlinear. Also, these controllers eliminated the problem of secondary peaks, secondary instabilities that would arise after the initial limit-cycle was suppressed, which had plagued earlier work.

Another group that has used model-based control is Jacobson, Krstic, and Krupadanam [8]. Though the basis of this work is a model for this process, it also bridges the gap between model-based techniques and the next topic, adaptive control. The work begins with the nonlinear model of acoustic waves in a combustion environment that was developed by Culick in 1976. Fung and Yang took this model and proposed a PI (Proportional, Integral) controller. The gains for this controller, however, required that knowledge of the model parameters. It is possible that changes in the parameters of Culick's model, be it by variations in the combustor over time or by errors in modeling, may result in the stabilization of the 1st mode but a destabilization of the 2nd.

The focus of this work was to use Lyapunov-based adaptation, which takes both modes into account, to adapt the gains of the PI controller. Simulations were carried out using a secondary fuel line to modulate fuel flow, and were shown to effectively attenuate that limit-cycle of the instability.

Another important result of this work was that this technique was shown to stabilize the system in the presence of time delays, which are inherent to the sensing and actuation processes. Also, this scheme can be carried out with only a single pressure sensor used to measure the combustor pressure signal.

2.3 Adaptive Control

Though there has been success in the use of models for control of thermoacoustic instabilities, there has also been a great deal of work with techniques in which little a priori information is needed. Adaptive control has been shown to be effective in this area, and has the advantage of being able to withstand changes in the operating condition of the combustor.

An adaptive algorithm that has been proven to be effective is the Least Mean Square (LMS) algorithm that was developed by Widrow in 1970. The LMS algorithm is based on the method of steepest descent with using an instantaneous approximation of the gradient. This algorithm is very attractive because it is computationally efficient and very easy to implement. A group that has done work with this algorithm is Bowman and Kemal from Stanford University [10]. A transversal filter was selected as the filter structure because of its ease of implementation. The update law for the filter coefficients in the LMS algorithm is:

$$W_{k+1} = W_k + 2\mu\varepsilon_k X_k$$

where $X_k = [x_k \; x_{k-1} .. x_{k-L}]^T$, $W_k = [w_{0k} \; w_{1k} \; ... \; w_{Lk}]^T$ and ε_k is the error signal and μ is the convergence parameter which affects stability and convergence rate.

In order to use ε_k directly it was required to be prefiltered by a model of the plant. Thus the LMS algorithm that was implemented was:

$$W_{k+1} = W_k + 2\mu\varepsilon_k U_k$$

where U is obtained by convolving X and C (the plant model). The filter architecture is modified to include another adaptive process that directly obtains this model of the plant. This model is then used as the prefilter to the LMS algorithm. This is known as the filtered-x LMS algorithm.

Tests of this algorithm were conducted on a laboratory scale premixed dump combustor with an acoustic actuator and a piezoelectric pressure transducer just downstream of the inlet. The result was a 15% reduction in the normalized pressure oscillations. An IIR architecture was also studied and was found to handle direct acoustic feedback better than the FIR design, but was susceptible to becoming unstable.

Vaudrey [1] did a great deal of work with different algorithms for suppression of thermoacoustic instabilities. Some of the main areas of the work were artificial neural networks (ANN), the LMS algorithm, and the time-averaged gradient (TAG) algorithm. An ANN was developed using a variety of flow rates and equivalence ratios on a Rijke tube combustor. Thermocouples were used to measure temperatures throughout the tube, and the output was an open-loop frequency response function (FRF). This FRF was used to modify the gain and phase a fixed shape controller.

The result of experiments on a Rijke tube with the ANN was a 50 dB attenuation of the instability. Another result was effective system identification in the frequency domain. This method of control can be very effective on a single combustor, but a major drawback is that a lengthy system identification process is required to build the database for the ANN, which may be unacceptable for real world applications.

Vaudrey also studied the effectiveness of the TAG algorithm, which is a steepest descent algorithm and has also been used throughout this work. This algorithm has many very attractive features; namely, it requires very little a priori information, it can adapt to changes in plants, and can be used with any controller parameterization or actuation scheme. Vaudrey used the TAG algorithm with FIR, IIR, and subharmonic control

architectures. With a two-weight FIR implementation an attenuation of nearly 60 dB was achieved on the pre-mixed methane-air Rijke tube.

Jacobson, et al. [11] have used what they referred to as a classical extremum-seeking algorithm, which estimates the derivative of the pressure magnitude with respect to control phase by introducing a sinusoidal variation in the control phase and measuring the response of the pressure magnitude, and a triangular search algorithm, which uses the three past sampled average magnitude values to determine the new control phase. The fundamental idea behind the triangular algorithm is to determine an interval that contains the extremum of a function and reduce the size of this interval at an exponential rate. A frequency-tracking algorithm, which was based on an Extended Kalman Filter, was also implemented within the control structure.

Jacobsen's work was focused on performance specifications during engine acceleration transients, and experiments were carried out on a 4 MW single nozzle rig with a full-scale engine nozzle at realistic operating conditions. Simulations were also conducted by representing the process as a lightly damped second order system for the acoustic mode and a large delay with a saturation nonlinearity representing the heat release process. The results of this study were that both the triangular algorithm and extremum-seeking algorithm performed well in the engine transients at high power conditions and reasonably well at lower power conditions. Also both algorithms ability to track the changing optimal control phase shift during engine acceleration has been demonstrated in simulation.

This present work is comprised entirely of adaptive control, which is very attractive because the same controller can be applied to a variety of combustors. Any information that is required of the system is obtained during a brief parameter-tuning phase. Several different adaptive algorithms are explored here, using both acoustic actuation and modulated fuel on a liquid fuel combustor.

Chapter 3 Minimization Algorithms

This work has concerned itself with several minimization algorithms, which can be divided into two basic categories: gradient descent methods and pattern searches. In general, the gradient descent methods perturb the filter weights, calculate the gradient of the cost function, and descend in the gradient direction. The pattern searches perturb along specified directions, compute the corresponding mean squared error, and make decisions about future directions based on the these computations.

The control structure for this work was to adaptively update the coefficients of a finite impulse response (FIR) filter, though these algorithms are versatile and are not constrained to this type of controller. Note that these are direct optimization algorithms, which do not require a priori plant models. The following sections describe in detail the algorithms that were incorporated in this work. In later chapters, the algorithms will be referred to by the shorthand name in parentheses.

3.1 Gradient Descent Algorithms

3.1.1 Time-Averaged Gradient (TAG)

The TAG algorithm performs a gradient search by the method of steepest descent for which the basic weight update equation is:

$$w_n(k+1) = w_n(k) - \mu\xi'(w_n(k))$$

where w_n is the nth filter coefficient and the gradient, ξ', is calculated from:

$$\xi'(w_n) = \frac{\xi(w_n) - \xi(w_n - \delta)}{\delta}.$$

The cost function, ξ, is the mean squared error (MSE) of the signal:

$$\xi(w_n) = \frac{1}{N}\sum_{k=0}^{N} e^2(k).$$

The convergence parameter, μ, is a system dependent value that controls the speed of adaptation and stability of the filter.

A more detailed description of this algorithm can be found in Widrow [3] and experimental results were presented by Vaudrey[1].

3.1.2 Gradient Descent with Line Search (Gradient)

This algorithm is an extension of the TAG algorithm, with the addition of a line search along the gradient direction. The gradient is calculated using the same procedure

described above, but instead of taking a fixed step along the gradient, the algorithm searches along the gradient direction for the optimal step size. This is done by taking successively larger step sizes and evaluating the corresponding MSE. When an increase in step size no longer results in increased performance, a new gradient is calculated, and the procedure is repeated.

3.1.3 Fletcher and Reeves Conjugate Gradient (Conjugate)

The conjugate gradient method of Fletcher and Reeves creates search directions that are a linear combination of the steepest decent direction and previous search directions. Weighting factors are applied such that the search directions are conjugate. These factors are ratios of the present and past squared norms of the gradient. Bazaraa and Shetty[2] summarized the Fletcher and Reeves Conjugate Gradient as follows:

Initialization Step: The scalar $\varepsilon > 0$ terminates the algorithm and the initial point is x_1. Let $y_1 = x_1$, $d_1 = -\nabla f(y_1)$, k = j = 1, and go to the main step

Main Step:

1. If $\|\nabla f(y_j)\| < \varepsilon$, stop. Otherwise, let λ_j be the optimal solution to the problem to minimize $f(y_j + \lambda_j d_j)$ subject to $\lambda_j \geq 0$, and let $y_{j+1} = y_j + \lambda_j d_j$. If $j < n$, go to step 2, otherwise go to step 3.
2. Let $d_{j+1} = -\nabla f(y_{j+1}) + \alpha_j d_j$, where $\alpha_j = \dfrac{\|\nabla f(y_{j+1})\|^2}{\|\nabla f(y_j)\|^2}$. Replace j by j + 1, and go to step 1.
3. Let $y_1 = x_{k+1} = y_{n+1}$, and let $d_1 = -\nabla f(y_1)$. Let j =1, replace k by k + 1, and go to step 1.

The concept of conjugacy is very important in unconstrained optimization problems. If the function to be minimized is quadratic, conjugate search directions guarantee that convergence will occur in at most n steps, where n is the number of parameters being adapted.

3.2 Pattern Search Algorithms

3.2.1 **Hooke and Jeeves Pattern Search with Line Search (Hooke and Jeeves)**

The first pattern search algorithm discussed here is that of Hooke and Jeeves. The original algorithm proposed by Hooke and Jeeves was a strict pattern search along the weight directions. The version incorporated in this work is an adapted version that uses both a pattern search and a line search along the successful directions. Bazaraa and Shetty[2] summarized the Hooke and Jeeves Pattern Search as follows:

Initialization Step: $\mathbf{d}_1,\ldots,\mathbf{d}_n$ are the coordinate directions. The scalar $\varepsilon > 0$ is used to terminate the algorithm. Also choose an initial step size, $\Delta > \varepsilon$, and an acceleration factor, $\alpha > 0$. Choose a starting point $\mathbf{x_1}$, let $\mathbf{y_1} = \mathbf{x_1}$, let k = j =1, and go to main step.

Main Step:

1. If $f(y_j + \Delta d_j) < f(y_j)$, the trial is deemed a success; let $y_{j+1} = y_j + \Delta d_j$, and go to step 2. If $f(y_j + \Delta d_j) \geq f(y_j)$, the trial is deemed a failure. In this case, if $f(y_j - \Delta d_j) < f(y_j)$, let $y_{j+1} = y_j - \Delta d_j$, and go to step 2; if $f(y_j - \Delta d_j) \geq f(y_j)$, let $y_{j+1} = y_j$, and go to step 2.
2. If $j < n$, replace j by j + 1, and repeat step 1. Otherwise go to step 3 if $f(y_{n+1}) < f(x_k)$, and go to step 4 if $f(y_{n+1}) \geq f(x_k)$.
3. Let $x_{k+1} = y_{n+1}$, and let $y_1 = x_{k+1} + \alpha(x_{k+1} - x_k)$. Replace k with k + 1, let j = 1, and go to step 1.
4. If $\Delta < \varepsilon$, stop; x_k is the solution. Otherwise replace Δ by $\Delta/2$. Let $y_1 = x_k$, $x_{k+1} = x_k$, replace k by k + 1, let j =1, and repeat step 1.

This algorithm can be thought of in two separate phases: an exploratory search (represented by steps 1 and 2 above) and a pattern search (step 3). The exploratory search successively perturbs along each weight direction and tests the resulting performance. The pattern search steps along the $(x_{k+1} - x_k)$ direction, or the direction between the last two points selected by the exploratory search. When perturbations along both the positive and negative weight direction do not result in enhanced performance, the perturbation size is decreased. When the perturbation size is less than a predetermined termination factor, ε, the algorithm stops and assumes an optimal solution.

3.2.2 **Method of Rosenbrock (Rosenbrock)**

The method of Rosenbrock uses a pattern search technique to evaluate functional values along the search directions. An acceleration term is included to increase or decrease the step size as the algorithm progresses. Bazaraa and Shetty [2] summarized the Rosenbrock Pattern Search as follows:

Initialization Step: $\mathbf{d}_1,\ldots,\mathbf{d}_n$ are the coordinate directions and $\overline{\Delta}_1,\ldots,\overline{\Delta}_n > 0$ be the initial step sizes along these directions. The scalar $\varepsilon > 0$ is used to terminate the algorithm. Let $\alpha > 1$ be the expansion factor and $\beta \in (-1,0)$ be the contraction factor. Choose a starting point $\mathbf{x_1}$, let $\mathbf{y_1} = \mathbf{x_1}$, let k = j =1, let $\Delta_j = \overline{\Delta}_j$ for each j, and go to main step.

Main Step:

1. If $f(y_j + \Delta_j d_j) < f(y_j)$, the trial is deemed a success; let $y_{j+1} = y_j + \Delta_j d_j$ and $\Delta_j = \alpha\Delta_j$. If $f(y_j + \Delta_j d_j) \geq f(y_j)$, the trial is deemed a failure; let $y_{j+1} = y_j$ and $\Delta_j = \beta\Delta_j$. If j < n, replace j by j + 1, and repeat step 1. Otherwise, if j = n, go to step 2.

2. If $f(y_{n+1}) < f(y_1)$, that is if any of the n trials of step 1 were successful, let $y_1 = y_{n+1}$, set j = 1, and repeat step 1. Consider the case when $f(y_{n+1}) = f(y_1)$, that is when each of the n trials in step 1 was a failure. If $f(y_{n+1}) < f(x_k)$, that is if at least one trial was successful during iteration k, go to step 3. If $f(y_{n+1}) = f(x_k)$, stop with x_k as an estimate for the optimal solution if $|\Delta_j| \leq \varepsilon$ for each j; otherwise, let $y_1 = y_{n+1}$, j = 1, and go to step 1.

3. Let $x_{k+1} = y_{n+1}$. If $\|x_{k+1} - x_k\| < \varepsilon$, stop with x_{k+1} as an optimal solution. Otherwise, compute $\lambda_1,\ldots,\lambda_n$ from the relationship $x_{k+1} - x_k = \sum_{j=1}^{n} \lambda_j d_j$, form a new set of directions for the Gram-Schmidt procedure, let $\Delta_j = \overline{\Delta}_j$ for each j, let $y_1 = x_{k+1}$, replace k with k +1, let j =1, and repeat step 1.

The Gram-Schmidt procedure used in the Rosenbrock algorithm for calculating new directions can be expressed as:

$$a_j = \begin{cases} d_j & if\ \lambda_j = 0 \\ \sum_{i=j}^{n} \lambda_i d_i & if\ \lambda_j \neq 0 \end{cases}$$

$$b_j = \begin{cases} a_j & if\ j = 1 \\ a_j - \sum_{i=1}^{j-1} \left(a_j{}^t \bar{d}_i \right) \bar{d}_i & if\ j \geq 2 \end{cases}$$

$$\bar{d}_j = \frac{b_j}{\|b_j\|}$$

This algorithm begins with searches along the weight directions. If a perturbation results in a lower MSE, the expansion term, α, is used to increase the step size in that direction. If a higher MSE results, the contraction term, β, reverses the sign of the perturbation and decreases the magnitude. This is repeated until a failure occurs along all directions, which leads to the development of new directions through the Gram-Schmidt procedure.

The Gram-Schmidt procedure takes the mutually orthogonal, linearly independent weight directions, $d_1, \ldots, d_n$, and forms new directions $\bar{d}_1, \ldots, \bar{d}_n$. The result is a new set of linearly independent orthogonal search directions. The Gram-Schmidt procedure forms a special case of conjugate directions, and thus the Rosenbrock algorithm behaves similarly to a conjugate direction method in its convergence upon a quadratic function.

3.3 Robustness and Implementation Issues

For the above algorithms, the function that was to be minimized was the mean squared error, defined as

$$MSE = \frac{1}{N} \sum_{k=1}^{N} e^2(k),$$

where *e* is the error signal of interest and *N* is the number of samples over which the error is averaged.

In some of the algorithms the MSE was made to be mean-zero data by subtracting the mean value from each element prior to squaring the signal. This was done because it was determined that a slight shift in the DC value could mask changes in the amplitude of the signal. This process was implemented in algorithms in which a decision on the performance was made, including Hooke and Jeeves, Rosenbrock, and Gradient.

Some algorithms were terminated if the MSE was below a threshold value. This was also incorporated into the decision-making algorithms to prevent them from making decisions based on signals not related to the initial limit cycle, such as noise from the

pressure transducer. A forgetting factor was applied to the MSE calculation for systems with a slow response time. The forgetting factor weights the array of inputs, giving recent values the most control over the MSE, allowing initial transients to die out.

These algorithms were used for several different control strategies. The first form of control was proportional actuation, which means that the control signal is proportional to the reference signal. This was used on the simulator and the acoustic actuator controlling the Rijke Tube. Pulsed, or on-off, actuation and subharmonic control were also used on the Rijke tube. Subharmonic control uses a control signal at harmonic frequencies below the fundamental frequency of the instability. Refer to Carson [5] for more results and discussion on the use of subharmonic signals for control of thermoacoustic instabilities.

3.4 Parameter Determination – Tuning Phase

The algorithms described above are functions of several parameters. These parameters are system-dependent, thus should be chosen automatically to insure the robustness of the minimization process. Two parameters that are involved in each algorithm are the integration length, N, and the perturbation size, δ. As mentioned earlier, the integration length is the number of samples over which the MSE is averaged. The perturbation size serves as change in a weight direction for gradient calculation or MSE evaluation.

The value of the MSE approaches the true value as the integration length approaches infinity. Because the algorithms are run in real-time and there is a desire to minimize convergence time, the goal is to find a minimum integration length while maintaining an accurate estimate of the MSE. This procedure involved reading the error signal and computing the MSE at each sample. The past *n* MSE values were then evaluated, where *n* is a specified evaluation range. When the maximum and minimum MSE values within this range fell within a certain percentage of each other, the current number of samples was considered an adequate integration length. If this condition was not met, the integration length was increased and the next MSE value was computed. The result of this is a transient response similar to a second order system. An example of this procedure is shown in Figure 3.1, which is a plot of the MSE calculation versus the sample number for an electronic simulation. At approximately 300 samples, the calculation of the MSE has reached a near steady-state value.

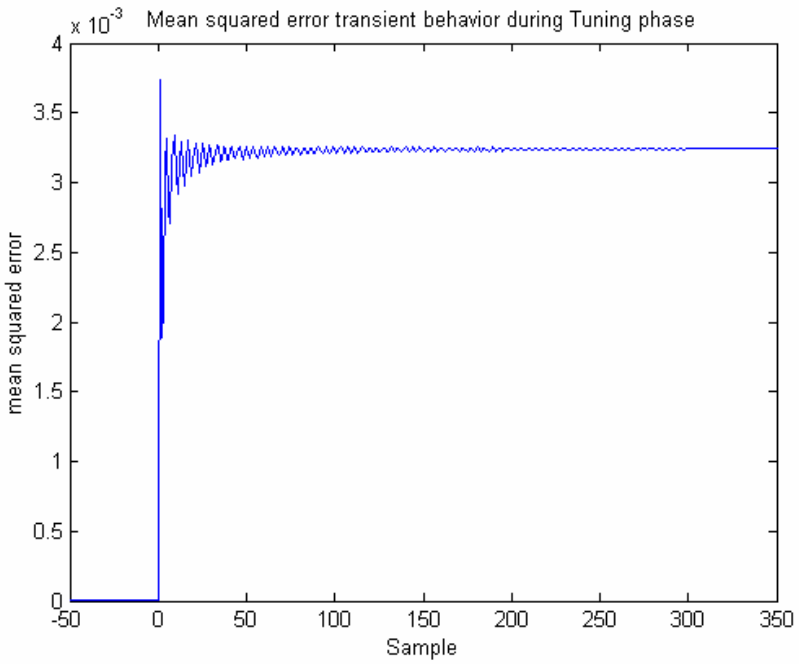

Figure 3.1 Mean squared error transient behavior during tuning phase

It was necessary for the perturbation size to be large enough to cause a measurable change in the signal, yet not so large as to drive the system unstable once control was achieved. The initial perturbation size was chosen to be relatively small. The first weight was perturbed and the change in the MSE was measured. If the percent change was below a minimum value, the perturbation size was increased. If the change exceeded a maximum value, it was decreased. Thus, when the change fell into a certain range, it was deemed acceptable. In practice, the acceptable range was a 20 – 25% change in the MSE.

The convergence parameter, μ, was also calculated during the tuning phase. Widrow [3] gives the bounds of μ for the LMS algorithm as

$$\frac{1}{\lambda_{\max}} > \mu > 0$$

where λ_{max} is the largest eigenvalue of the input correlation matrix, R. The R matrix is defined as

$$R = E\left[X_k X_k^{\,T}\right]$$

where X_k is the input matrix.

It can then be stated that λ_{max} cannot be greater than the trace of R (tr[R]), which is the sum of the diagonal elements of R. From the definition of R,

$$tr[R] = (L)E[x_k^{\,2}]$$

where L is the number of inputs. Thus the bounds of μ can be stated as

$$0 < \mu < \frac{1}{(L)(signal\ power)}$$

In practice, the signal power was calculated identically to the MSE mentioned above, and the convergence parameter used was 15% of the upper bound given above. Because this expression is derived from work on the LMS algorithm and assumes a transversal filter, this approach is valid when used to adapt an FIR filter. This approach was used for this work because these algorithms were indeed used to adapt an FIR filter, but care must be taken if a different control structure is being employed. These bounds may no longer be valid.

Chapter 4 Electronic Simulations

An analog electronic simulator was used during the coding and algorithm validation. There are several reasons for the implementation of this simulator. The first is that it is very desirable to work with a well-defined plant. There has been a great deal of research on the Rijke tube, but the nonlinearities inherent in an actual combustor provide additional complexities not involved in the simulator. By using the simulator, the algorithms could be isolated, and errors in the convergence of the simulated signal could be attributed to the algorithms being tested. The simulator also provided for a less cumbersome test environment. The set-up and takedown process for the simulator was far less intensive than that of an actual combustor. Finally, because the simulator is an electronic device, its use conserved fuel that would be used on a combustor.

4.1 Electronic Simulator

The electronic simulator was designed from simulations performed by Vaudrey[1]. A block diagram representation of this system is shown in Figure 4.1. The tube acoustics were modeled as a single degree of freedom lightly damped second order system, while the flame dynamics were incorporated as a low pass filter. A saturation non-linearity was used to introduce a limit cycling phenomenon, similar to the behavior in a Rijke tube combustor.

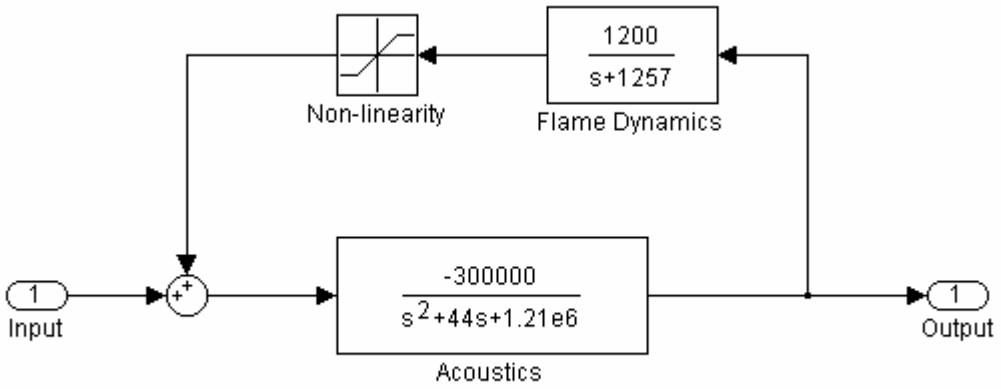

Figure 4.1 Block diagram representation of electronic simulator

The analog electronic implementation of this block diagram is shown in Figure 4.2.

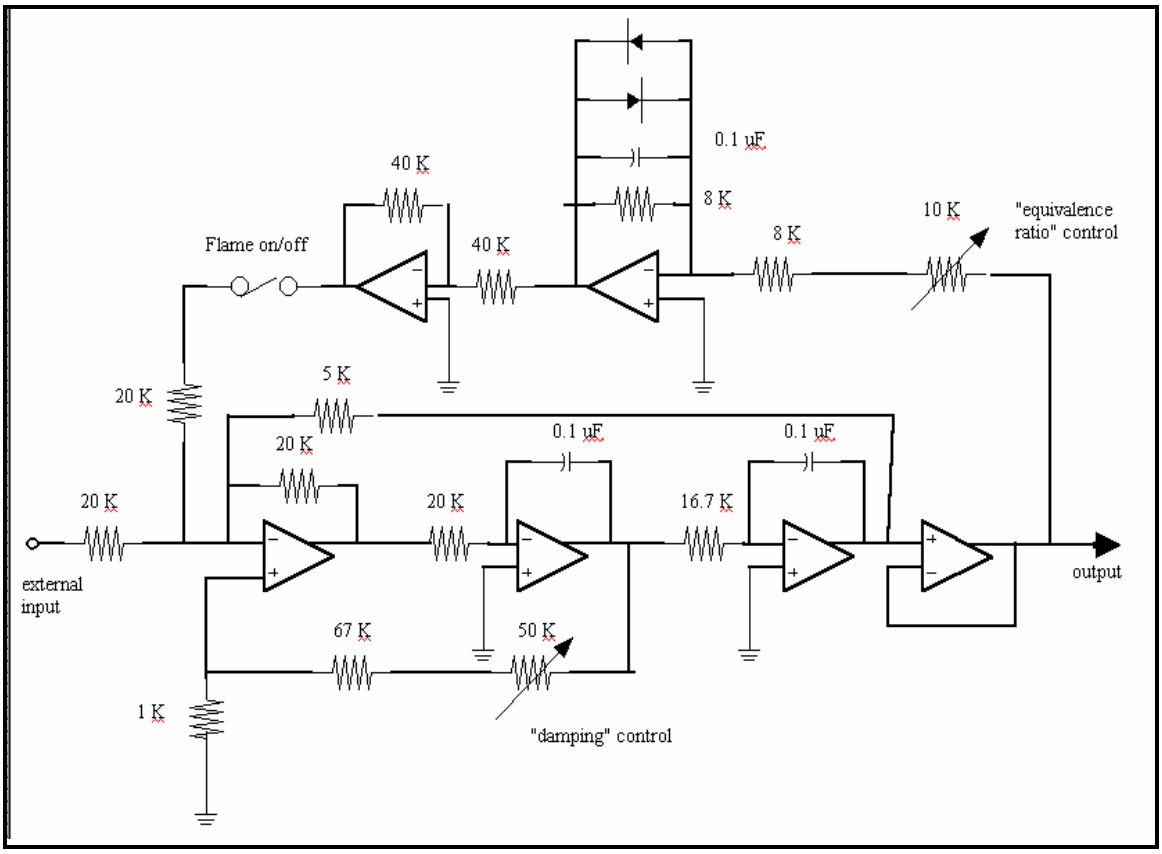

Figure 4.2 Analog electronic representation of simulator

A photograph of the simulator that was used for this work is shown in Figure 4.3, and time trace of the exponential growth envelope and the limit cycling behavior of the simulator is shown in Figure 4.4, and a schematic of the algorithm validation set-up is shown in Figure 4.8.

Figure 4.3 Electronic simulator

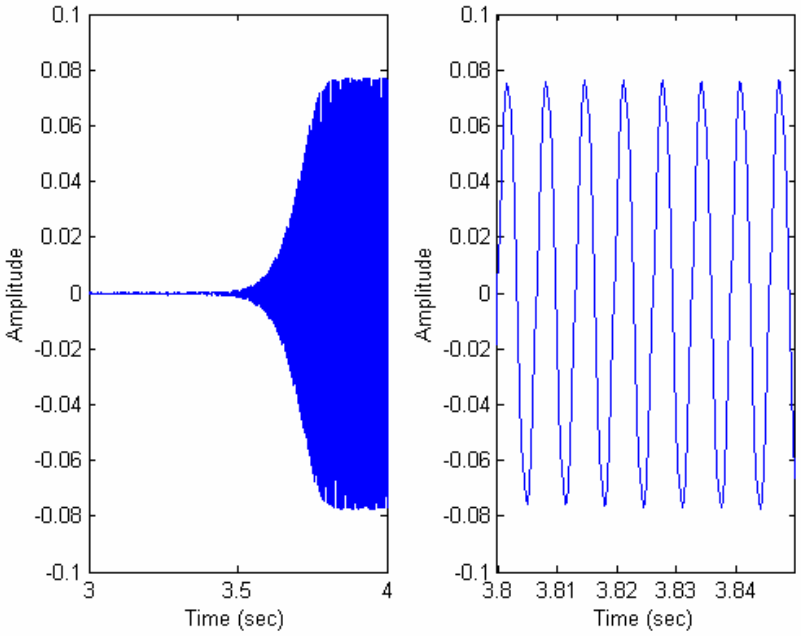

Figure 4.4 The growth envelope and limit cycling behavior of the simulator

The simulator oscillated at approximately 165 Hz with limit cycle amplitude of –2 dBVrms. The power spectrum of the simulator output signal can be seen in Figure 4.5. The performance surface for the simulator can be seen in Figure 4.6 as a three-dimensional plot of MSE versus the filter weights. The filter weights are the coefficients of an FIR filter used to control the output signal. Another performance surface is shown in Figure 4.7, this is a three-dimensional plot of the MSE of the simulator versus the phase and magnitude of the phase shift controller.

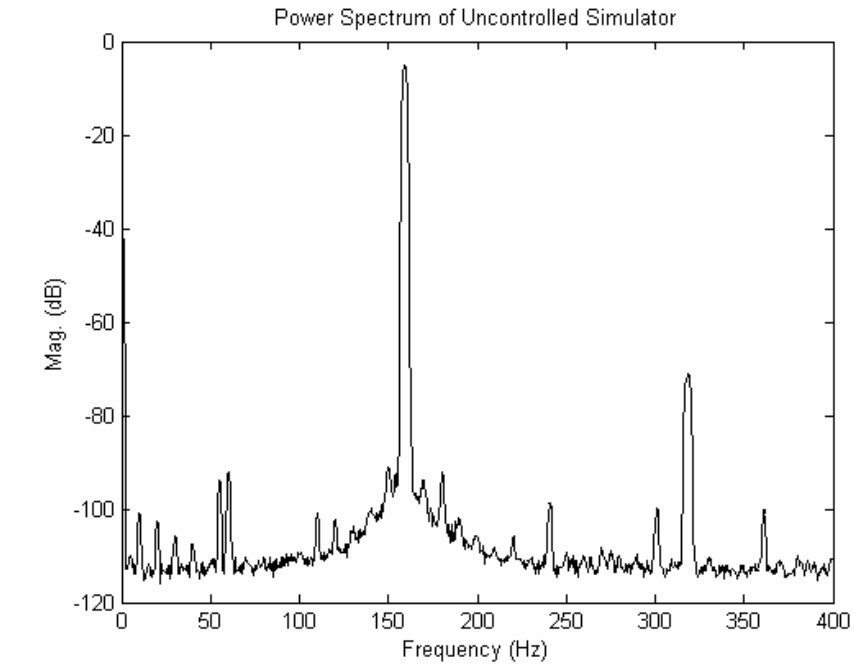

Figure 4.5 Power spectrum of electronic simulator

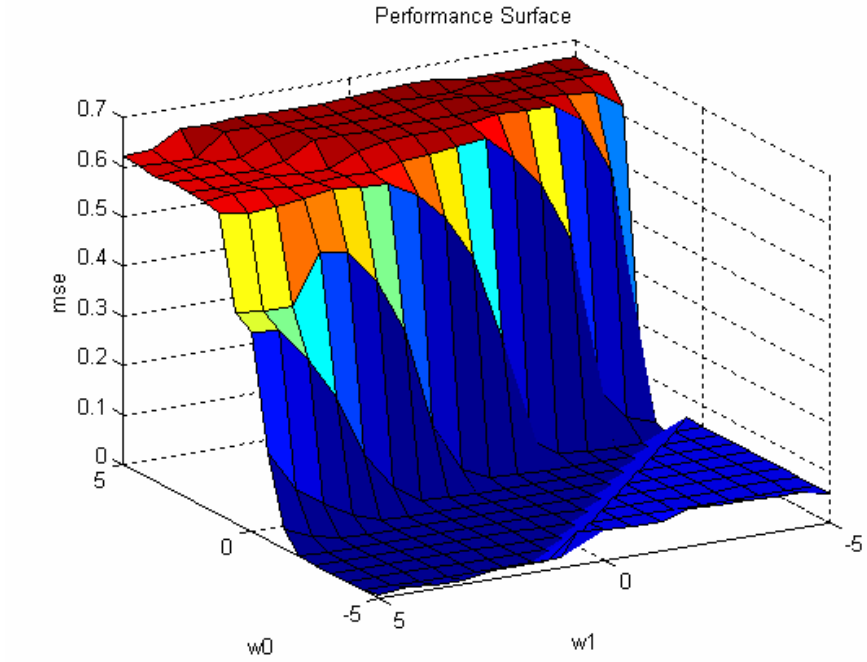

Figure 4.6 Performance surface for electronic simulator using filter weights

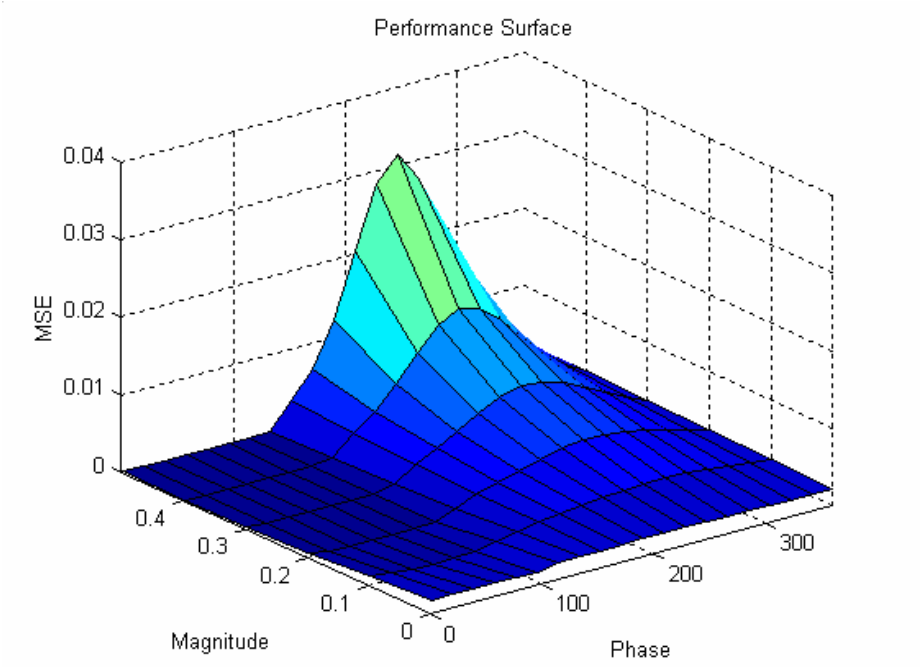

Figure 4.7 Performance surface for electronic simulator using phase and magnitude

4.2 Algorithm Validation Procedure

This section explains the process of implementing the simulator and validating the adaptive algorithms. The simulator was powered by a 15 V input. The simulator produced a simulated pressure signal that was fed into the dSpace DSP board. The adaptive algorithms used this signal to adapt a two-weight FIR filter and output to the DAC. This control signal was fed back to the simulator serving as the "acoustic actuation." The block diagram of this loop is shown in Figure 4.8.

Each algorithm was implemented using C language. The aforementioned set-up was used to test the control performance of the algorithm. The baseline for the validation process was a simple phase shift controller. This phase shifter had a variable sample delay and magnitude multiplier. Manual adjustment of the number of sample delay and gain could easily achieve attenuation of 60 dBVrms and maintain control indefinitely. Results with the adaptive algorithms that were considerably worse than this might indicate an error in the implementation of the algorithm. The processes of implementation, diagnostics, and modification of the algorithms continued until each algorithm could repeatedly stabilize the simulator.

A key phase in the diagnostics process of each algorithm was the acquisition of data. An HP Digital Signal Analyzer was used to collect the power spectral density (PSD) of the output of the simulator. This was necessary for the determination of the attenuation and frequency components of the signal. Another tool was the time trace capture using the dSpace ControlDesk software. With this data, the decay envelope and trajectory of the FIR filter weights (and thus, the magnitude and phase of the filter) could

be analyzed. The convergence time, smoothness of convergence, and maintained stability were some of the parameters that were analyzed when validating various algorithms.

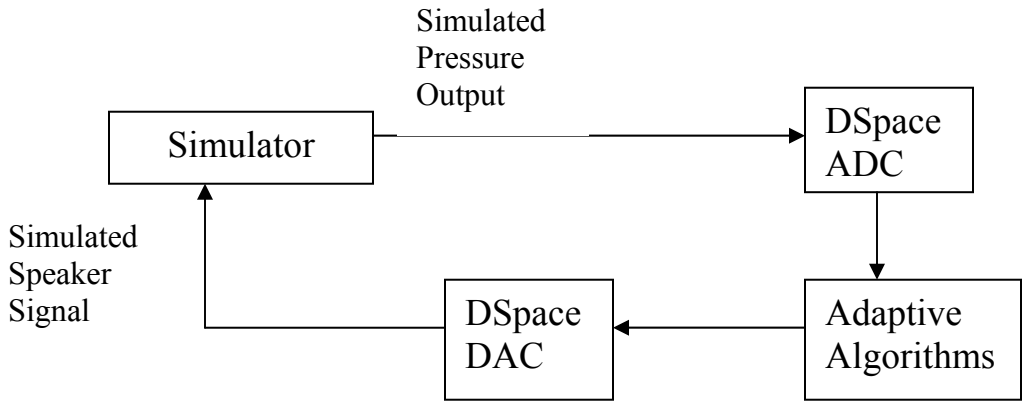

Figure 4.8 Schematic for algorithm validation using electronic simulator

The algorithms that were described in the previous chapter were used to adapt a two-weight FIR filter used to stabilize the oscillations of the simulator. The sampling frequency was 1600 Hz. The decay envelope, the phase and magnitude of the compensator, and the power spectral density for the control simulator for each algorithm is found below. It is important to note here that although the adaptive algorithms were concerned with the weights of the FIR filter, the following plots show the magnitude and phase of the filter. This was done because the parameters of magnitude and phase are more intuitive to most readers than the actual weight values. It is a straightforward process to convert the weight values to magnitude and phase.

The filter, G, can be expressed in the z-domain as:

$$G(z) = w_0 z^{-1} + w_1 z^{-2}$$

$$z = e^{j\omega T}$$

where filters of longer length would continue in decreasing powers of z. Using the identity that $e^{-j\omega T} = \cos(\omega T) - j\sin(\omega T)$ yields:

$$G(\omega) = w_0[\cos(\omega T) - j\sin(\omega T)] + w_1[\cos(2\omega T) - j\sin(2\omega T)]$$

And thus the phase and magnitude of G can be expressed as:

$$\angle G = \tan^{-1}\left(\frac{-[w_0 \sin(\omega T) + w_1 \sin(2\omega T)]}{[w_0 \cos(\omega T) + w_1 \cos(2\omega T)]}\right)$$

$$|G| = \sqrt{[w_0 \cos(\omega T) + w_1 \cos(2\omega T)]^2 + [w_0 \sin(\omega T) + w_1 \sin(2\omega T)]^2}$$

Additional results for the simulator are shown in Appendix A, which contains the frequency response of each filter at the steady-state weight values and the trajectories of the filter weights.

The tuning phase described in the previous chapter was used to determine acceptable values for the integration length, perturbation size, and convergence parameter. Table 4-1 documents the results of this process.

Table 4-1 Parameter values for the simulator

Convergence Parameter, μ	38.48
Perturbation Size, δ	0.192
Integration Length, N	299 samples

Figure 4.9 through Figure 4.18 below show the results of controlling the simulator.

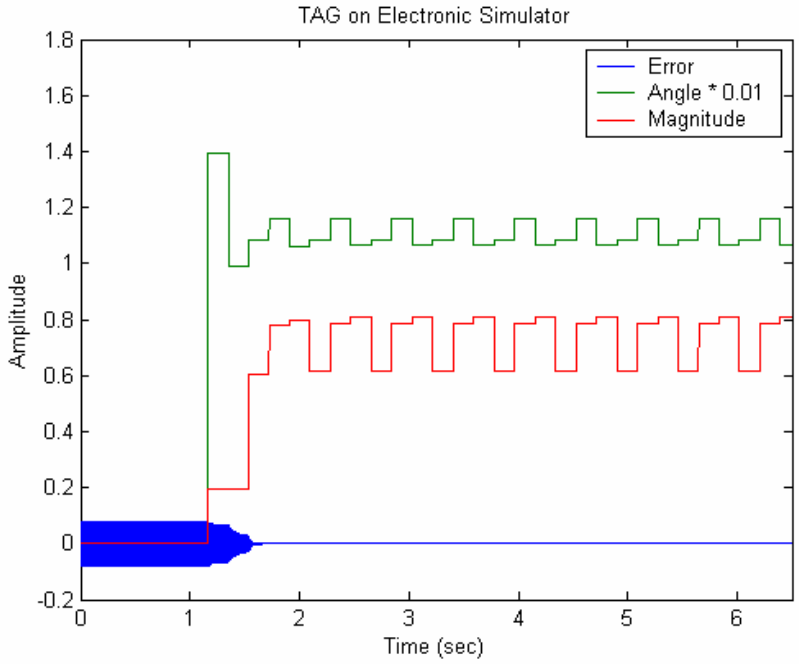

Figure 4.9 Phase and magnitude of filter for TAG algorithm

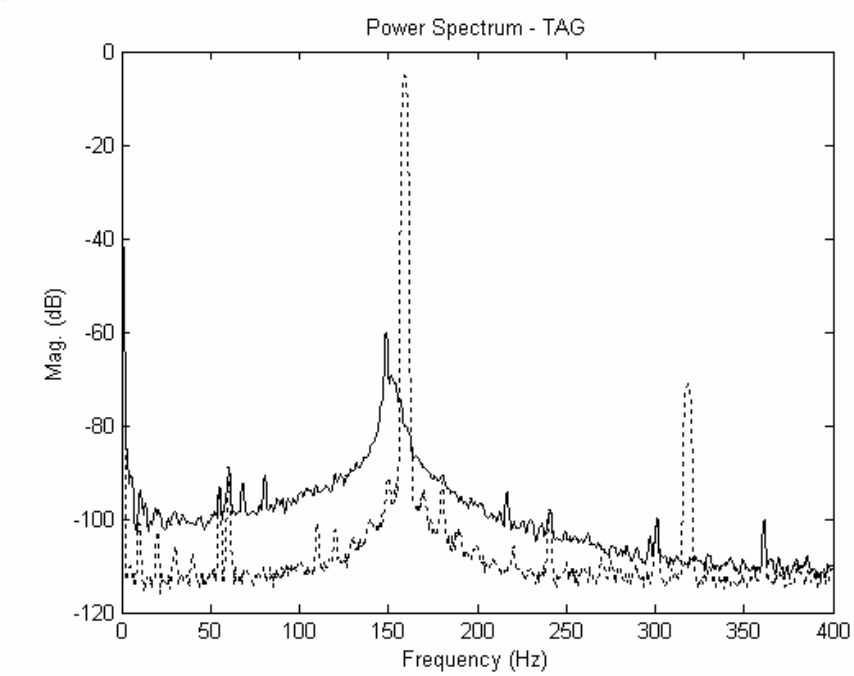

Figure 4.10 Power spectrum of TAG-controlled simulator

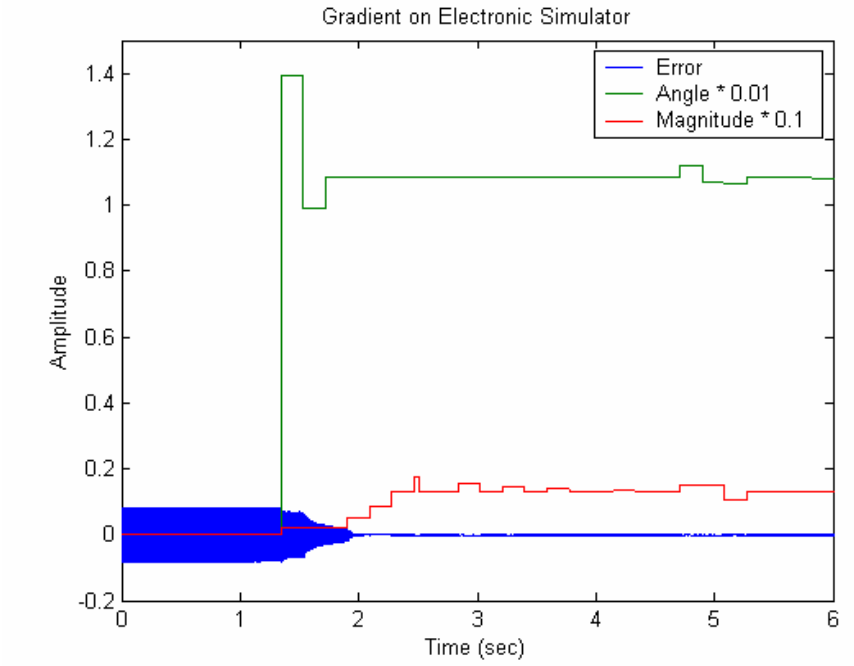

Figure 4.11 Phase and magnitude of filter for Gradient algorithm

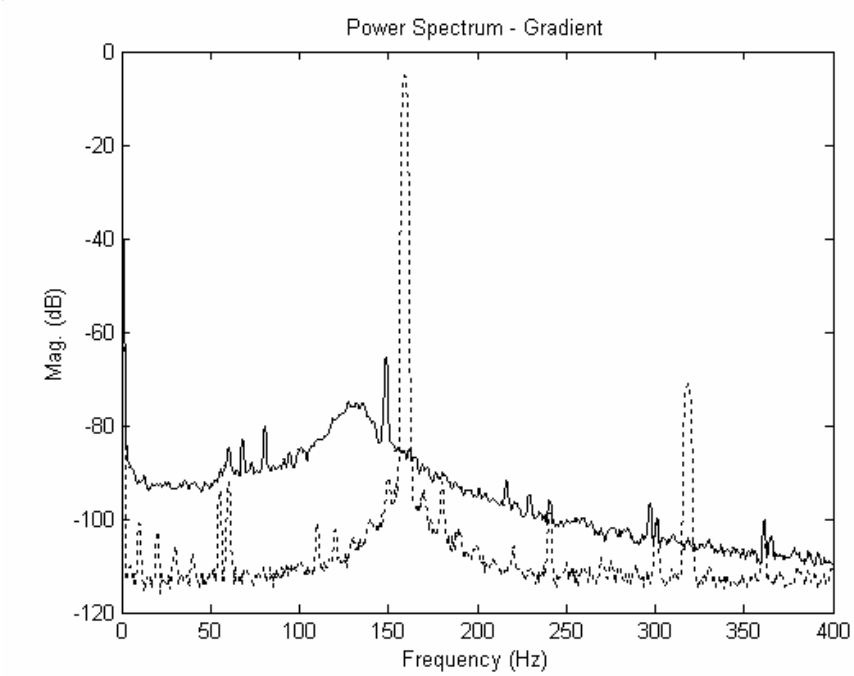

Figure 4.12 Power spectrum of Gradient-controlled simulator

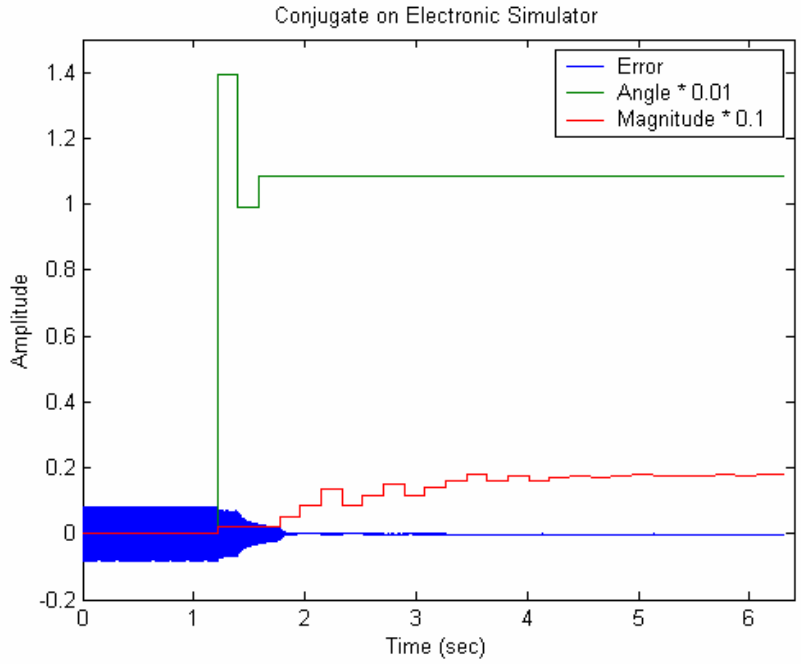

Figure 4.13 Phase and magnitude of filter for Conjugate algorithm

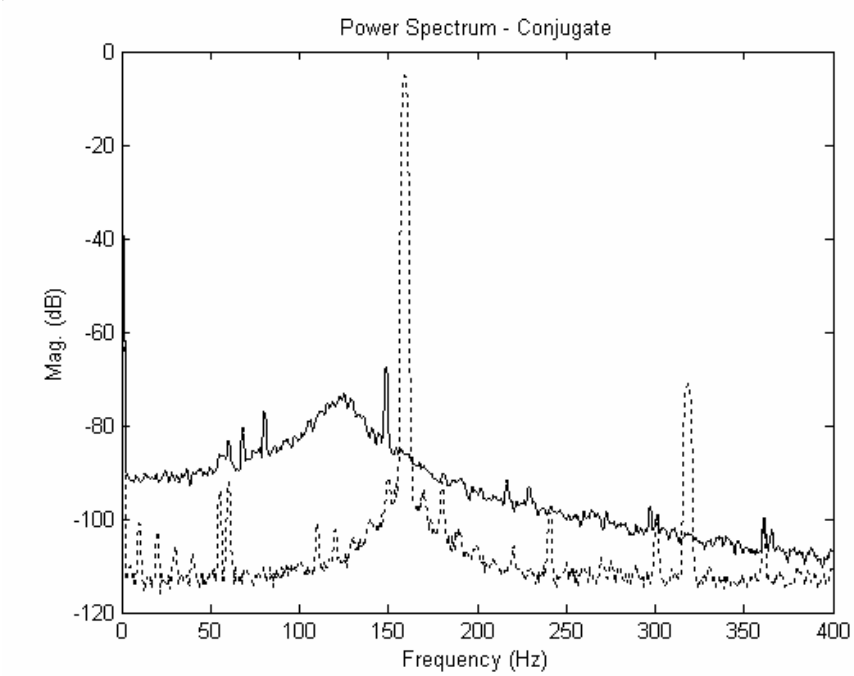

Figure 4.14 Power spectrum of Conjugate-controlled simulator

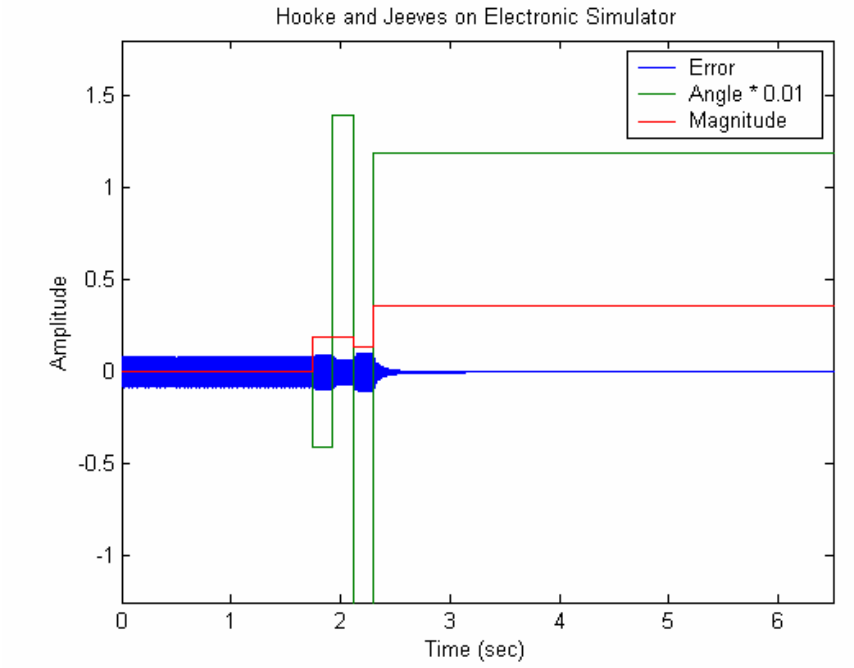

Figure 4.15 Phase and magnitude of filter for Hooke and Jeeves algorithm

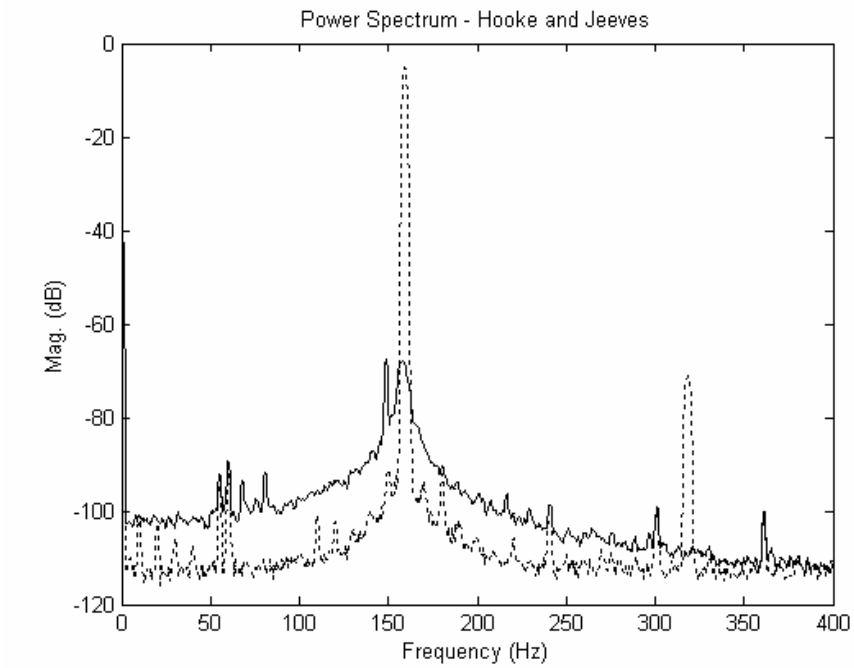

Figure 4.16 Power spectrum of Hooke and Jeeves-controlled simulator

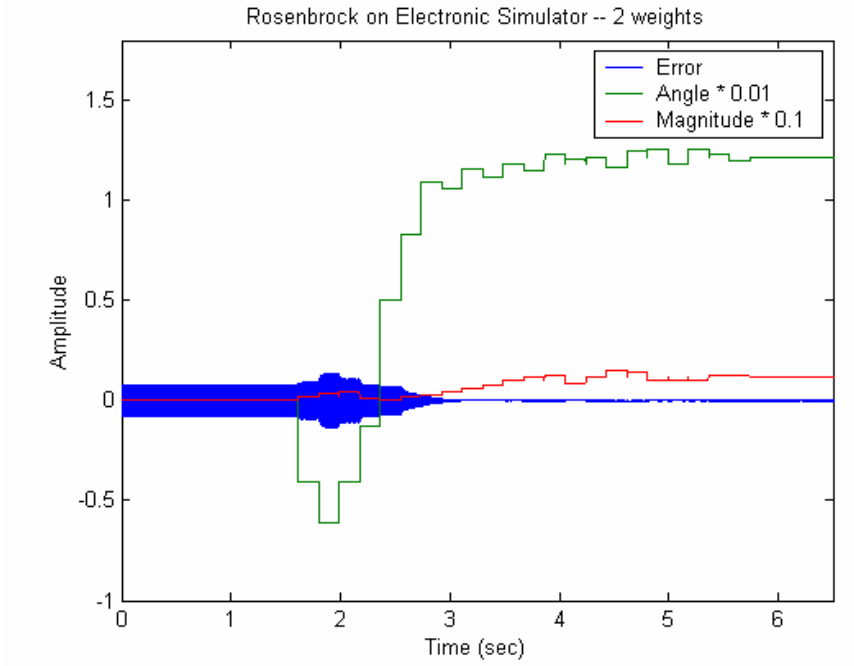

Figure 4.17 Phase and magnitude of filter for Rosenbrock algorithm

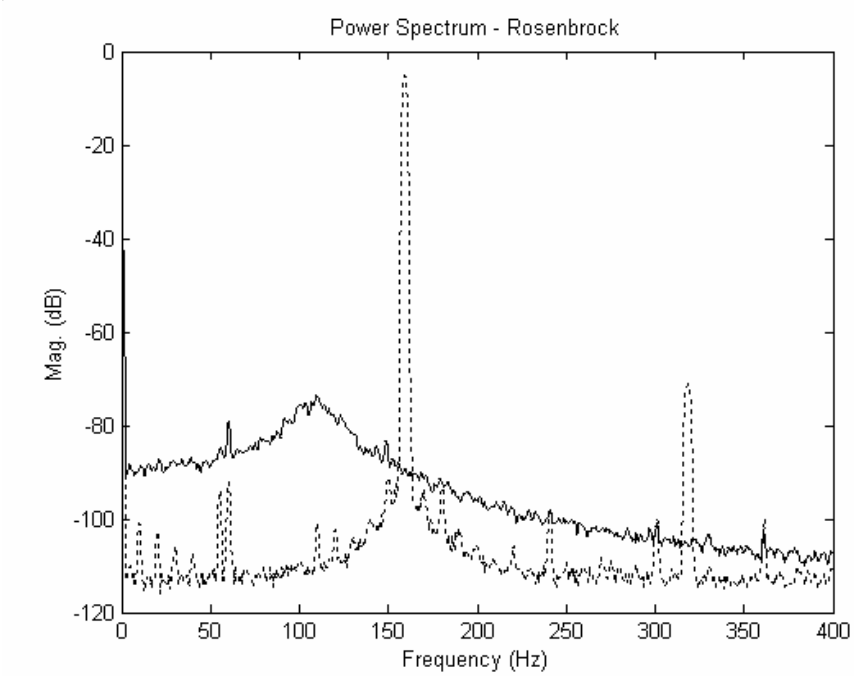

Figure 4.18 Power spectrum of Rosenbrock-controlled simulator

Table 4-2 gives results for convergence time and ultimate attenuation for the tests performed on the simulator. The ultimate attenuation is the averaged decibel attenuation of the signal from the uncontrolled state to the controlled state.

Table 4-2 Convergence times and ultimate attenuation at limit cycle frequency for the simulator

Algorithm	Convergence Time	Ultimate Attenuation	Magnitude	Phase
TAG	0.51 sec.	54.9 dB	0.72	112°
Gradient	0.73 sec.	60.2 dB	1.32	108°
Conjugate	0.75 sec.	62.1 dB	1.79	109°
Hooke and Jeeves	1.65 sec.	62.5 dB	0.36	119°
Rosenbrock	1.51 sec.	67.7 dB	1.17	122°

Note that although the algorithms formed compensators with similar phases, ranging from 108° to 122°, there was a fairly large variance in the magnitude. This suggests that there is a large region of the weight space that controls the system, which is reiterated by the cost surface in Figure 4.6. It also points out a limitation in the algorithms, in that they do not optimize the solution with respect to control output. The Hooke and Jeeves algorithm was terminated if a minimum MSE was achieved, thus not allowing the algorithm to make decisions on noise in the system. The other algorithms were not equipped with this feature, and therefore continued to increase the gain of the controller even after sufficient suppression has been achieved.

4.3 Discussion

Throughout the coding process there were several problems that arose simply due to errors in converting the algorithm into C code. It is not necessary to go into detail these issues at this time. Other problems, however, were of a more conceptual nature. As mentioned in Chapter 3, the error was made mean-zero for certain algorithms. Specifically this was done on the algorithms that compared the current performance to past performances, such as Gradient, Hooke and Jeeves, and Rosenbrock. It was first noticed that the controller using the Gradient algorithm was successful in stabilizing the simulator with acceptable convergence times and signal attenuation, however the signal would begin to diverge after a period of time. Close inspection of the stabilized output of the simulator showed that there was a slight DC offset in the signal. Thus, there were two independent components to the MSE of the signal: the DC offset and the limit cycle amplitude. It was found that a slight increase in the limit cycle amplitude could actually result in a lower MSE. This led the algorithm in the non-optimal direction, and eventually to a condition that lost control of the simulator. By making the data mean-zero, the only component of the signal of interest was the amplitude of the limit cycle.

Another issue that was encountered during the validation process concerned the Hooke and Jeeves algorithm. This issue showed the same symptoms as described above, in that the algorithm was able to control the simulator for a period of time but would then lose control. This problem, however, was a result of the algorithm making decisions based on a noise signal. When the initial limit cycle was stabilized, the algorithm continued to search the weight space for increased performance. There may be slight variations in the MSE of the noise that the algorithm believes are a result of weight perturbations. This again leads to perturbations in the non-optimal direction and to loss of control. The solution to this problem was to implement a threshold value for the output of the simulator. When the algorithm sees an MSE less than this threshold, the adaptation stops at the current position. The MSE continues to be computed and the algorithm will begin to adapt again if the MSE value grows large.

Eventually, each algorithm was successful in controlling the simulator, which is not surprising when the cost function in Figure 4.6 is considered. The simulator had a cost function that rolled off quite dramatically with a large region that achieved control.

It can be seen in Table 4-2 that the gradient descent algorithms outperformed the pattern search algorithms with respect to convergence time. By calculating a gradient, the gradient descent algorithms gain insight on the dynamics of the system, and thus move towards an optimal solution. The pattern searches, however, are systematically searching the weight space, which may result in search steps in the non-optimal direction. The Rosenbrock and Hooke and Jeeves results above show this behavior. The signal magnitude actually increases in the initial steps of these algorithms, signifying a step in the non-optimal direction. Because of this, one would expect the gradient descent algorithms to converge in less time than the pattern searches. Also, although each algorithm was able to achieve a great deal of attenuation; the pattern searches seem to have slightly outperformed the gradient descents in this respect.

It is important to note here that although the phase of the filters produced by the algorithms were within a very small range; this may not necessarily be the case. It can be shown that destructive interference will occur between two signals if they are within 60° of the optimal phase, where the optimal phase results in complete destruction of the signal. This suggests that the algorithms do not necessarily need to find the optimal phase relationship to gain control, but that there is, in fact, a range of phase values that will provide suppression of the pressure signal. Figure 4.19 demonstrates this concept graphically. Plot (1) shows the destructive interference resulting from the additional of a signal with the optimal phase shift. Plot (2) shows the interference with a phase shift 30° from the optimal, which still results in attenuation of the signal. Plot (3) shows that at 60° from the optimal, where the signal magnitude is unchanged, but only shifted in phase. Plot (4) shows that at more than 60° from the optimal, there is constructive interference, which is undesirable within the confines of this work.

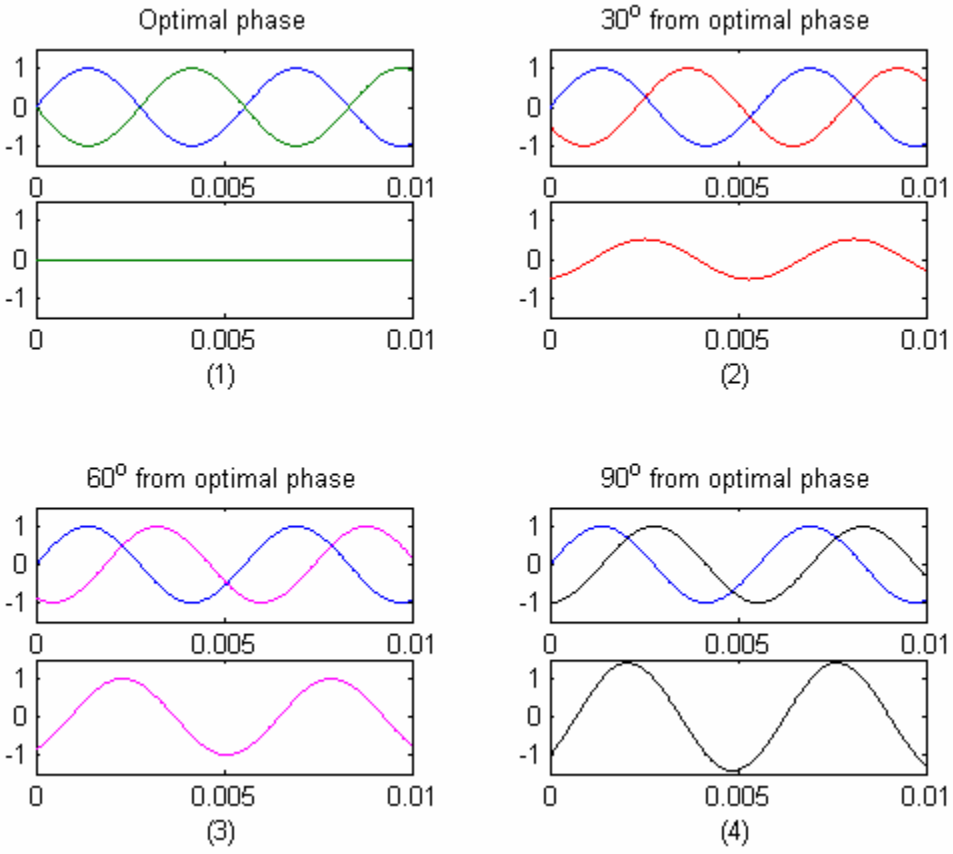

Figure 4.19 Signal interference for various phases

It is also interesting to note that, although there was considerable attenuation at the instability frequency, the overall noise floor was raised after control. The reason for this can be seen when the Bode plots for the controlled and uncontrolled simulator are compared. These are seen in Figure 4.20 and Figure 4.21.

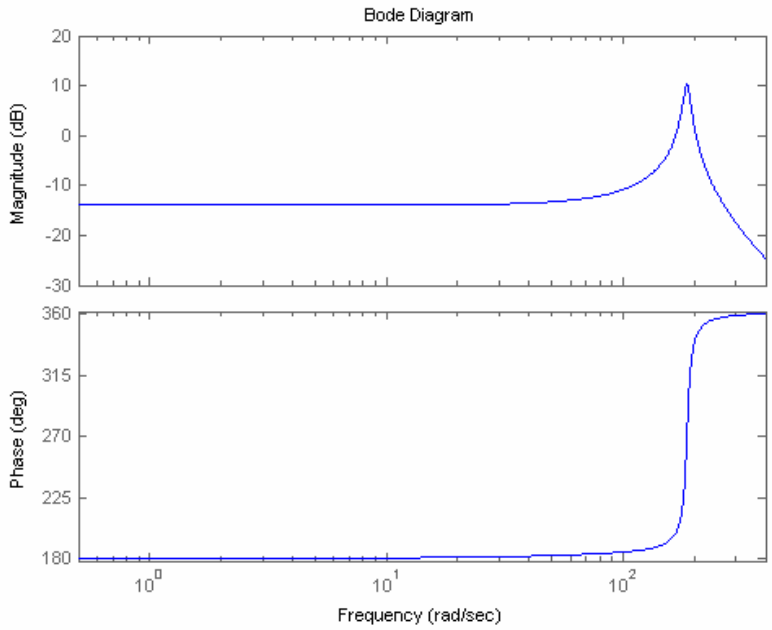

Figure 4.20 Bode plot for the uncontrolled simulator

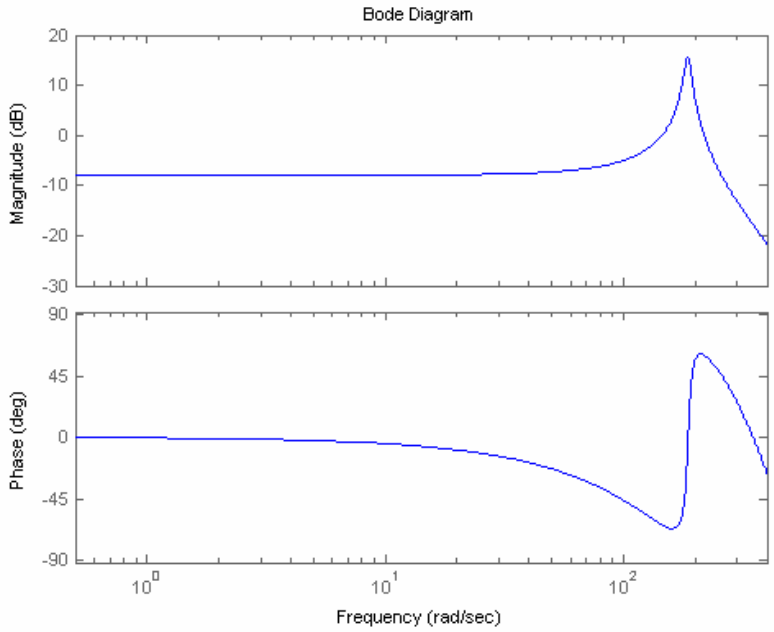

Figure 4.21 Bode plot for the controlled simulator

Comparing the two plots, it is clear that the low frequency magnitude has increased due to the influence of the controller. Assuming that the broadband noise component is unchanged by control, the noise floor should then increase.

Chapter 5 Combustor Experiments

As mentioned earlier, the first combustor that was included in this work was a simple open-closed tube combustor, often referred to as a Rijke tube. Because the simulator was modeled after the physics observed in the Rijke tube, the adaptive algorithms that effectively controlled the simulator should also be able to gain control over the Rijke tube. A major difference between the simulator and the actual combustor is the fact that the simulator is a completely stationary system. The combustor, however, fluctuates due to variations in heat transfer and temperature of the tube. Also the nonlinear dynamics between the simulator and the combustor are quite different. The limit cycle amplitude increase as the equivalence ratio increases, which eventually leads to an inability to control due to actuator authority issues. This issue will be discussed in detail later in the chapter.

A second combustor, which was fuel be kerosene and actuated by modulating the flow of fuel, was also investigated. Results for this combustor are not as extensive as for the Rijke tube.

5.1 Rijke Tube Experimental Set-up

A ceramic honeycomb was used to stabilize a premixed air-methane flame located at one-half the length of the tube. The interaction between the heat release rate and the pressure fluctuations in the tube form a self-excited loop. Rayleigh's criterion predicts an instability of the second acoustic mode of the tube at a frequency of approximately 180 Hz, and that instability is observed experimentally.

A SenSym resistive-based pressure transducer was used to collect sound pressure data from this 180 Hz instability. This signal was sent through a strain gauge amplifier, then was band-pass filtered between 160 and 200 Hz. The signal was then sent to a dSpace DS1103 DSP board, sampling at 1600 Hz, and used by the minimization algorithms to determine adaptive filter coefficients. The output was passed through a smoothing filter at 185 Hz and into an amplifier. The amplified signal was delivered to a 3" speaker that was used to control the instability in the tube. A schematic of this system can be seen in Figure 5.1.

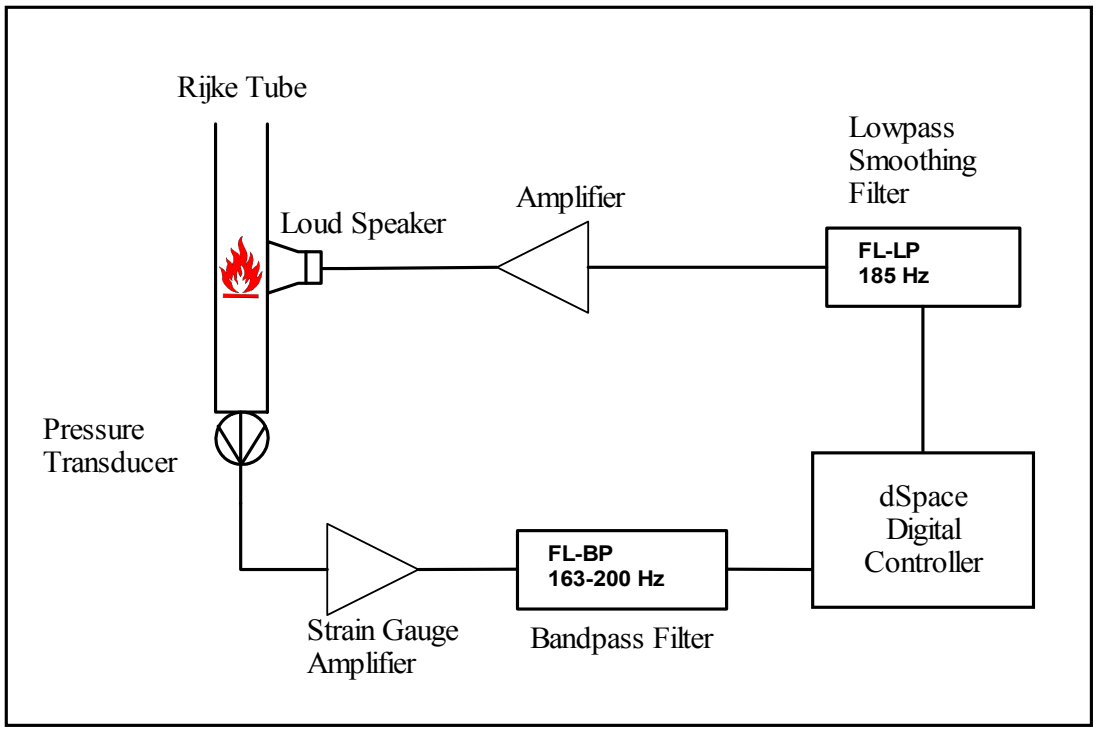

Figure 5.1 Rijke tube experimental set-up

Control tests were done in one of two actuation methods: proportional or pulsed (on-off) actuation signals. Proportional actuation involved a control signal that is proportional to the input pressure signal. Thus, the control effort is initially high, and decreases as control is achieved. Pulsed control, on the other hand, involves control signals of fixed amplitude. The pulsed experiments also include the use of sub-harmonic control. This is done by forcing the actuator at frequencies that are integer divisions of the fundamental instability frequency. Control is still possible because these signals contain a harmonic component at the instability frequency. Sub-harmonic control may be used to extend component life by exposing the actuator to fewer cycles. A more detailed description of the theory behind sub-harmonic control can be found in Carson [5].

Inherently, superior performance can be achieved by proportional actuation because of a secondary limit cycle present in pulsed control. This phenomenon is demonstrated in Section 5.4. The motivation for studying pulsed actuation is twofold. Pulsed actuators are more prevalent and easier to construct than proportional actuators. Also, pulsed actuation allows for the possibility of sub-harmonic control discussed above, which may increase actuator life.

5.2 Algorithm Performance using Proportional Actuation

There were three separate operating conditions on the Rijke tube that were explored, each have a total flow of approximately 128 cc/sec. The first was a condition

in which the tube was at the lower end of the instability range. The equivalence ratio for this case was, $\Phi = 0.544$. The second condition was at a higher equivalence ratio of $\Phi = 0.582$. The final condition was at an equivalence ratio, $\Phi = 0.641$, which could not be successfully controlled due to restrictions in the actuator authority and will be discussed at the end of this section. Because of this actuator authority issue, higher equivalence ratio conditions were not investigated.

Because the Rijke tube exhibits basically a single frequency instability, only two filter coefficients are required to set the phase and magnitude of the control filter. This is shown through the equations derived in Chapter 4 for the magnitude and phase of the filter: $G(z) = w_0 z^{-1} + w_1 z^{-2}$:

$$\angle G = \tan^{-1}\left(\frac{-\left[w_0 \sin(\omega T) + w_1 \sin(2\omega T)\right]}{\left[w_0 \cos(\omega T) + w_1 \cos(2\omega T)\right]}\right)$$

$$|G| = \sqrt{\left[w_0 \cos(\omega T) + w_1 \cos(2\omega T)\right]^2 + \left[w_0 \sin(\omega T) + w_1 \sin(2\omega T)\right]^2}$$

It is desired to constrain the magnitude and phase of the filter at the instability frequency such that the control signal will destructively interfere with the physical feedback loop generating the instability. Because there is a single frequency that is relevant in this case, there is only a single magnitude and phase to constrain. As can be seen from the above equations, this results in the need for a filter with only two taps. Thus, unless otherwise stated, it can be assumed that two weights have been used to obtain the following results.

5.2.1 Low Equivalence Ratio Case

The first of the operating conditions for the Rijke tube was a relatively low equivalence ratio of 0.544 with limit cycle frequency of 178 Hz at a level of 4.65 dBVrms. The power spectrum of this operating condition can be seen in Figure 5.2 and traces of the pressure oscillations are shown in Figure 5.3.

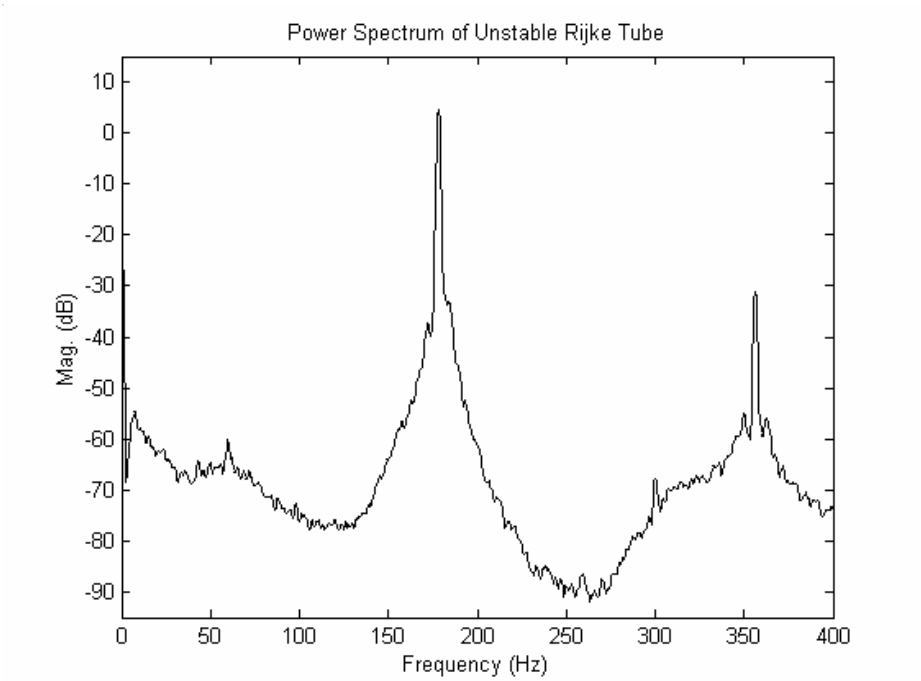

Figure 5.2 Power spectrum of Rijke tube, Φ = 0.544

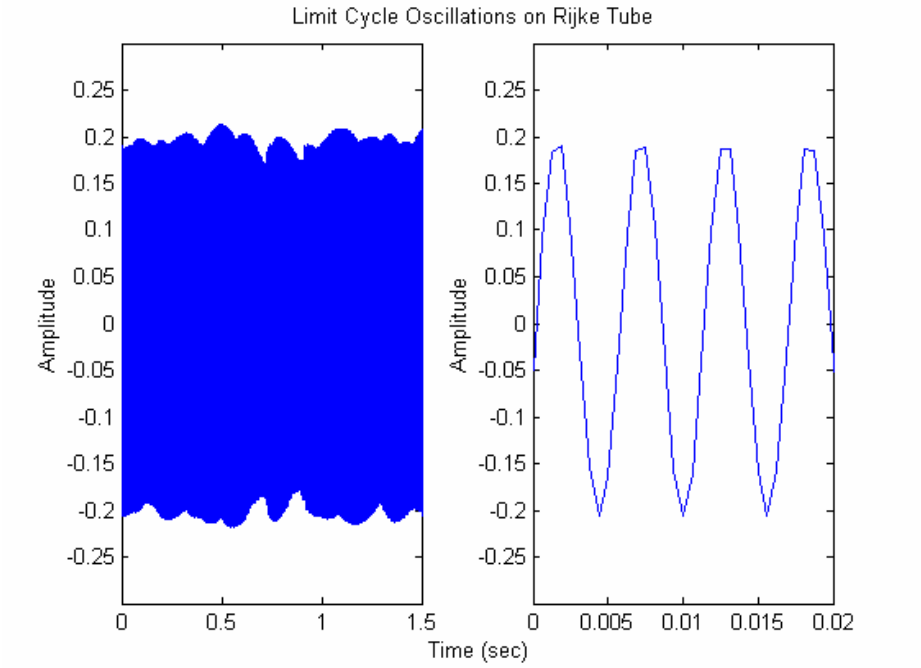

Figure 5.3 Limit cycle oscillations of Rijke tube, Φ = 0.544

A simple phase shift controller was used to insure that the system could be controlled with the control structure and to give a baseline for where the adaptation should converge. The results of using a phase shifter for this operation condition can be seen in Figure 5.4.

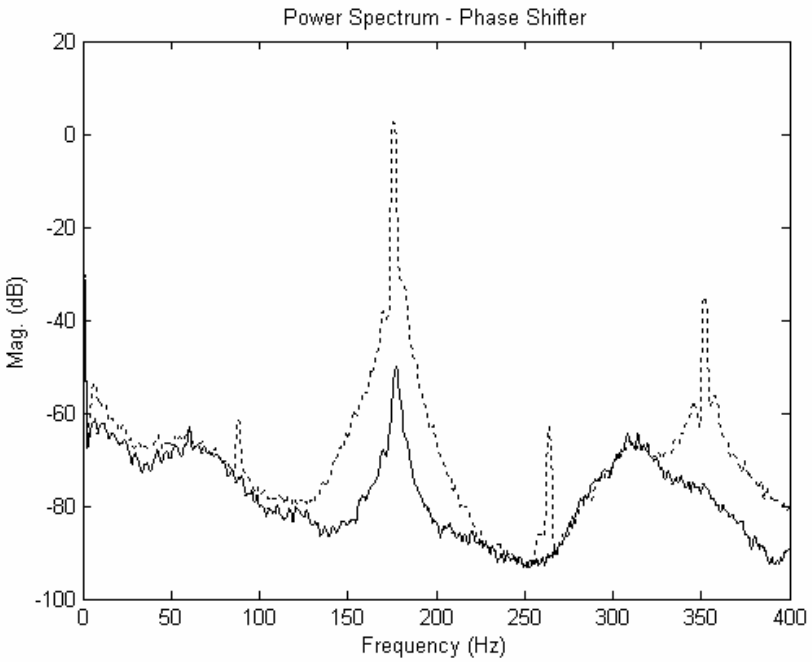

Figure 5.4 Power spectrum of Phase Shift-controlled Rijke tube, Φ = 0.544

The shift in phase for this controller is achieved by reading the input signal, holding this value for a specified number of samples, and then outputting the input signal scaled by a magnitude multiplier. For this condition the phase shifter was tuned manually and it was found that the best attenuation occurred at a delay of 13 samples. For this controller, the sample rate was 3200 Hz. Thus for a 180 Hz signal, the phase shift was approximately 97°, with a magnitude of 0.519. The relationship between the phase shift controller and the adaptive algorithms will be discussed in detail later in the section.

The tuning phase that was described in Chapter 3 was used to determine acceptable values of μ, δ, and N, the results of which can be seen in Table 5-1 (the value for μ was based on 15% of the upper limit). Refer to Section 3.3.2 for the tuning procedure and the impact of each of these parameters.

Table 5-1 Parameter values for the low Φ case

Equivalence Ratio, Φ	0.544
Convergence Parameter, μ	6.30
Perturbation Size, δ	0.1644
Integration Length, N	402 samples

For each algorithm, data for the decay envelope, the weight trajectories, the magnitude and phase of the filter, the frequency response of the steady-state weights, and the power spectra of the controlled pressure in the tube were collected. Plots for

magnitude and phase and the power spectra are shown below, while the remainder of the plots are provided in Appendix B.

The transient response, phase and magnitude, and power spectrum for the TAG algorithm control at the Φ = 0.544 equivalence ratio condition are shown in Figure 5.5 and Figure 5.6.

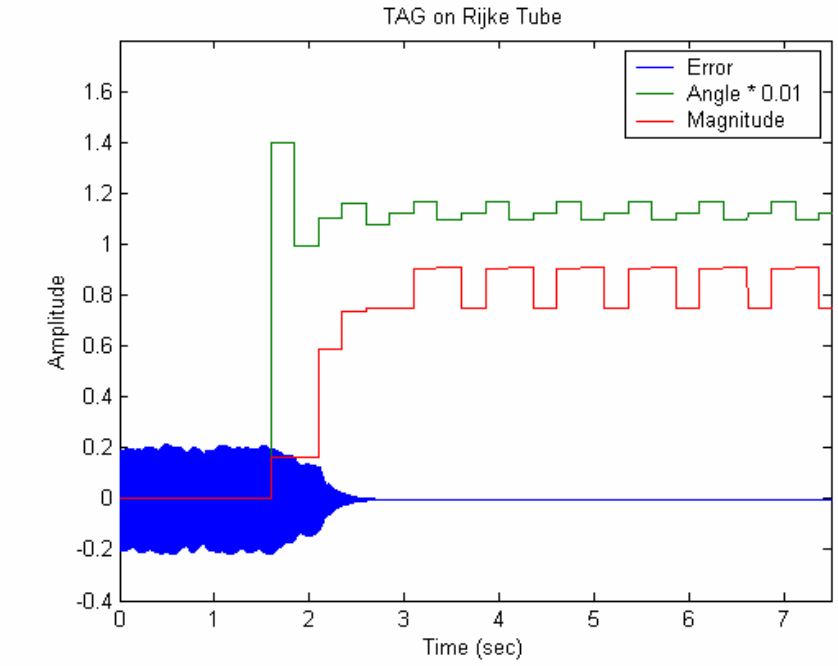

Figure 5.5 Phase (degrees) and linear magnitude of filter for TAG algorithm, Φ = 0.544

Refer to Section 4.2 for the conversion from filter weights to angle and phase of the filter.

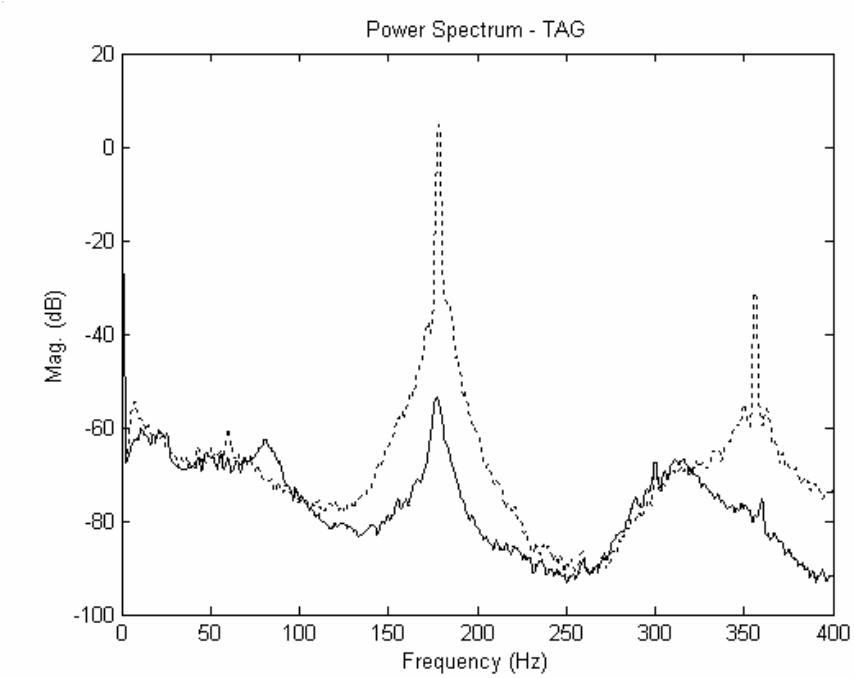

Figure 5.6 Power spectrum of TAG-controlled Rijke tube, Φ = 0.544

The TAG algorithm was able to produce satisfactory attenuation of the pressure signal, along with a reasonable convergence time. Figure 5.5 shows that the magnitude and phase of the controller do not reach a steady-state value. This is because the algorithm continuously perturbs the system to calculate a gradient, which causes continuous, small fluctuations in the magnitude and phase.

The results of the Gradient algorithm for this same operating condition are presented in Figure 5.7 and Figure 5.8.

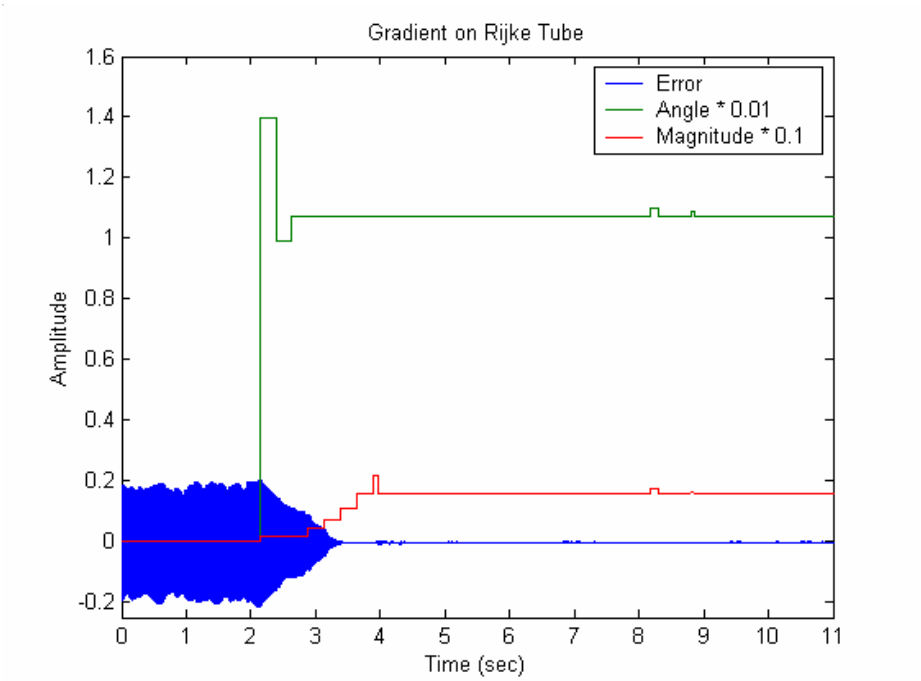

Figure 5.7 Phase (degrees) and linear magnitude of filter for Gradient algorithm, Φ = 0.544

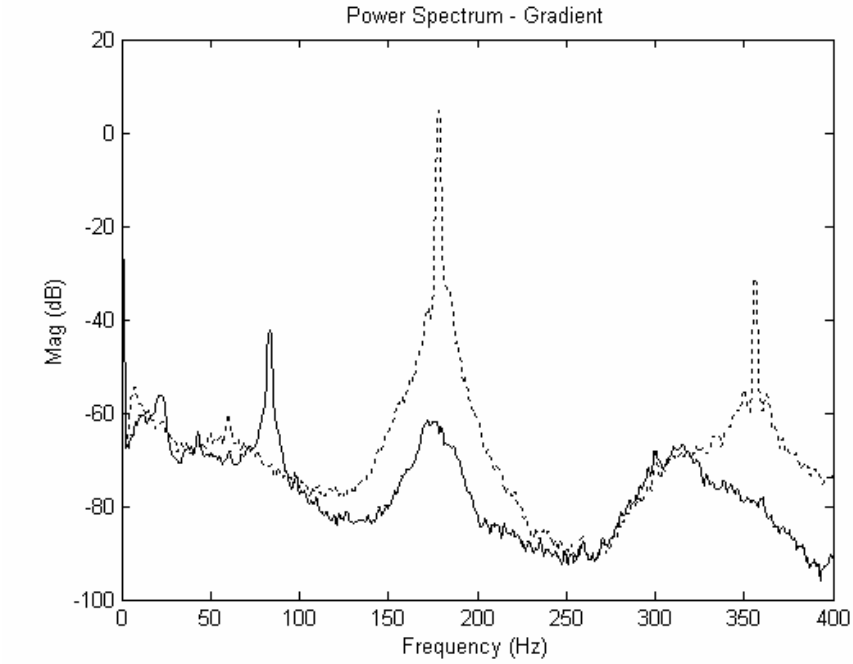

Figure 5.8 Power spectrum of Gradient-controlled Rijke tube, Φ = 0.544

The Gradient algorithm, too, performed well at this condition. It is important to note that the dominant energy component in the power spectrum has shifted from the initial limit cycling frequency of approximately 180 Hz to the second sub-harmonic frequency of 90 Hz. This is a result of using a bandpass filter on the pressure signal. A narrow bandpass was used, and as a result the information at the subharmonics is filtered.

The Gradient algorithm does not see the growth at this frequency, thus does not adapt to reduce this signal component.

Results for the Conjugate algorithm are shown in Figure 5.9 and Figure 5.10.

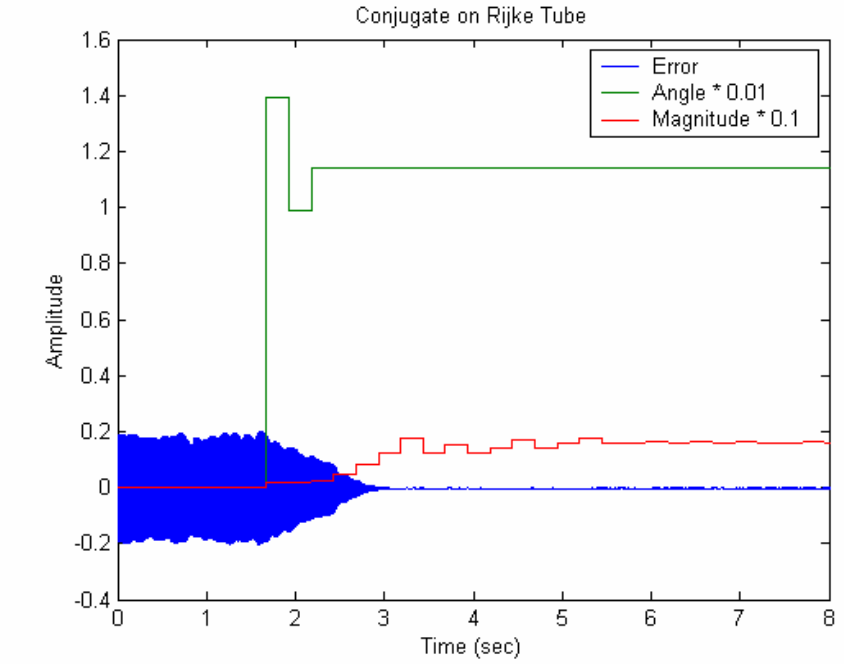

Figure 5.9 Phase (degrees) and linear magnitude of filter for Conjugate algorithm, Φ = 0.544

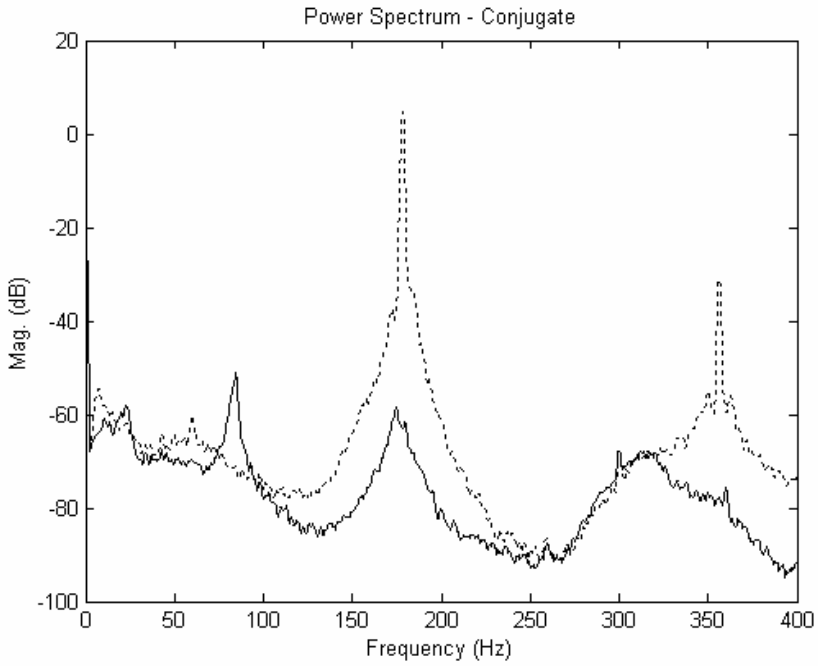

Figure 5.10 Power spectrum of Conjugate-controlled Rijke tube, Φ = 0.544

Results for the Conjugate algorithm are very similar to that of the Gradient algorithm, including the dominant energy component shifting to a sub-harmonic frequency.

The results for the first of the pattern search algorithms, Hooke and Jeeves, can be seen in Figure 5.11 and Figure 5.12.

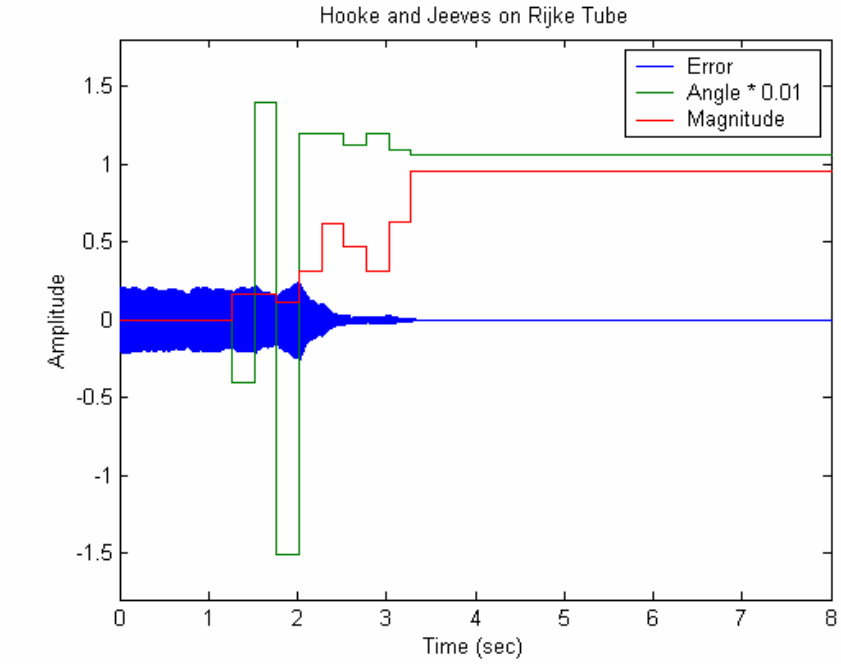

Figure 5.11 Phase (degrees) and linear magnitude of filter for Hooke and Jeeves algorithm, Φ = 0.544

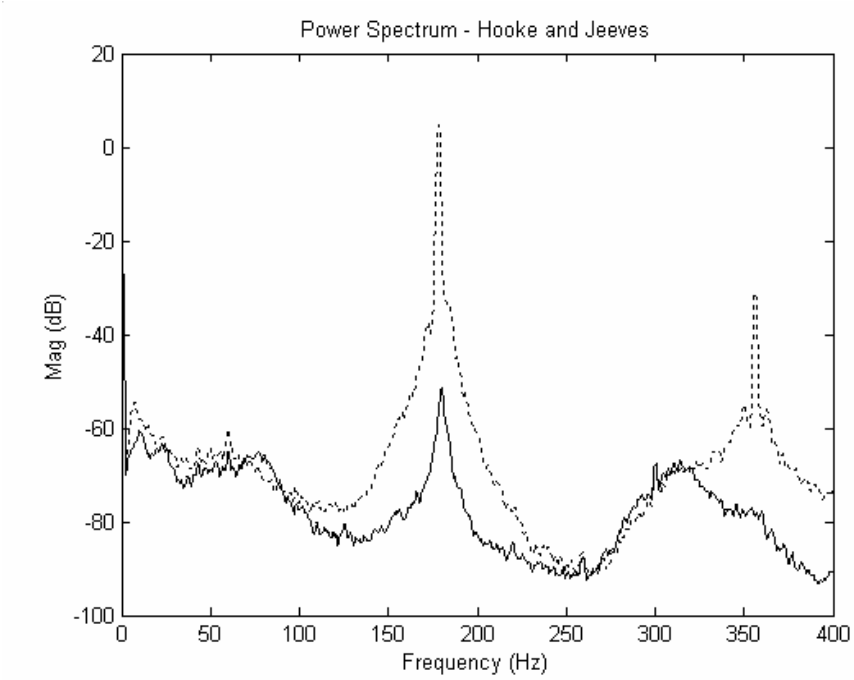

Figure 5.12 Power spectrum of Hooke and Jeeves-controlled Rijke tube, Φ = 0.544

The transient response for the Hooke and Jeeves pattern search is noticeably different from the gradient descent algorithms shown earlier. By calculating a gradient, the gradient descent algorithms guarantee that the pressure will not increase. This is not the case with the pattern searches, because they are simply systematically searching the weight space, and thus may take steps in the non-optimal direction. This results in a decay that is not completely smooth, and possibly a longer convergence time.

The results for the final algorithm, Rosenbrock, are shown in Figure 5.13 and Figure 5.14.

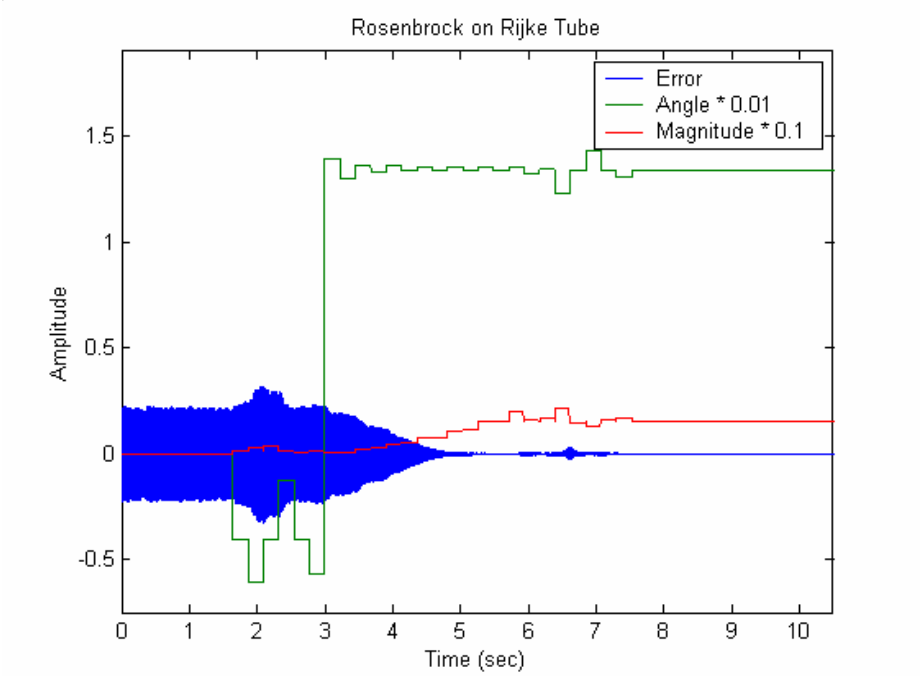

Figure 5.13 Phase (degrees) and linear magnitude of filter for Rosenbrock algorithm, Φ = 0.544

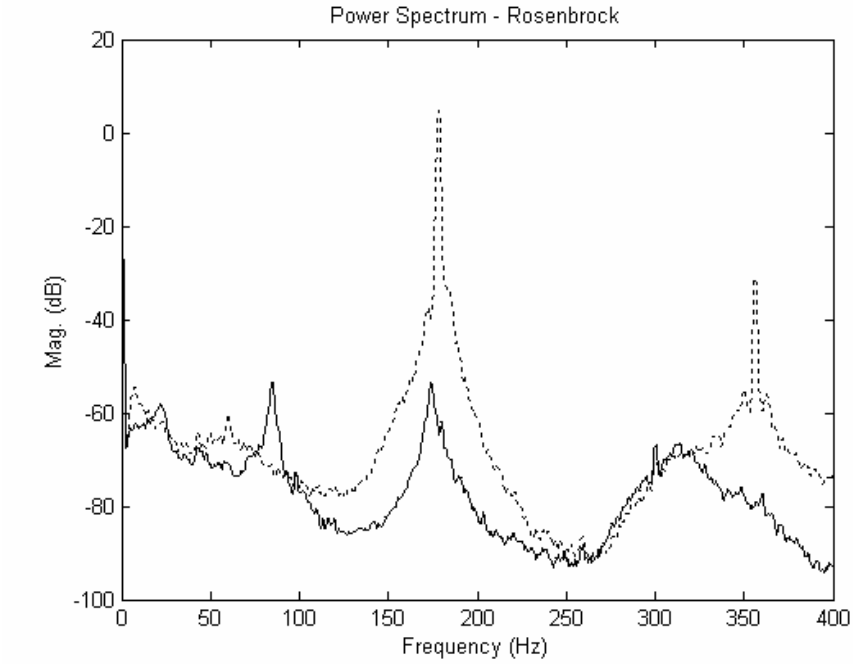

Figure 5.14 Power spectrum of Rosenbrock-controlled Rijke tube, Φ = 0.544

Because both are pattern searches, the statements related to the transient response of the Hooke and Jeeves algorithm also apply to the Rosenbrock algorithm.

The convergence times, ultimate attenuation, and the phase and magnitude of the controllers for each of the algorithms at this operating condition are tabulated in Table

5-2. For the low equivalence ratio case, each algorithm was successful in gaining control of the thermoacoustic instability. On average, there was about 60 dB of attenuation and a convergence time of approximately 2 seconds. Table 5-2 again demonstrates that the gradient descent algorithms outperformed the pattern search algorithms with respect to convergence time. The Rosenbrock and Hooke and Jeeves results show that these algorithms may take steps in the non-optimal direction and thus produce temporary growth in the pressure oscillations during the convergence process.

Table 5-2 shows that the adaptive algorithms have converged to a filter with magnitude greater than that of the phase shift controller. This suggests that the algorithms may continue to increase that gain of the controller in an attempt to increase the performance. Also note that the attenuation of the phase shifter is slightly less than that of the adaptive algorithms. This may be a result of the phase resolution of the phase shift controller. As mentioned earlier, the phase shifter uses the input signal delayed by some number of samples. With a 180 Hz instability and a sampling frequency of 3200 Hz, one sample corresponds to 20.25° of phase shift. The adaptive algorithms, however, can achieve much higher resolution through the ratio of the two filter weights, as given in Equation 5.1.

Table 5-2 Convergence times and ultimate attenuation at limit cycle frequency for, Φ = 0.544 Case

Algorithm	Convergence Time	Ultimate Attenuation	Filter Magnitude	Filter Phase
Phase Shifter	N/A	52.9 dB	0.519	97°
TAG	1.343 sec.	58.1 dB	0.84	112°
Gradient	1.363 sec.	66.2 dB	1.59	107°
Conjugate	1.478 sec.	63 dB	1.61	114°
Hooke and Jeeves	2.219 sec.	56.1 dB	0.95	106°
Rosenbrock	3.852 sec.	58.2 dB	1.55	134°

5.2.2 Medium Equivalence Ratio Case

The second condition was at an equivalence ratio of 0.582. Figure 5.15 shows the power spectrum of this condition with the instability at nearly 180 Hz and a magnitude of approximately 8 dBVrms, while Figure 5.16 shows the envelope of the oscillations.

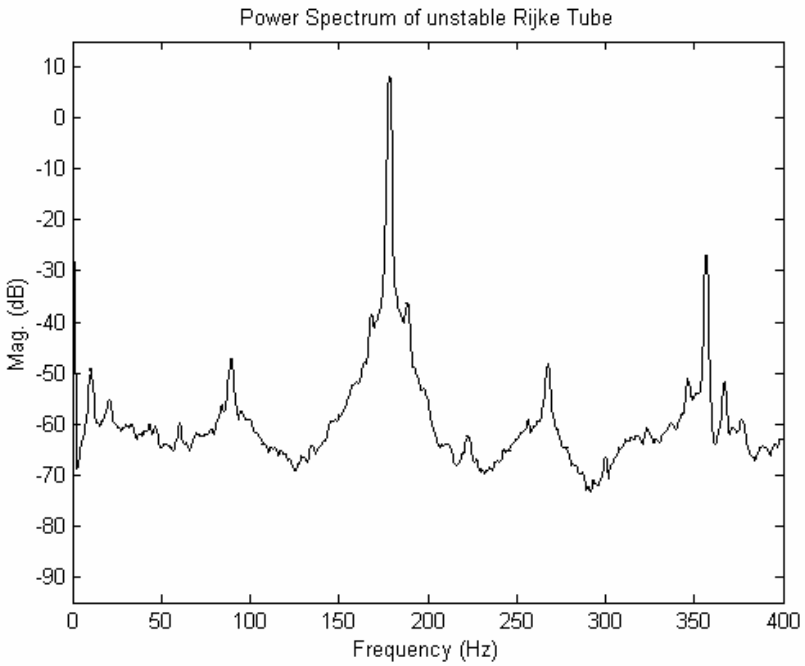

Figure 5.15 Power spectrum of Rijke tube, Φ = 0.582

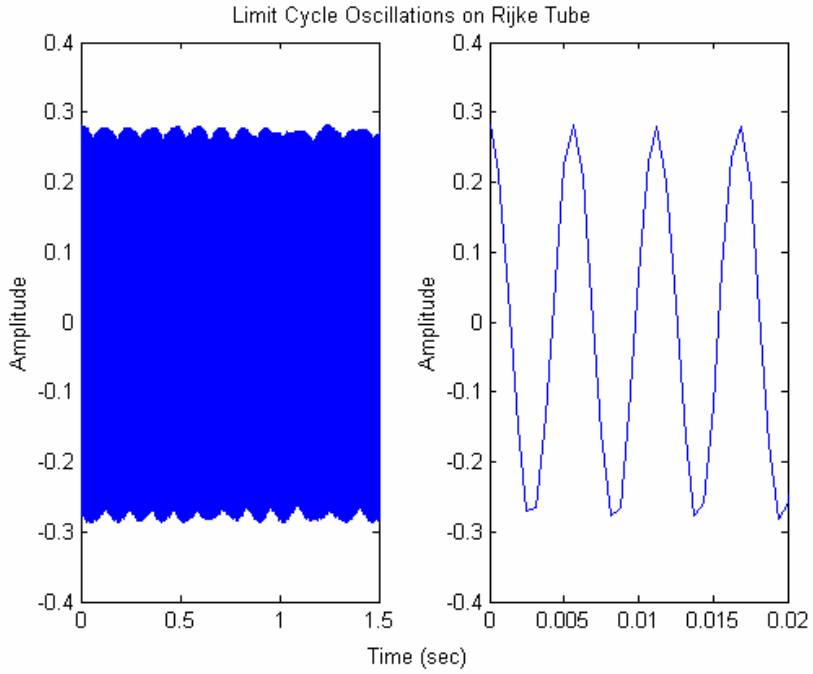

Figure 5.16 Limit cycle oscillations of Rijke tube, Φ = 0.582

The phase shift control results for the operating condition are shown in Figure 5.17. The tuning phase was run for this operating condition and the results are given in Table 5-3 and the resulting convergence times for this condition are given in Table 5-4.

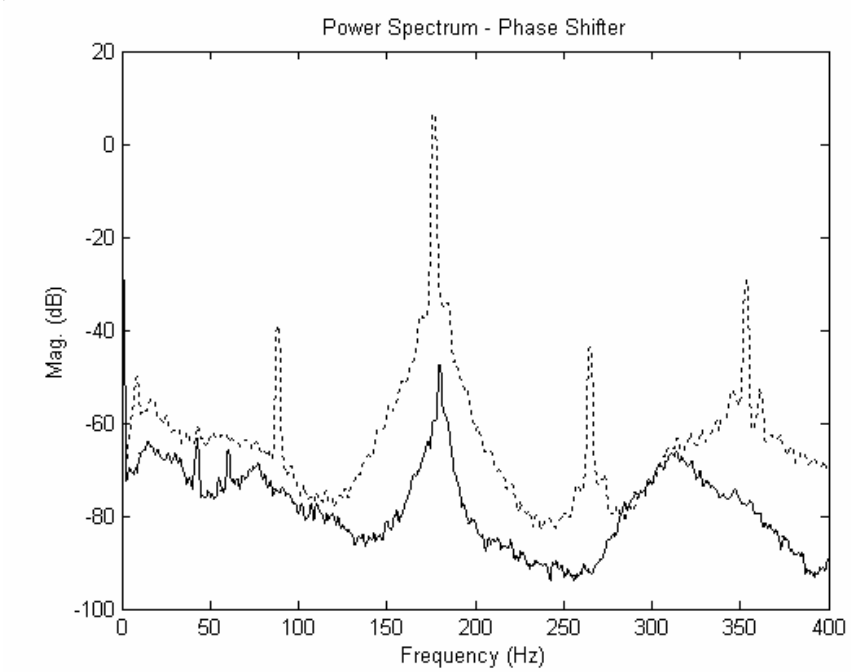

Figure 5.17 Power spectrum of Phase Shift-controlled Rijke tube, Φ = 0.582

Table 5-3 Parameter values for Φ = 0.582

Equivalence Ratio, Φ	0.582
Convergence Parameter, μ	3.165
Perturbation Size, δ	0.1621
Integration Length, N	361 samples

Raising the equivalence ratio to 0.582 did not negatively affect the performance of the algorithms. The results for this case, in fact, are very similar to that of the previous case. The results are shown in Figure 5.18 through Figure 5.40, encompassing each algorithm.

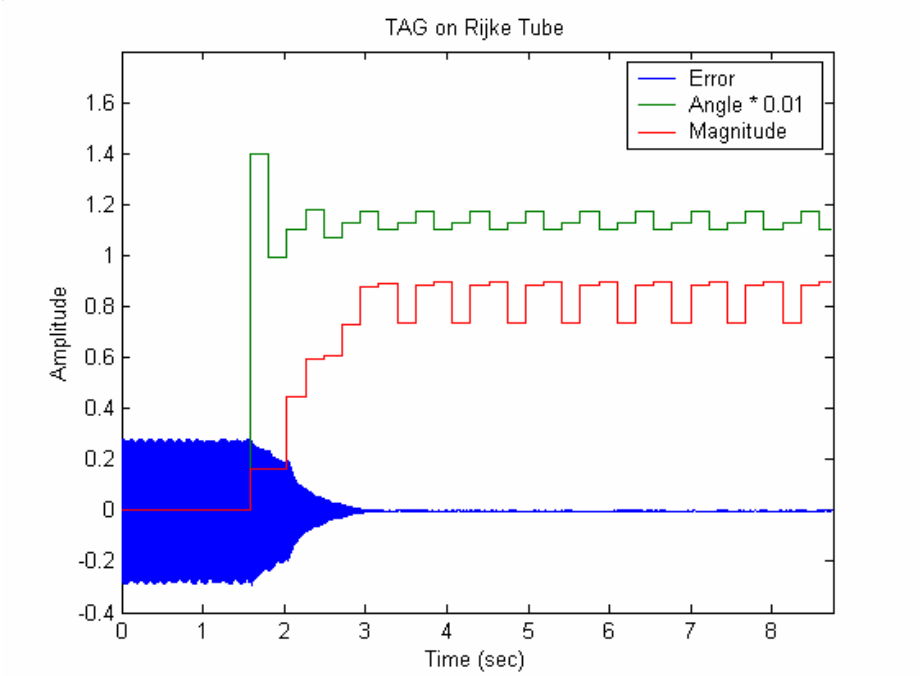

Figure 5.18 Phase (degrees) and linear magnitude of filter TAG algorithm, Φ = 0.582

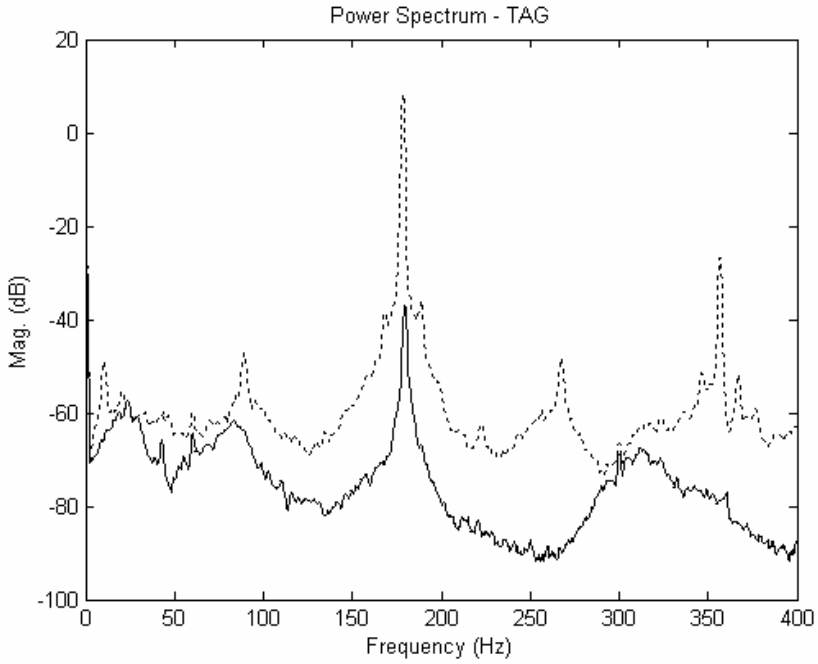

Figure 5.19 Power spectrum of TAG-controlled Rijke tube, Φ = 0.582

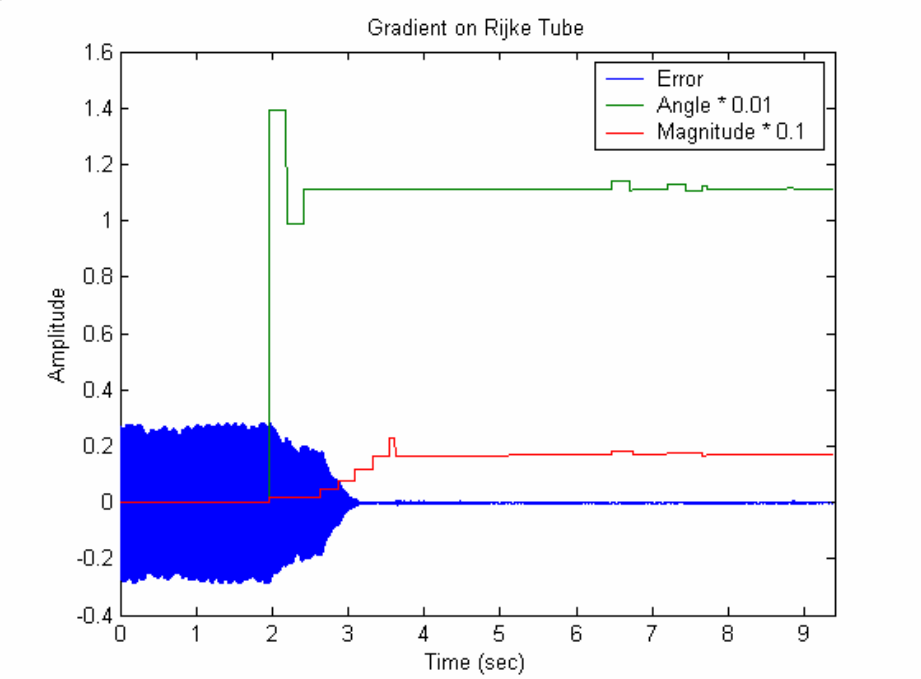

Figure 5.20 Phase (degrees) and linear magnitude of filter Gradient algorithm, Φ = 0.582

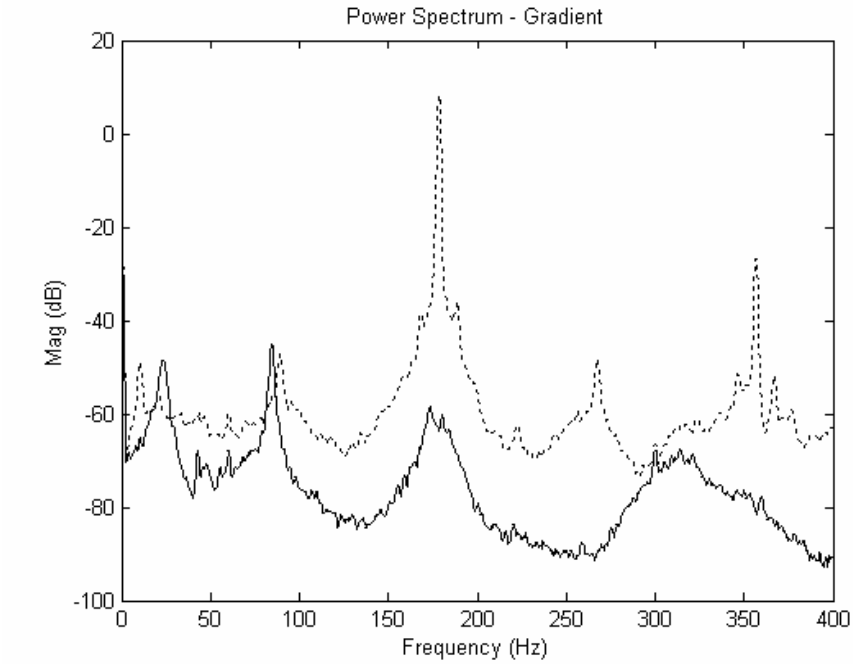

Figure 5.21 Power spectrum of Gradient-controlled Rijke tube, Φ = 0.582

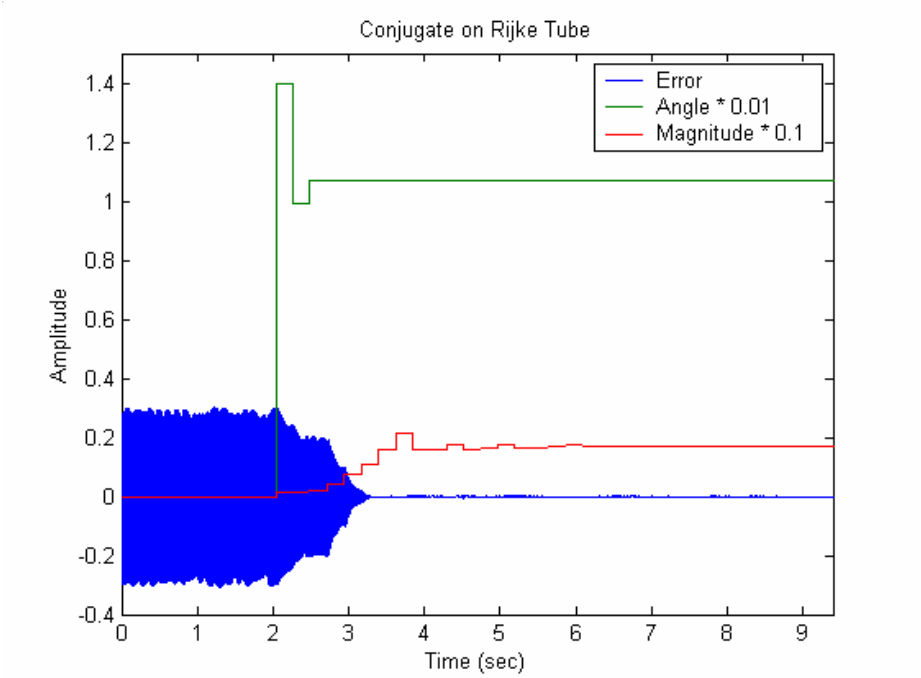

Figure 5.22 Phase (degrees) and linear magnitude of filter Conjugate algorithm, Φ = 0.582

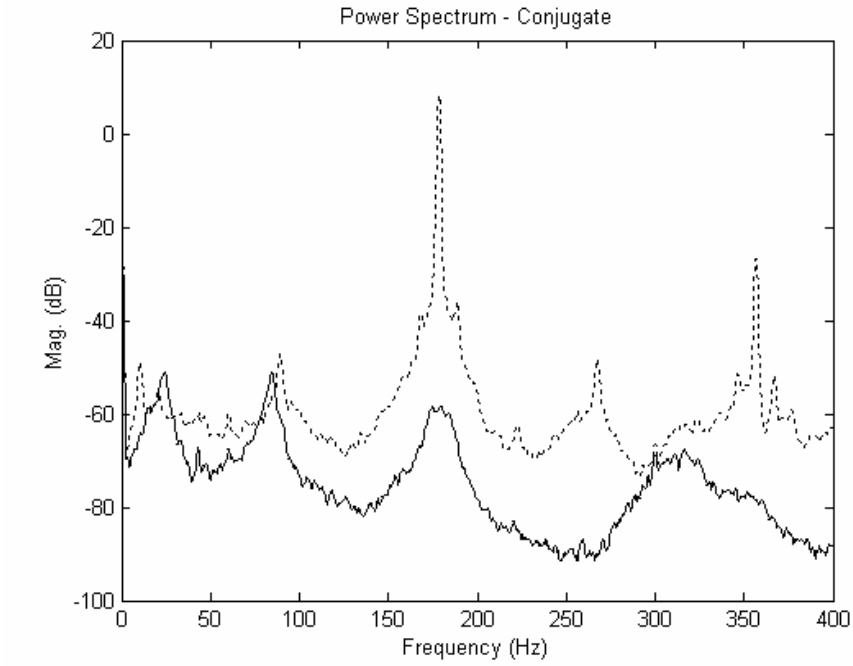

Figure 5.23 Power spectrum of Conjugate-controlled Rijke tube, Φ = 0.582

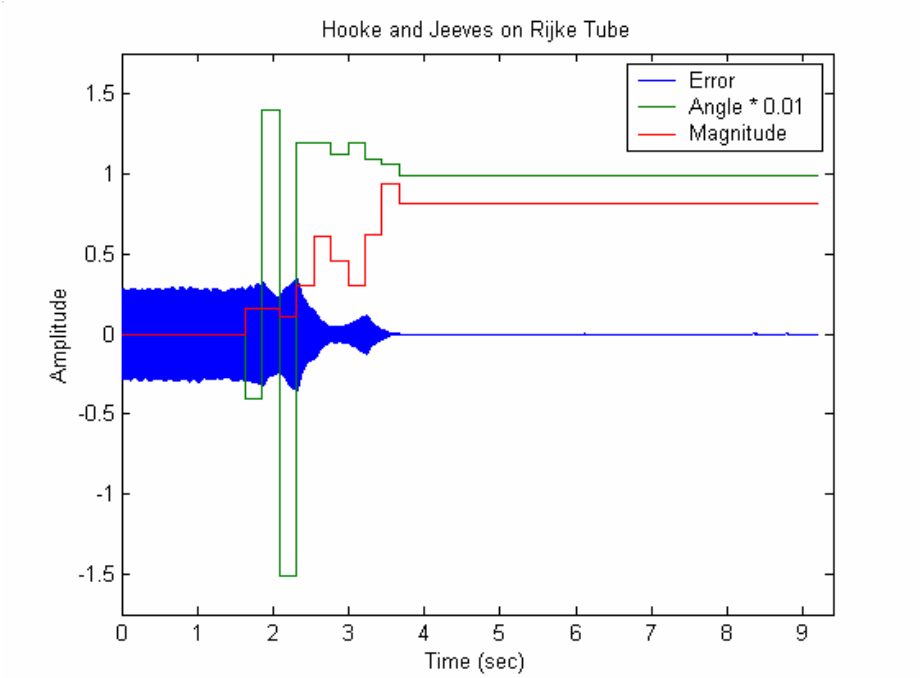

Figure 5.24 Phase (degrees) and linear magnitude of filter Hooke and Jeeves algorithm, Φ = 0.582

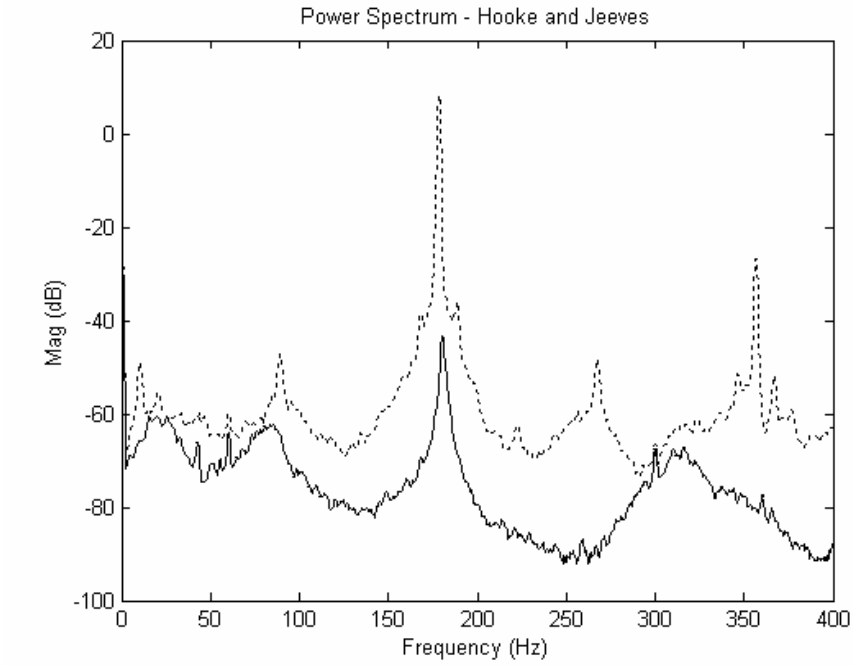

Figure 5.25 Power spectrum of Hooke and Jeeves-controlled Rijke tube, Φ = 0.582

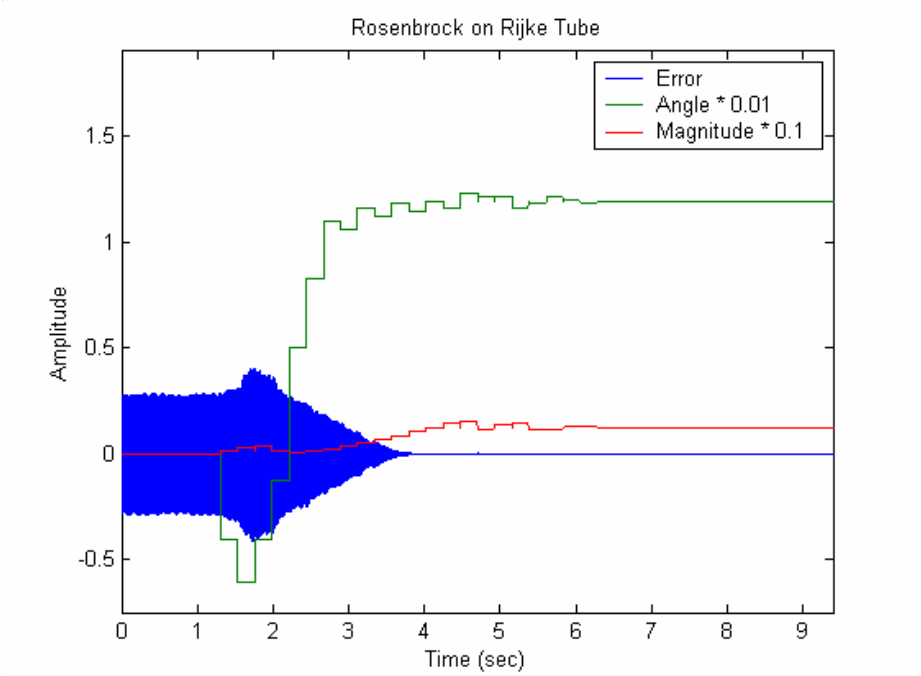

Figure 5.26 Phase (degrees) and linear magnitude of filter Rosenbrock algorithm, Φ = 0.582

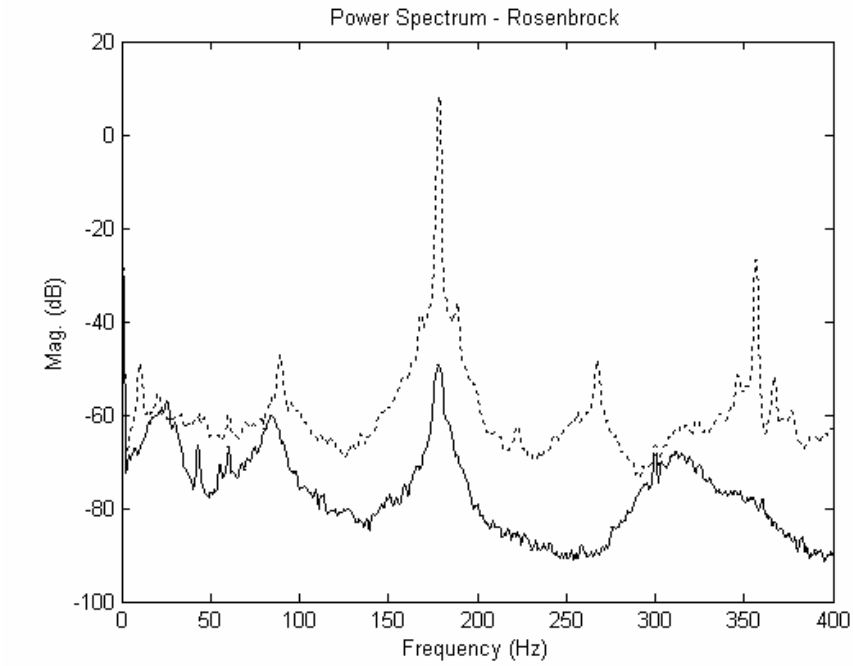

Figure 5.27 Power spectrum of Rosenbrock-controlled Rijke tube, Φ = 0.582

The results shown in the above figures are tabulated in Table 5-4, with the convergence time, ultimate attenuation, and magnitude and phase of the controller.

Table 5-4 Convergence times and ultimate attenuation at limit cycle frequency for Φ = 0.582

Algorithm	Convergence Time	Ultimate Attenuation	Magnitude	Phase
Phase Shifter	N/A	54.1 dB	1.25	97°
TAG	1.636 sec.	44.8 dB	0.81	114°
Gradient	1.407 sec.	66.1 dB	1.68	111°
Conjugate	1.315 sec.	65.8 dB	1.69	107°
Hooke and Jeeves	2.075 sec.	50.8 dB	0.81	99°
Rosenbrock	2.726 sec.	57.1 dB	1.25	119°

The magnitudes and phases that were developed by the algorithms for this operating condition are similar to those for the previous condition, and the attenuation ranged from nearly 50 dB to 65 dB. It is interesting to note that the TAG and Hooke and Jeeves algorithms actually produced filters with magnitudes lower than that of the phase shifter. Again, this is likely due to the fact that the phase resolution on the phase shifter is worse than that of the adaptive algorithms. The average convergence time for this case was 1.832 seconds, which is slightly lower than the low equivalence ratio case. This is most likely due to a shorter integration length for this condition. Again, the gradient descent methods proved to be more effective with respect to convergence time. No generalizations, however, can be made for which type of algorithm produced the greatest amount of attenuation. Additional results for each algorithm for this test case can be seen in Appendix C.

5.2.3 High Equivalence Ratio Case

The final condition that was tested on the Rijke tube was a high equivalence ratio of 0.641. This equivalence ratio produced the power spectrum in Figure 5.28 and the oscillation trace in Figure 5.29.

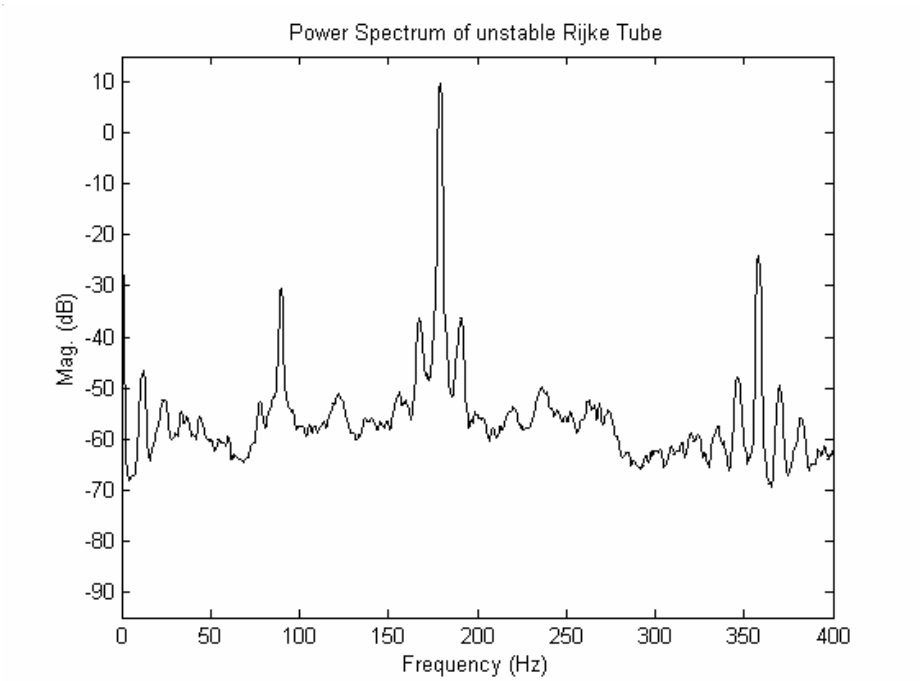

Figure 5.28 Power spectrum of Rijke tube, Φ = 0.641

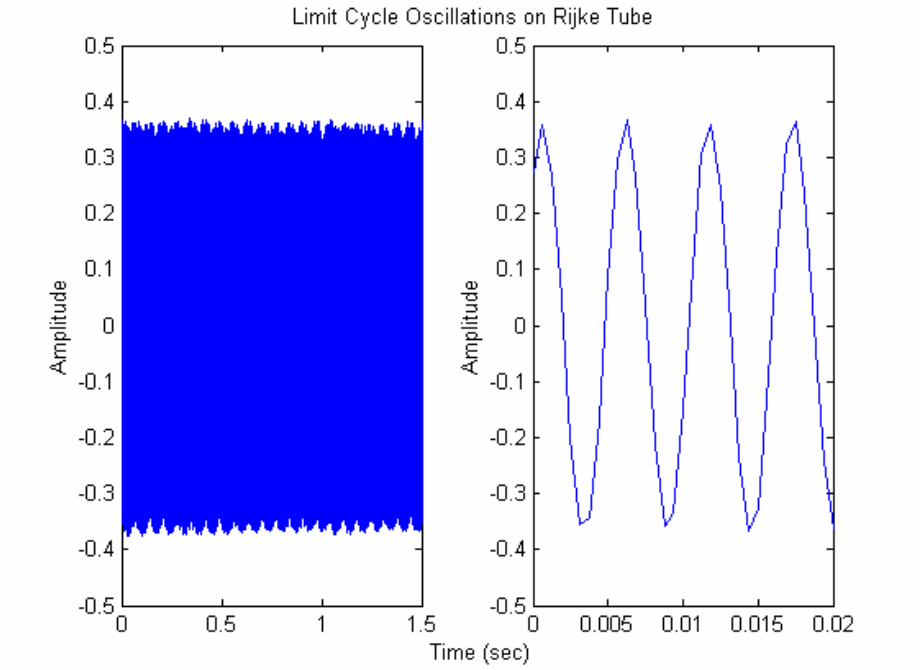

Figure 5.29 Limit cycle oscillations of Rijke tube, Φ = 0.641

The phase shift results are shown in Figure 5.30. The tuning phase was once again run and Table 5-5 outlines the results. Table 5-6 presents the convergence times of each algorithm for the high equivalence ratio operating condition.

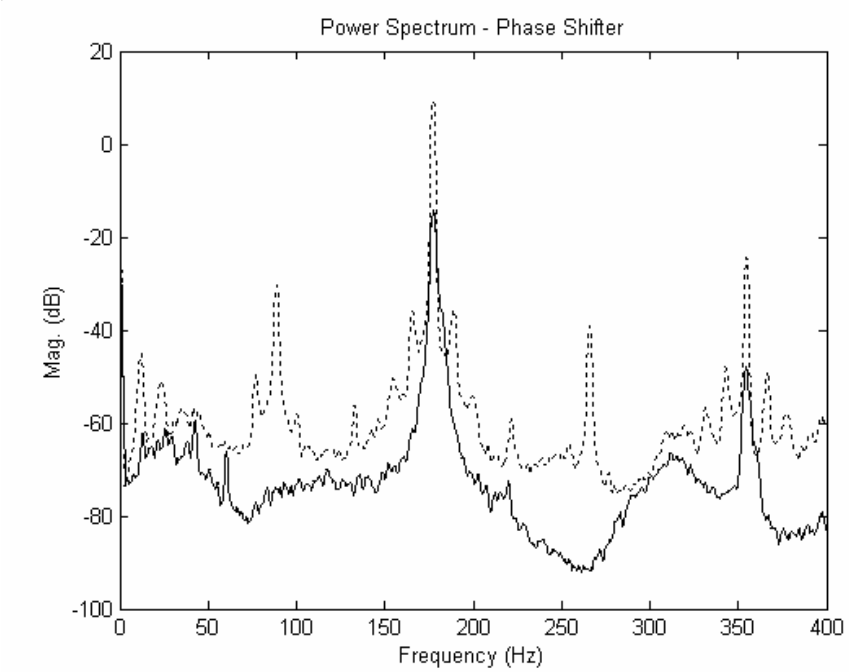

Figure 5.30 Power spectrum of Phase Shift-controlled Rijke tube, Φ = 0.641

Note that the performance of the phase shifter is considerably worse than the previous operating conditions. This will be discussed in detail later in the section.

Table 5-5 Parameter values for Φ = 0.641

Equivalence Ratio, Φ	0.641
Convergence Parameter, μ	2.363
Perturbation Size, δ	0.2736
Integration Length, N	341 samples

Results for the TAG algorithm on the high equivalence ratio condition are presented in Figure 5.31 and Figure 5.32. Note that control cannot be maintained for this condition. Initially, control is achieved, but then the system produces a series of bursts in the pressure signal. This phenomenon has been documented previously in Vaudrey [1], which states that the bursting is due to a combination of lack of actuator authority and a changing plant. As the flame becomes stable the heat release increases, which drives the poles further into the right half of the s-plane. At leaner conditions, there is still enough authority to maintain control over this increasingly unstable plant, but at richer conditions the actuator lacks this authority. As the system begins to lose control and become unstable, the heat release decreases. This allows the actuator to regain control, and the process repeats itself in the form of a series of bursts in the combustor pressure.

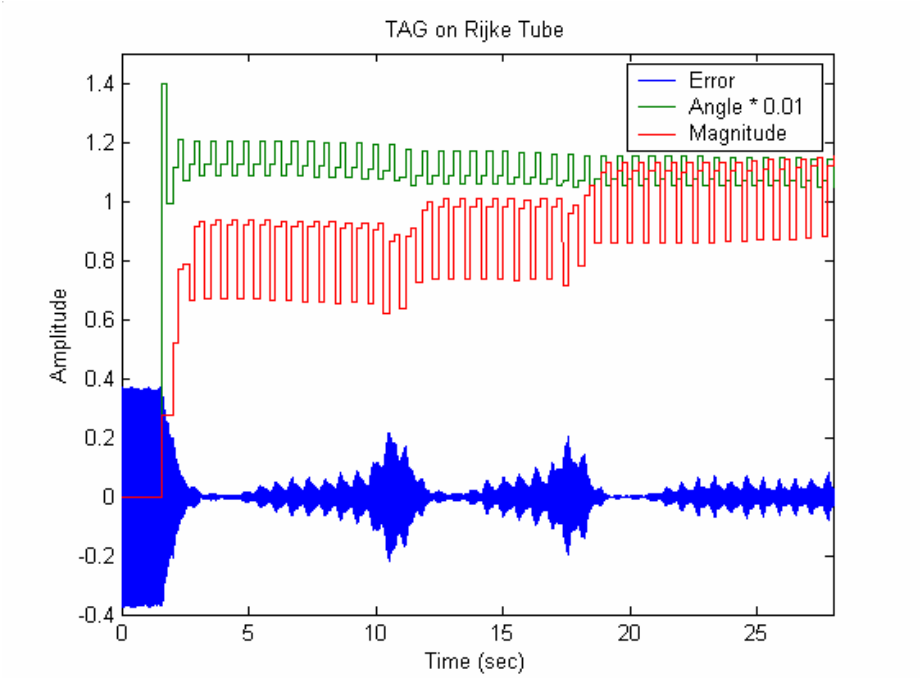

Figure 5.31Phase (degrees) and linear magnitude of filter TAG algorithm, Φ = 0.641

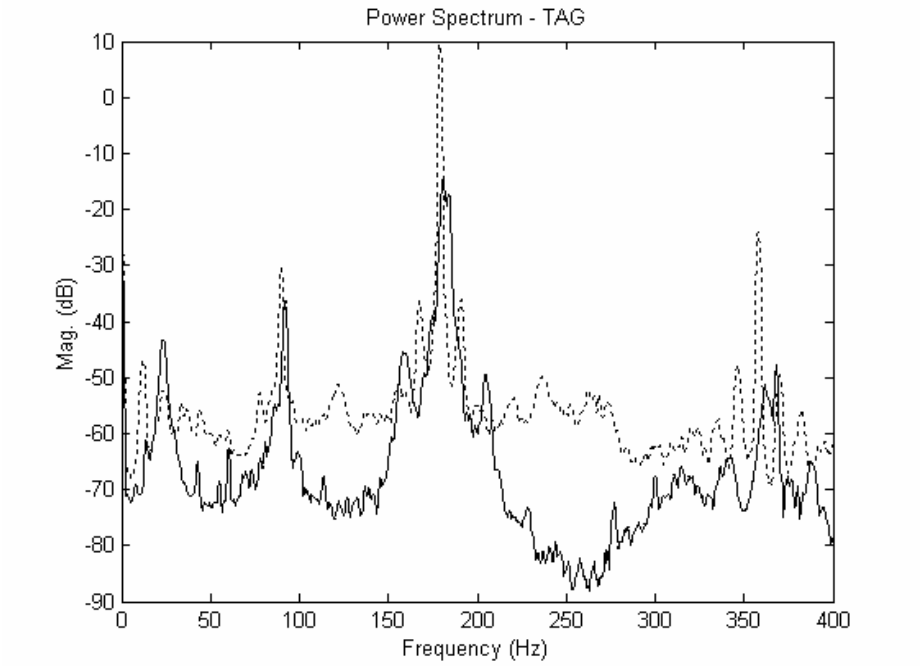

Figure 5.32 Power spectrum of TAG-controlled Rijke tube, Φ = 0.641

The results for the Gradient case are shown in Figure 5.33 and Figure 5.34, which also demonstrate a bursting behavior, though less severe than the TAG case.

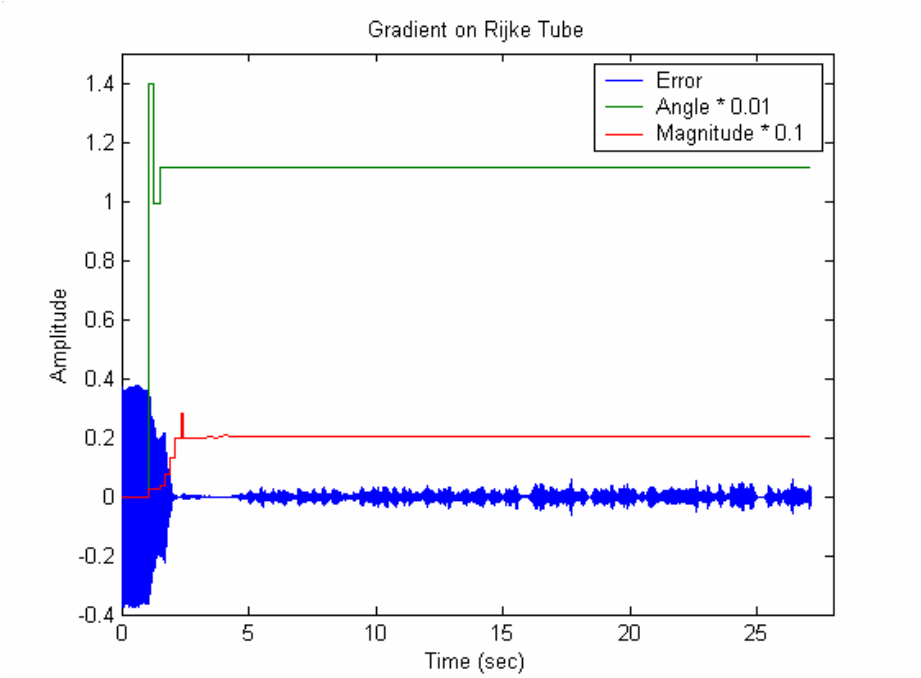

Figure 5.33 Phase (degrees) and linear magnitude of filter Gradient algorithm, Φ = 0.641

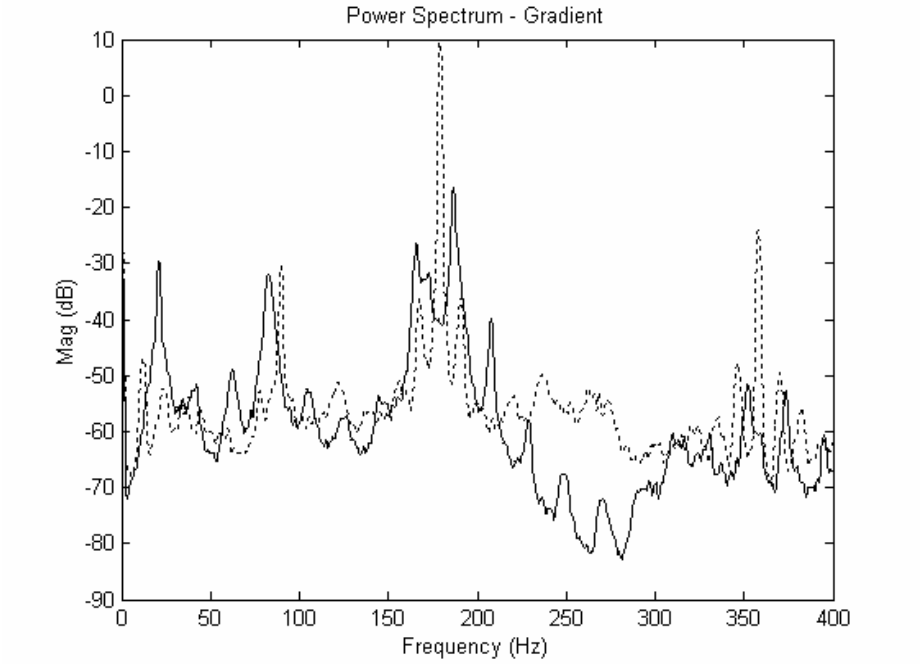

Figure 5.34 Power spectrum of Gradient-controlled Rijke tube, Φ = 0.641

Figure 5.35 and Figure 5.36 show the transient response and the power spectral density, respectively, for the Conjugate algorithm. The results of this test are very similar to that of the Gradient algorithm.

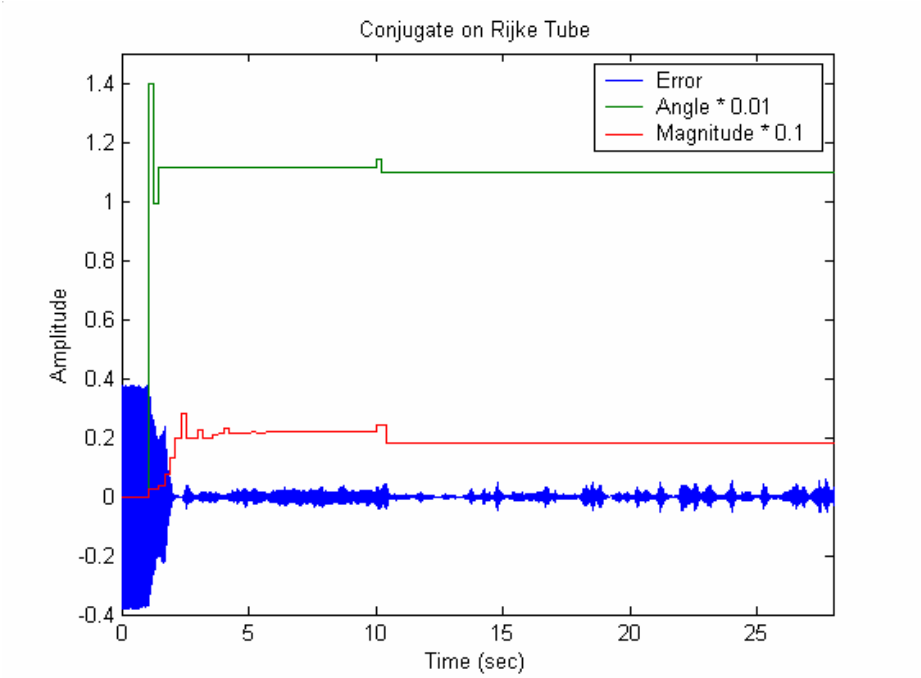

Figure 5.35 Phase (degrees) and linear magnitude of filter Conjugate algorithm, Φ = 0.641

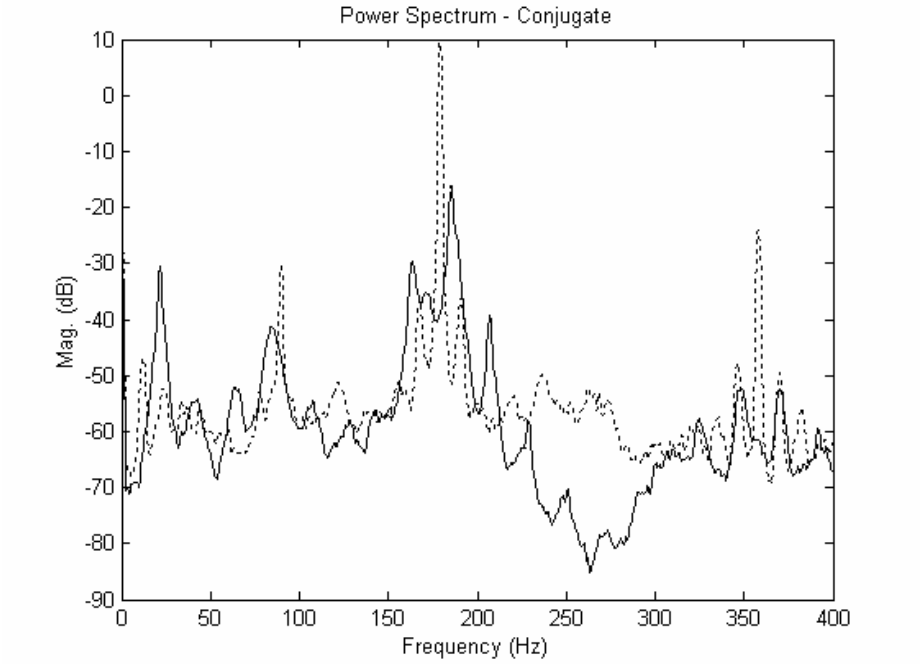

Figure 5.36 Power spectrum of Conjugate-controlled Rijke tube, Φ = 0.641

Performance for the Hooke and Jeeves algorithm is shown in Figure 5.37 and Figure 5.38. The amplitude of the pressure signal is greater for Hooke and Jeeves than for the previous gradient descent algorithms. This is also shown in the lack of attenuation in the power spectrum.

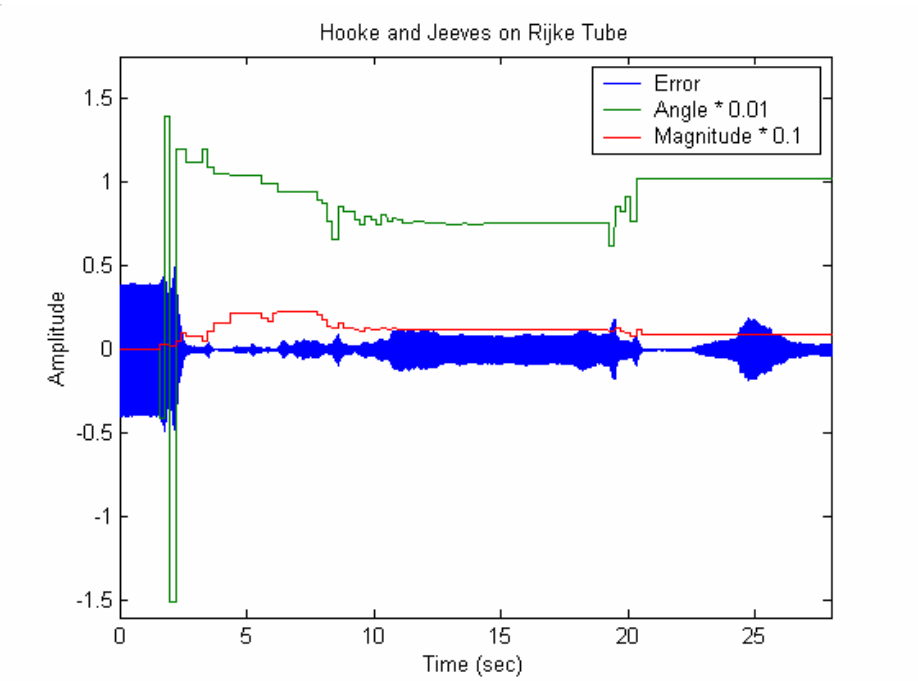

Figure 5.37 Phase (degrees) and linear magnitude of filter Hooke and Jeeves algorithm, Φ = 0.641

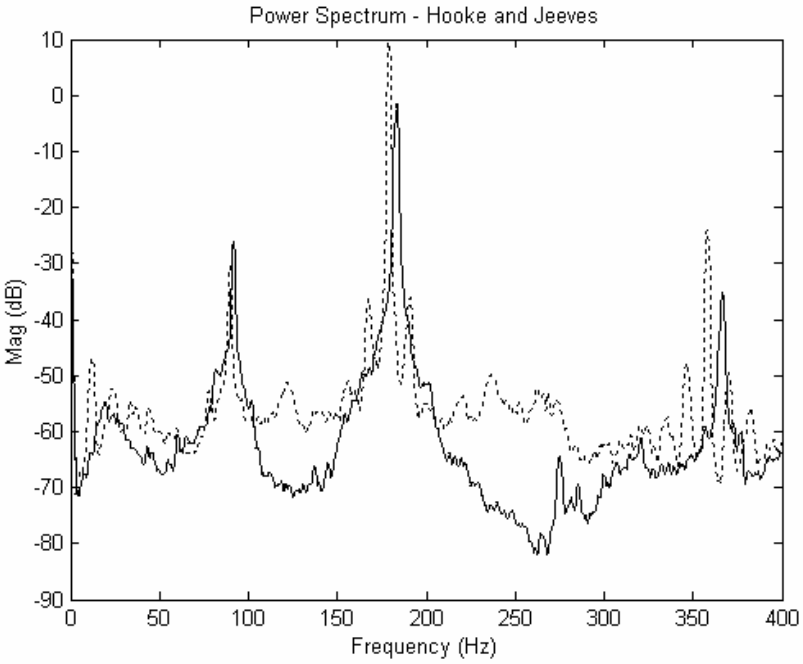

Figure 5.38 Power spectrum of Hooke and Jeeves-controlled Rijke tube, Φ = 0.641

Rosenbrock results are shown in Figure 5.39 and Figure 5.40.

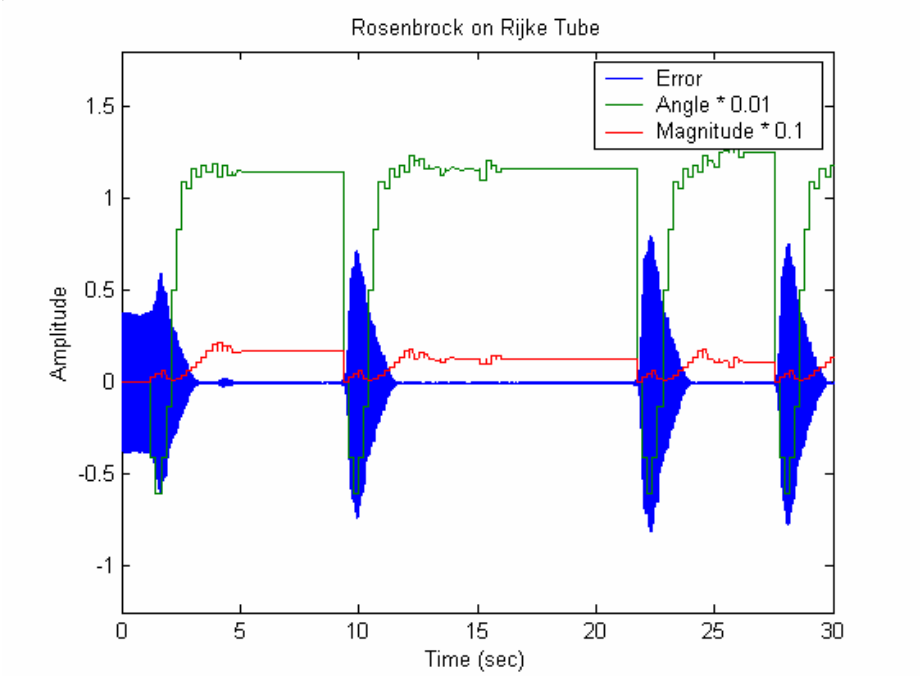

Figure 5.39 Phase (degrees) and linear magnitude of filter Rosenbrock algorithm, Φ = 0.641

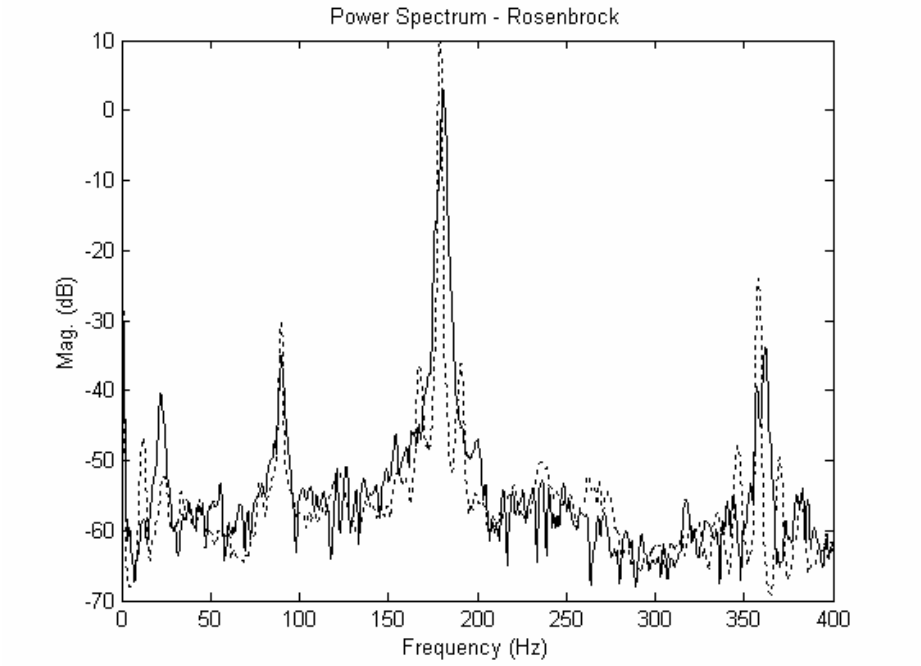

Figure 5.40 Power spectrum of Rosenbrock-controlled Rijke tube, Φ = 0.641

The transient response for the Rosenbrock algorithm shows extreme bursts in the pressure signal. The Rosenbrock algorithm searches the weight space and settles into a region that produces the lowest MSE of the pressure signal. The algorithm will begin to search again if a measurable increase in the MSE occurs. This is the reason that the

bursts for this algorithm are so severe. Instead of continually computing the gradient like the gradient descent algorithms, and thus gaining knowledge as the system changes, the Rosenbrock algorithm waits until the bursts occur and then descends upon the optimal answer again. In practice, these bursts would be very damaging to the lives of engine components.

Table 5-6 shows that the gradient descent methods proved to be more effective in this case with respect to the ultimate attenuation. Again, this is most likely due to the fact that these algorithms are continuously calculating a gradient, whereas the pattern searches are looking to settle into an optimal solution.

Table 5-6 Convergence times (in seconds) for Φ = 0.641

Algorithm	Convergence Time	Ultimate Attenuation	Magnitude	Phase
Phase Shifter	N/A	23.6 dB	1.645	117°
TAG	1.701 sec.	24.1 dB	N/A	N/A
Gradient	1.181 sec.	26 dB	2.02	111°
Conjugate	1.281 sec.	25.6 dB	1.89	145°
Hooke and Jeeves	2.193 sec.	11 dB	N/A	N/A
Rosenbrock	2.379 sec.	6.9 dB	N/A	N/A

The weight trajectories for each algorithm are located in Appendix D. The frequency responses of the steady-state weights are not shown for each algorithm for this case because, for many of the algorithms, bursting effects do not allow the weights to reach a steady state.

5.3 Proportional Actuation Discussion

It can be seen that the integration length, N, decreases with increasing equivalence ratio, from 402 for the low case to 341 for the high case. This is the expected result considering the plots of the limit cycling pressure signal. Figure 5.3 shows the trace of the low equivalence ratio case, and it shows that the amplitude of the oscillations is far from uniform. This is compared to Figure 5.16 for the medium case and Figure 5.29 for the high case, in which the envelope is much less sporadic. Thus, it can be concluded that the low equivalence ratio case should require the longest averaging time.

One would expect that the perturbation size, δ, would increase as the equivalence ratio increased. This is due to the fact that with an increase in equivalence ratio comes an increase in the limit cycle amplitude, thus a larger perturbation is required to achieve a measurable change in the MSE. The perturbation size stayed relatively constant from the low to medium case, but did increase substantially for the high case.

The convergence parameter, μ, was shown to be inversely proportional to the signal power in Chapter 3, thus should decrease with increasing Φ. This was, in fact, the outcome of the tuning phase. These trends can be seen graphically in Figure 5.41.

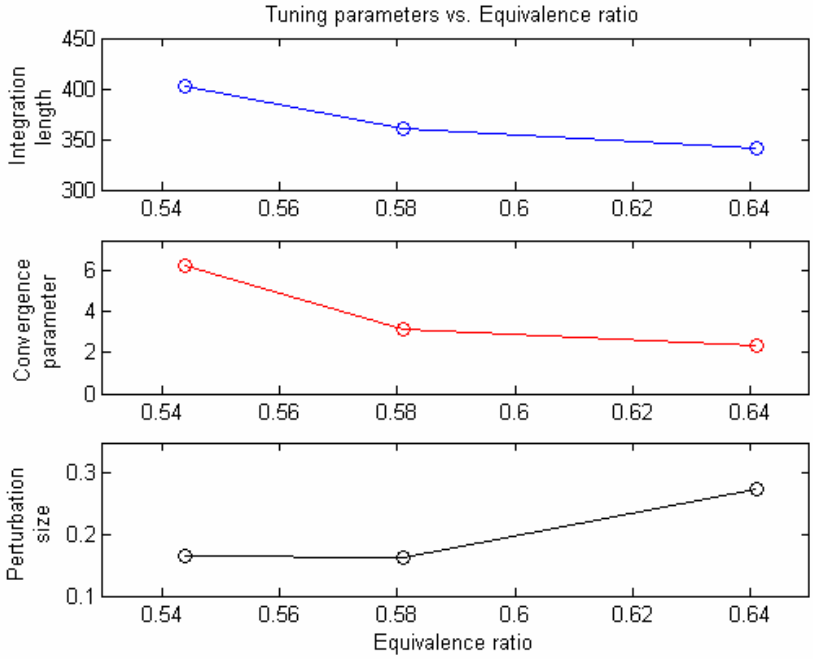

Figure 5.41 Tuning parameters vs. equivalence ratio

The proportional actuation tests on the Rijke tube combustor have shown that, in general, the gradient descent algorithms outperformed the pattern search algorithms. Although, the pattern search algorithms were able to suppress the pressure signal to level comparable to the gradient descent algorithms, the convergence time was lower for the gradient descent algorithms. These algorithms were also superior in the presence of actuator authority limitations.

5.4 Pulsed Actuation Results

For the following tests, the speaker was actuated in a pulsed, or on/off, fashion rather than the proportional manner in which it was driven in previous tests. The amplitude of the signal that was delivered to the audio amplifier was 1 volt. Actuation was at the fundamental frequency of the instability along with sub-harmonic frequencies. A single operating condition was used for these tests with a total flow of 128 cc/sec and Φ of 0.55. A plot of the power spectral density for this case can be seen in Figure 5.42.

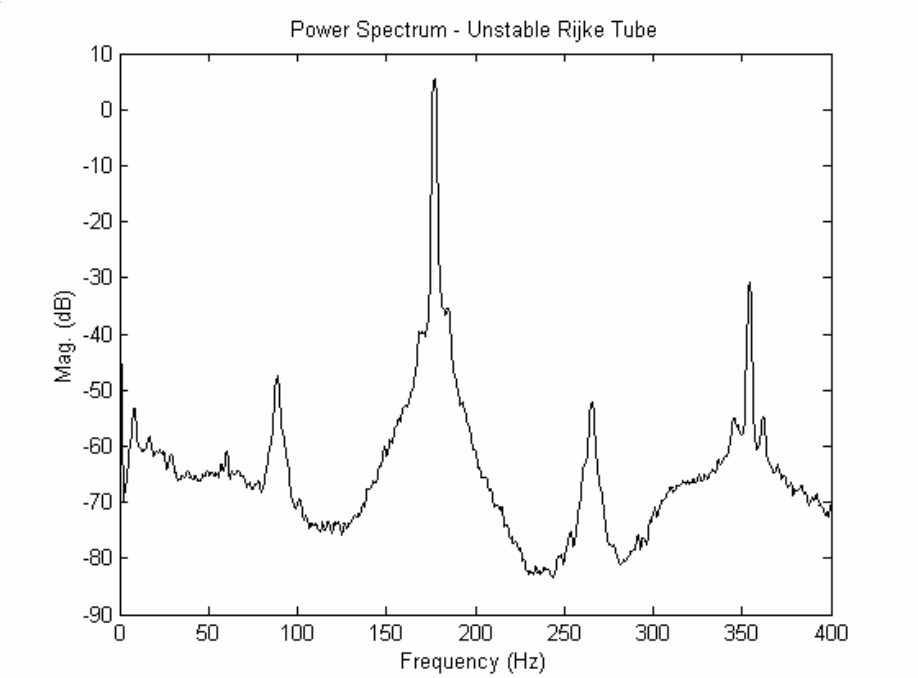

Figure 5.42 Power spectrum of unstable Rijke tube used during pulsed tests

Data was collected for actuation at the fundamental and the 2nd and 3rd sub-harmonic for each algorithm. The time traces pulsed at the fundamental frequency are shown below, and the other plots can be found in Appendix E. Higher order sub-harmonics were also explored, however this was done using only the Gradient algorithm. Power spectrums were captured for increasing sub-harmonics until control was lost. Data of the signal being sent to the actuator was also collected, in an attempt to explain the loss of control at higher sub-harmonics.

The results of the TAG algorithm with pulsed actuation are shown in Figure 5.43 and Figure 5.44. Note that the combustor pressure signal convergences very quickly and settles into a control-induced limit cycle because of the pulsed actuation. This is a general statement that may be extended to the rest of the gradient descent algorithms. As with proportional actuation, the pattern searches do not perform as well as the gradient descents with respect to convergence time. This is demonstrated in the plots in Figure 5.45 through Figure 5.52.

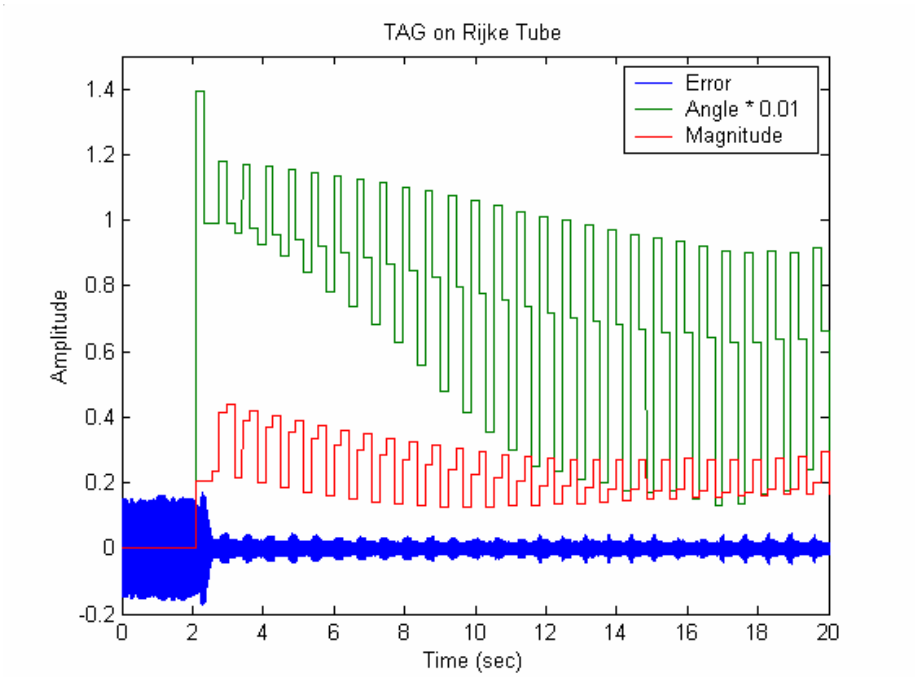

Figure 5.43 Phase (degrees) and linear magnitude of filter for TAG algorithm with pulsed actuation

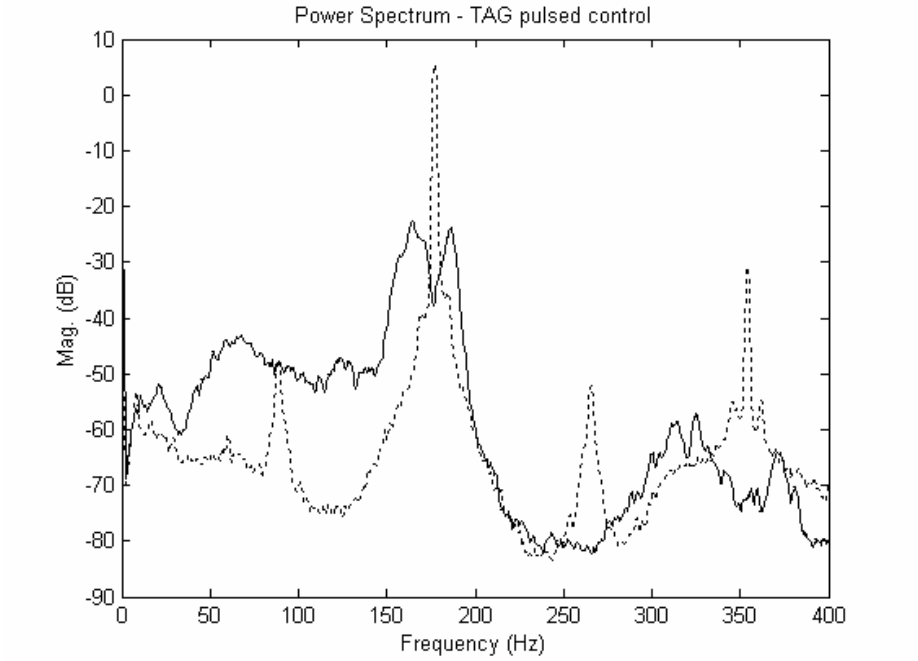

Figure 5.44 Power spectrum using TAG with pulsed actuation

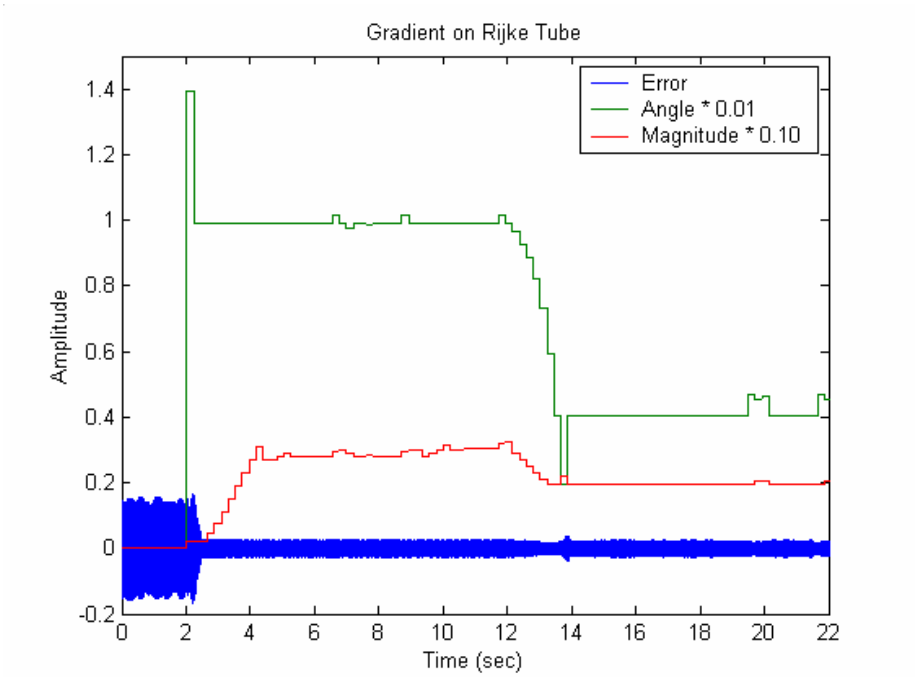

Figure 5.45 Phase (degrees) and linear magnitude of filter for Gradient algorithm with pulsed actuation

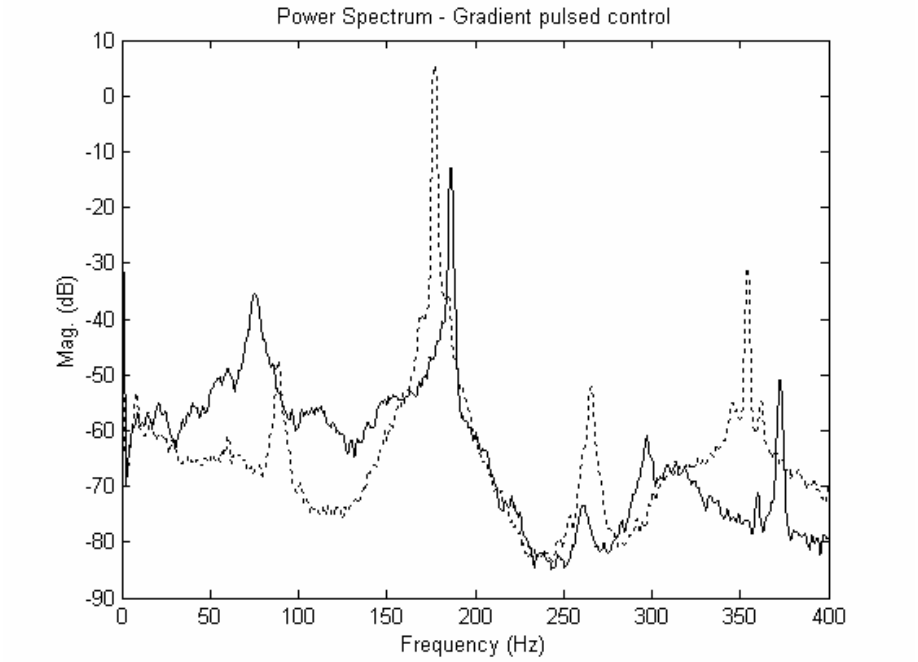

Figure 5.46 Power spectrum using Gradient with pulsed actuation

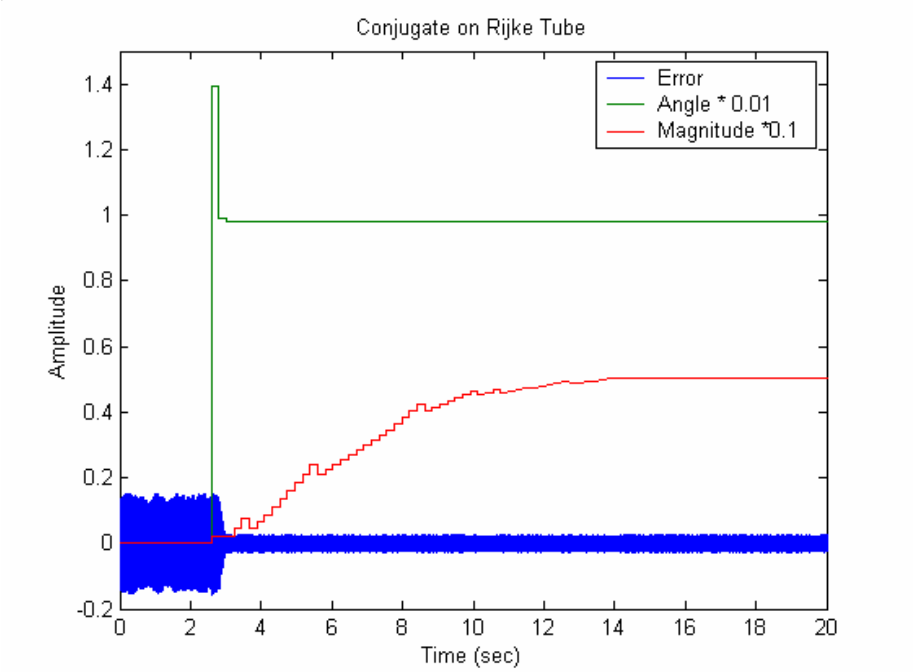

Figure 5.47 Phase (degrees) and linear magnitude of filter for Conjugate algorithm with pulsed actuation

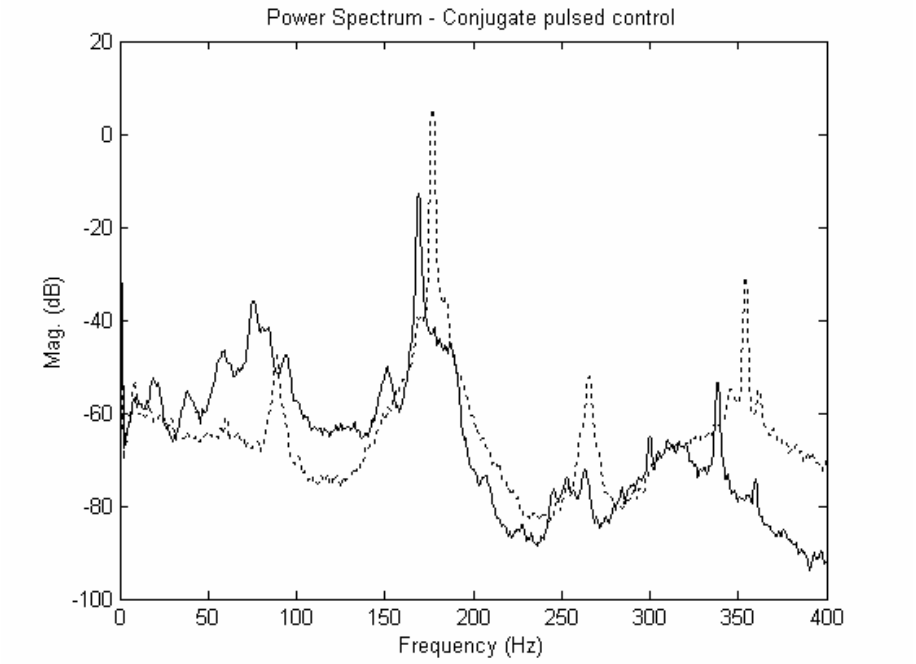

Figure 5.48 Power spectrum using Conjugate with pulsed actuation

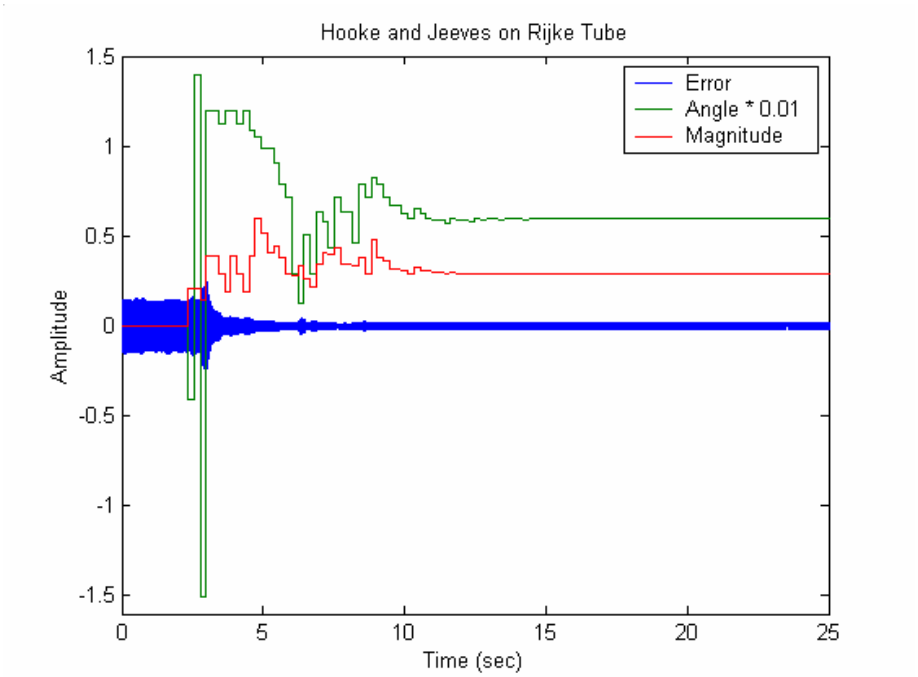

Figure 5.49 Phase (degrees) and linear magnitude of filter for Hooke and Jeeves algorithm with pulsed actuation

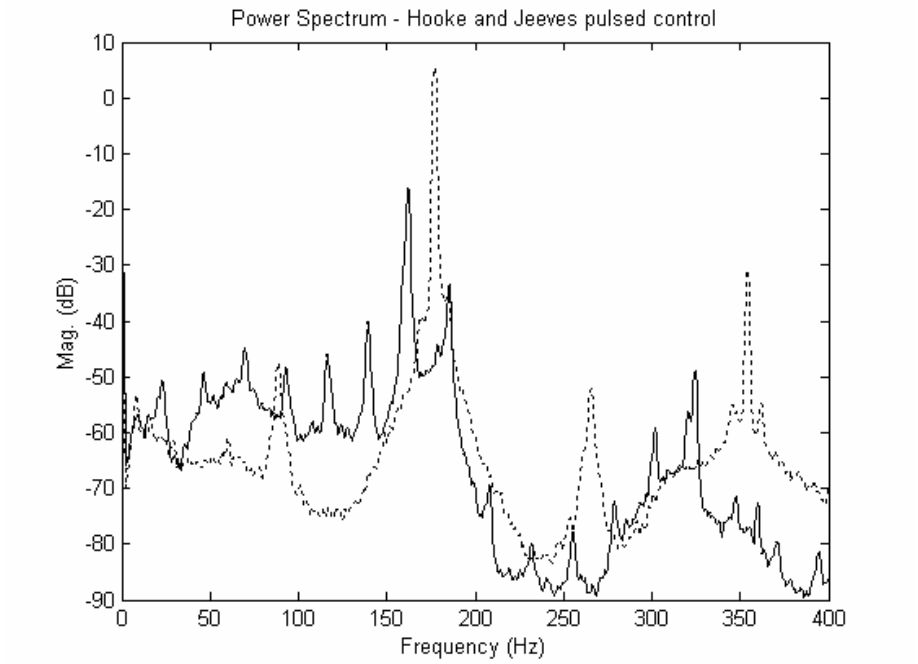

Figure 5.50 Power spectrum using Hooke and Jeeves with pulsed actuation

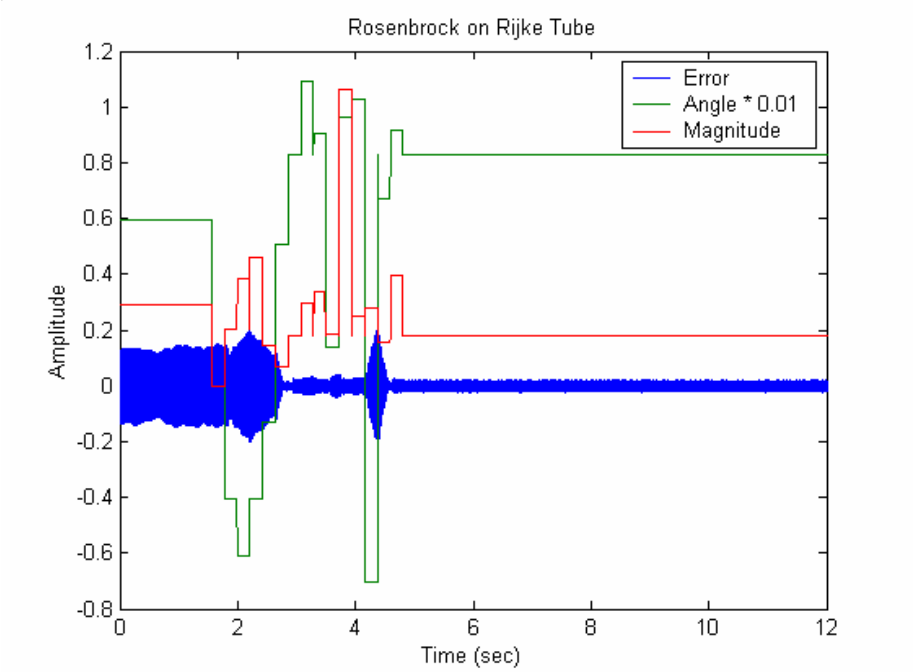

Figure 5.51 Phase (degrees) and linear magnitude of filter for Rosenbrock algorithm with pulsed actuation

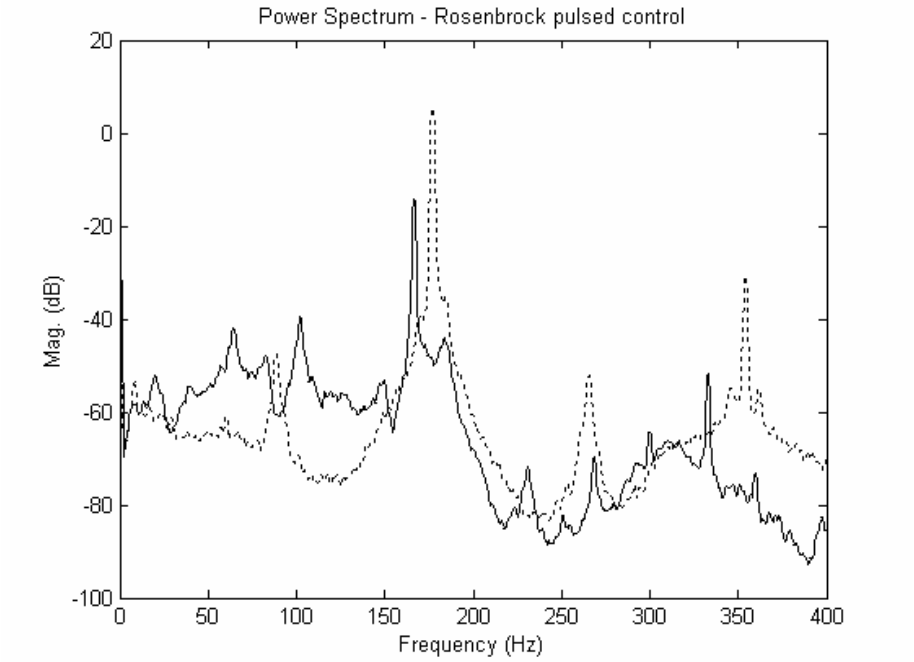

Figure 5.52 Power spectrum using Rosenbrock with pulsed actuation

The Gradient algorithm was used to gather data for actuation at increasing sub-harmonics. The results are shown in Figure 5.53 through Figure 5.56. Note that, because

a bandpass filter was also employed for these tests, the dominant energy component is not necessarily the initial instability frequency.

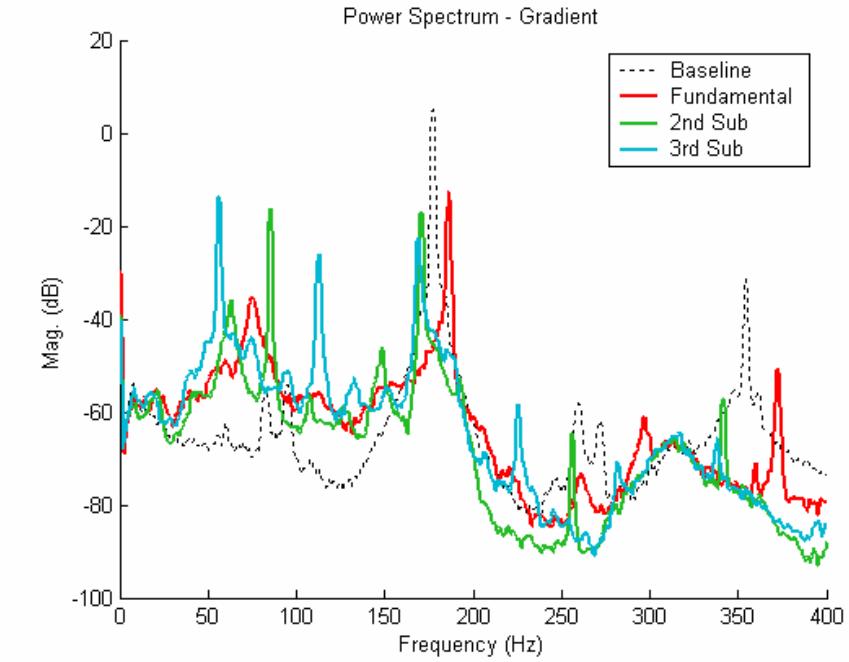

Figure 5.53 Power spectrum of Gradient algorithm using pulsed actuation

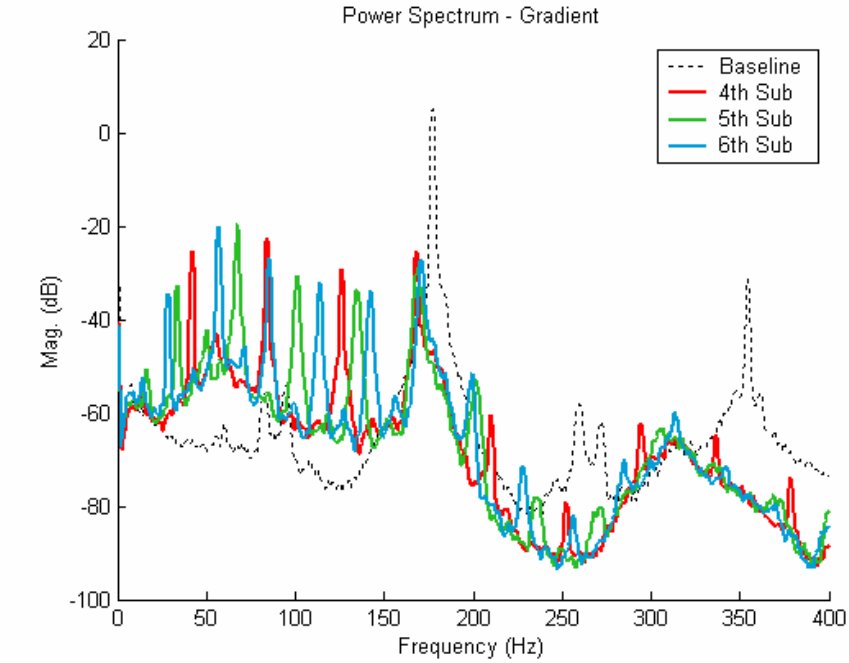

Figure 5.54 Power spectrum of Gradient algorithm using pulsed actuation

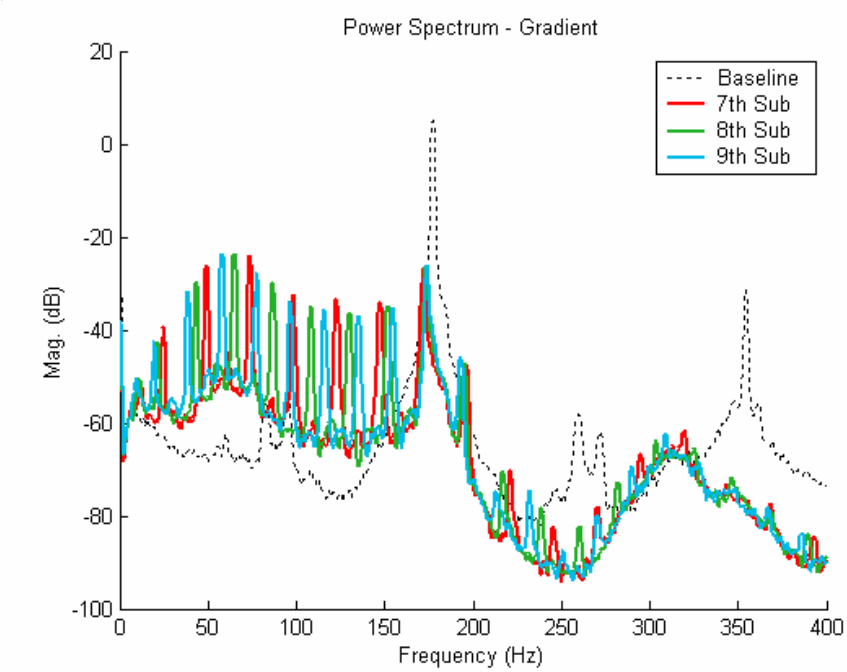

Figure 5.55 Power spectrum of Gradient algorithm using pulsed actuation

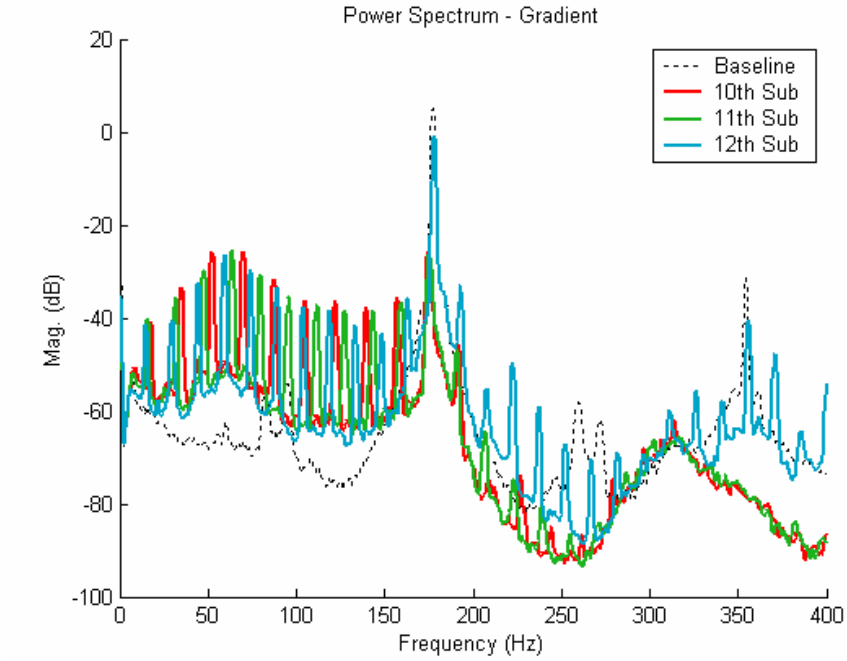

Figure 5.56 Power spectrum of Gradient algorithm using pulsed actuation

Note that at the 12th sub-harmonic control was lost. The reasoning for this phenomenon is discussed in the next section.

5.5 Pulsed Actuation Discussion

Each algorithm was able to achieve considerable attenuation of the combustor signal by pulsing at the fundamental frequency. In general, control was achieved quickly, which is a function of the pulsed control. With pulsed actuation, the gain of the signal is already relatively high. The algorithms must then only search the weight space for the optimal phase that results in control. As mentioned earlier, the signal did find a secondary stable limit cycle due to the pulsed control.

With proportional actuation, the noise floor for the controlled case decreased, but this was not the case for the pulsed actuation. This is demonstrated in Figure 5.57, which shows results from proportional and pulsed actuation for the Gradient algorithm.

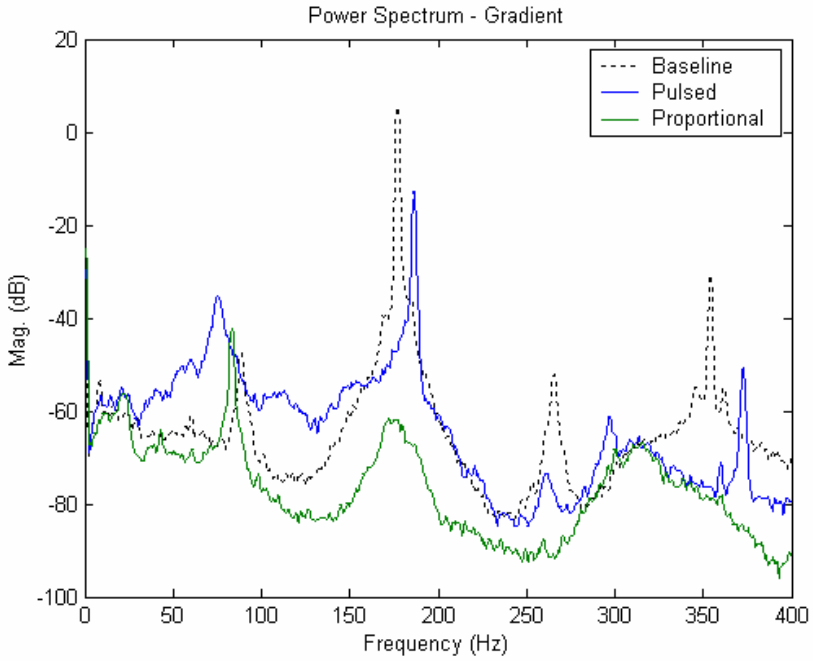

Figure 5.57 Pulsed and Proportional actuation using Gradient algorithm

Each algorithm was also able to obtain control directly using the 2nd sub-harmonic, although the convergence for this case was slower than actuating at the fundamental frequency. The resulting limit cycle was at a lower magnitude than previously observed for the fundamental frequency. This new limit cycle decreases in amplitude as higher sub-harmonics are employed, because the actuator is acting at a lower frequency and thus adds less energy.

There was mixed success in the attempt to control the instability by directly applying control at the 3rd sub-harmonic, because some of the algorithms were able to obtain acceptable attenuation, while others were not. It is difficult to generalize as to which type of minimization algorithm, gradient or pattern search, performed better in this test. Two of the three gradient descent algorithms, TAG and Gradient, were able to achieve control, and one of the two pattern searches, Rosenbrock, was successful. All

algorithms, however, could gain control actuating at the 3rd sub-harmonic if the system was first controlled at the fundamental or 2nd sub-harmonic. This was the case with higher sub-harmonics, as well, in which control could not be achieved, but it could be maintained. Plots for the 2nd and 3rd sub-harmonics for each algorithm can be seen in Appendix E.

As mentioned earlier, at frequencies near the 12th sub-harmonic, control was lost. Carson [5] has shown that the relevant signal is only that at the instability frequency. The power spectrum of the signal sent to the speaker is shown in Figure 5.58 (using Gradient algorithm). The instability frequency has shifted slightly under the influence of control, and is now between 180 and 190 Hz. It is clear from Figure 5.58 that as the sub-harmonic order increases, the energy of the control signal at the instability frequency decreases. Because the amplitude of the signal is limited to 1 volt, eventually there is not enough gain in the signal at this frequency to sufficiently control the tube.

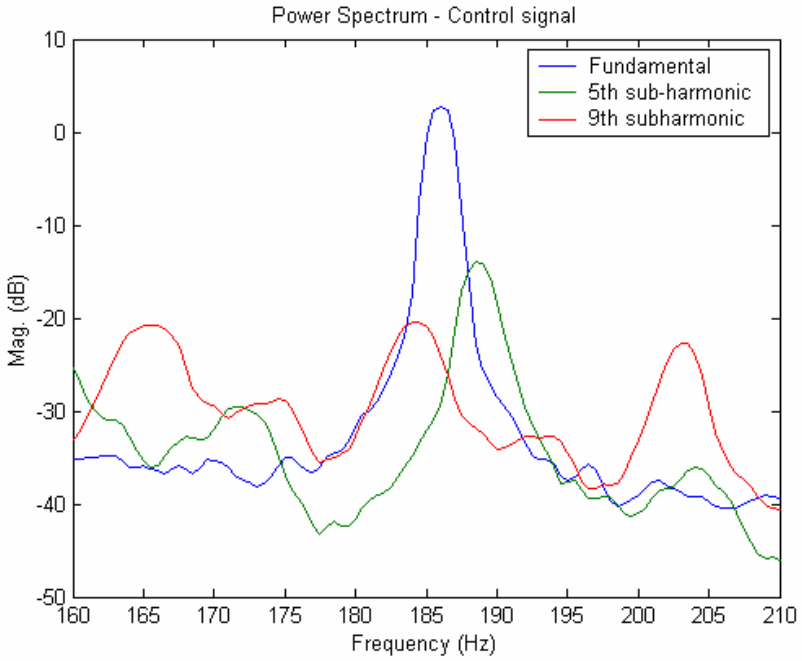

Figure 5.58 Power spectrum of control signal sent to actuator

5.6 Liquid Fuel Combustor

The second combustor that was used during this work was a turbulent swirl stabilized kerosene tube combustor. A picture of the experimental apparatus is shown in Figure 5.59. As with the Rijke tube, this combustor was a closed-open tube. A fuel nozzle is located at the bottom of the tube, and there exists an instability at approximately 105 Hz. The PSD of the unstable combustor is shown in Figure 5.60.

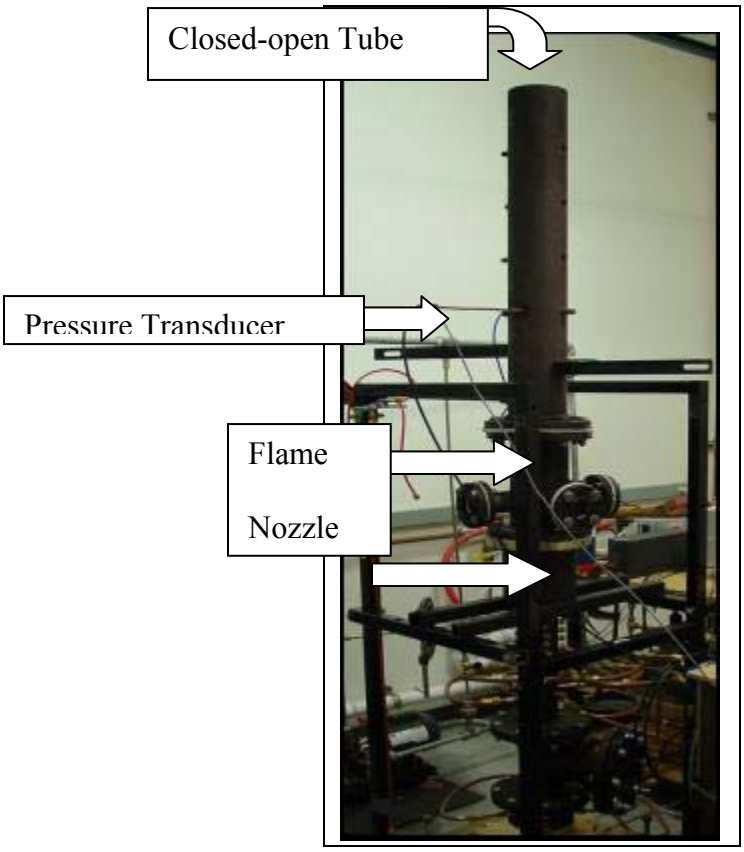

Figure 5.59 Liquid fuel combustor

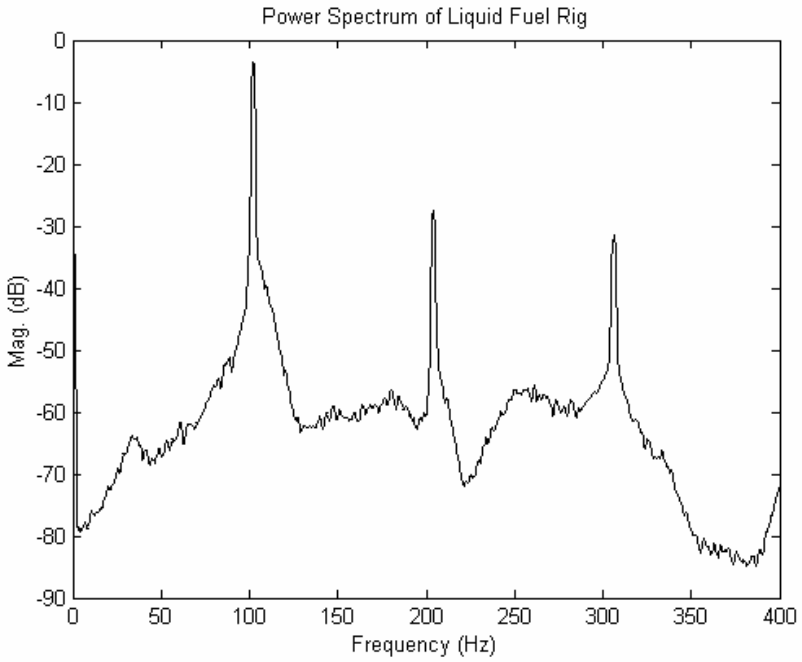

Figure 5.60 Power spectral density of the unstable liquid rig

Actuation for this combustor was accomplished by modulating the fuel, which thus modulates the heat release of the flame. This was done using a proportional throttling valve actuated by a piezoelectric stack. Operating at 105 Hz, the stack had a displacement of approximately 225 microns at no load and a maximum force at zero displacement of 8400 N (1888 lbs.). The valve can be seen in Figure 5.61, and the valve/stack system is shown in Figure 5.62. A more detailed description of the apparatus can be found in DeCastro [12]. The following tests were run at a nozzle pressure of 85 psi and airflow of approximately 22 SCFM.

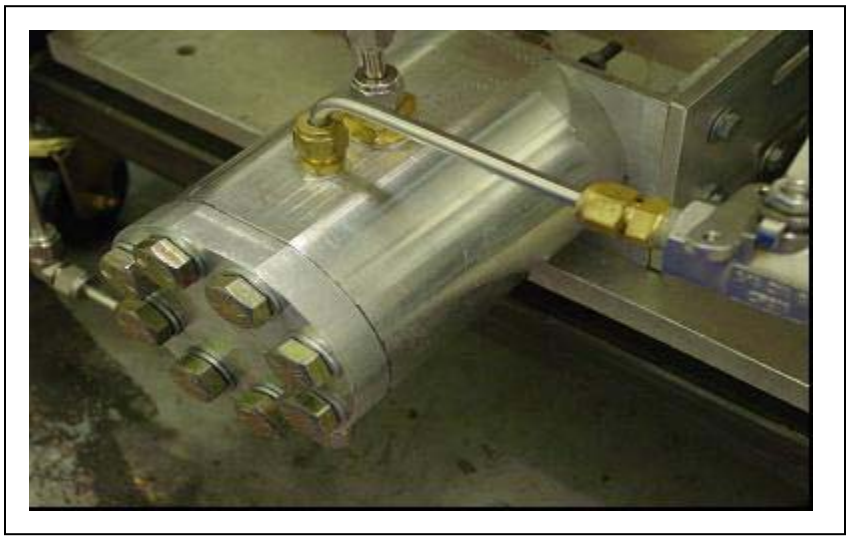

Figure 5.61 Proportional throttling valve used to modulate fuel

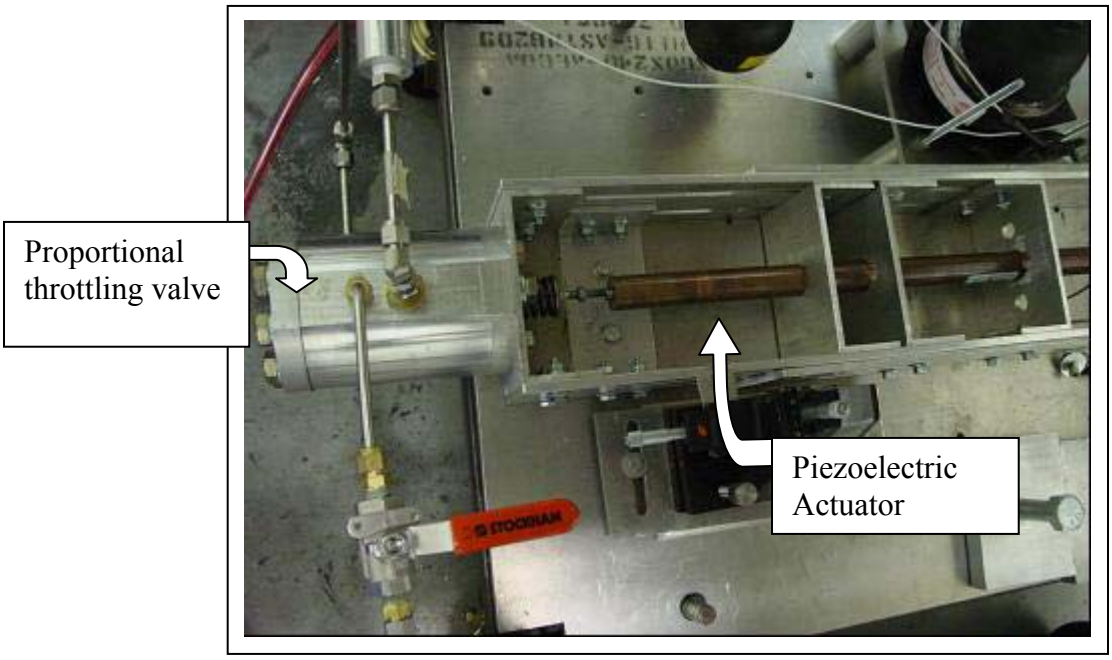

Figure 5.62 Valve and actuator assembly for fuel modulation

5.6.1 **Cost Surface**

A major part of the work that was done on this combustor was the determination of the cost surface, in terms of phase and magnitude of the phase shifter versus the resulting MSE of the combustor pressure. The result of this work is shown in Figure 5.63. This cost surface appears to be very favorable for the application of adaptive control because the surface is relatively smooth and parabolic. The current algorithms are ill suited to handle a cost surface that contains local minima. Fortunately, no local minima are apparent in Figure 5.63.

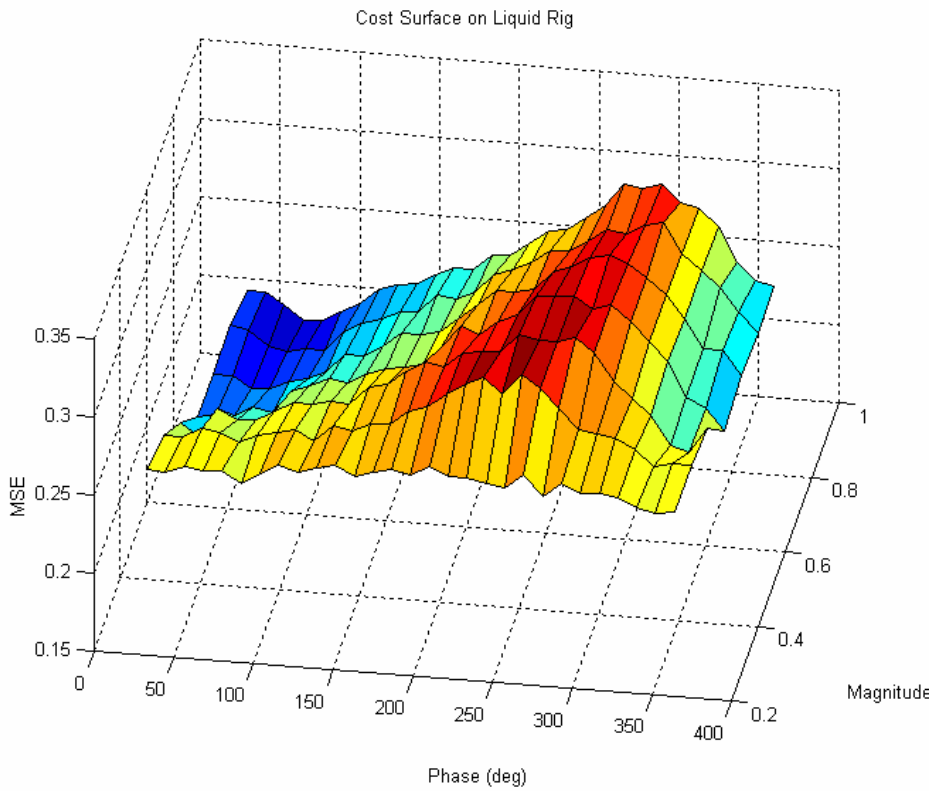

Figure 5.63 Cost surface for the liquid fuel combustor

5.6.2 Adaptive Algorithms on Liquid Fuel Rig

Adaptive control was tested on this combustor with limited success. The parameters that were calculated during the tuning phase for the tests with the adaptive algorithms are shown in Table 5-7. The sampling frequency that was used for these tests was 3200 Hz.

Table 5-7 Parameter values for the liquid rig

Convergence Parameter, μ	0.4607
Perturbation Size, δ	0.38
Integration Length, N	998 samples

Results for the Gradient algorithm and Hooke and Jeeves algorithm are shown in Figure 5.64 and Figure 5.65. Both of the algorithms achieved a small amount of attenuation of the combustor pressure signal, however they did not produce a filter with the optimal phase as seen from the cost surface. The adaptive algorithms quickly produced a phase of approximately 150° and proceeded to increase the magnitude. The cost surface suggests that the best attenuation will occur at a phase of approximately 70°.

As mentioned earlier, the cost surface for this system seems to be well suited for control via adaptive control. A possible reason for the failure of the algorithms to adapt to the optimal weights for this condition may be that the perturbation size was not large enough. Because of this, there was not a large enough phase variation and the algorithms continued to increase the magnitude but did not adjust the phase significantly.

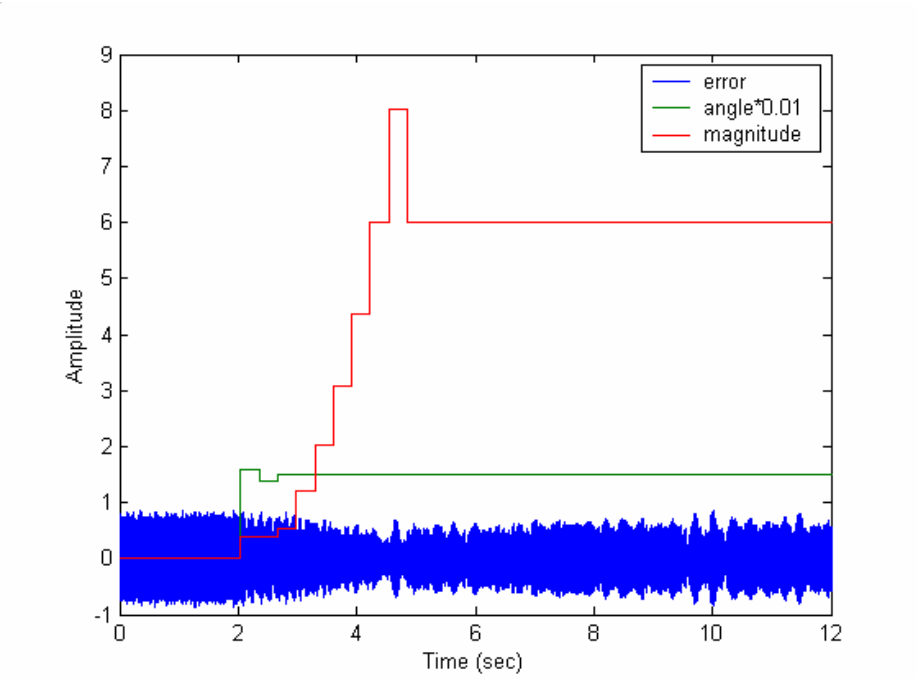

Figure 5.64 Phase (degrees) and linear magnitude of filter for Gradient algorithm on liquid rig

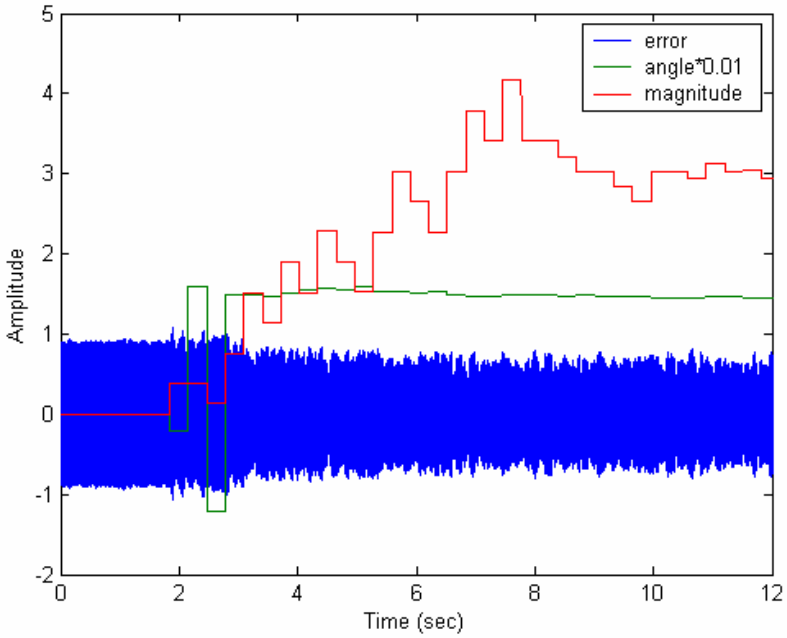

Figure 5.65 Phase (degrees) and linear magnitude of filter for Hooke and Jeeves algorithm on liquid rig

5.6.3 Simulations

Due to complications with the fuel modulation hardware, further tests on the liquid fuel combustor were not possible. However, the data from the cost surface was used to develop simulations in Matlab to determine if the algorithms would converge upon the minimum of the surface. The TAG algorithm was used for the simulations, because it was the simplest algorithm to adapt to Matlab.

During the simulations, the algorithm adapts the weights similar to the process described in Chapter 2. A table of the MSE values from the cost surface was used to determine the MSE that corresponds to the current weights. A linear interpolation function was used for values that were between data points.

Several simulations were run, with varying perturbation sizes and initial weight conditions. Figure 5.66 through Figure 5.68 show the simulations for perturbation sizes of 0.1, 0.4, and 0.8. There was an increase in the performance as the perturbation increased from 0.1 to 0.4, however the algorithm did not converge upon a condition that was within an acceptable distance from the optimal. Any further increase above 0.4 did not result in an increase in performance.

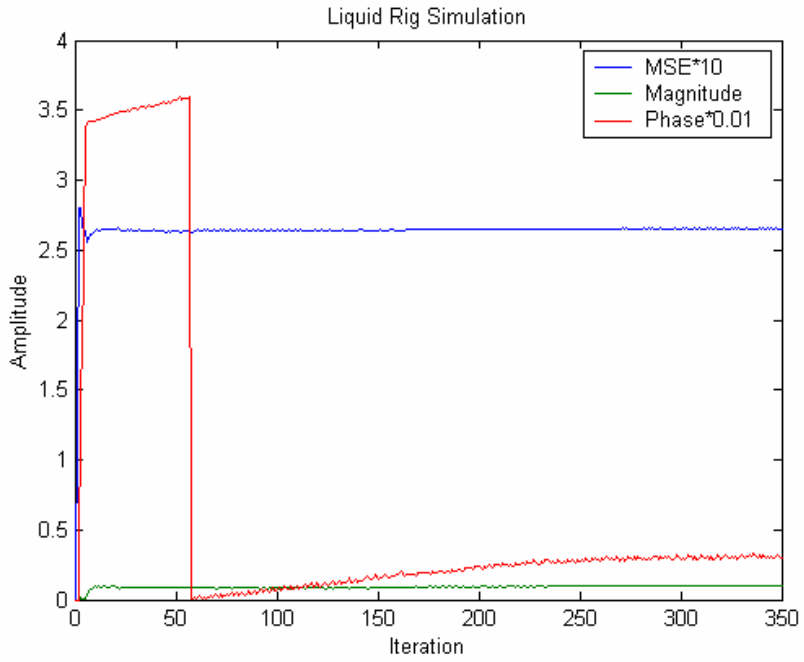

Figure 5.66 Liquid rig simulation for perturbation size = 0.1

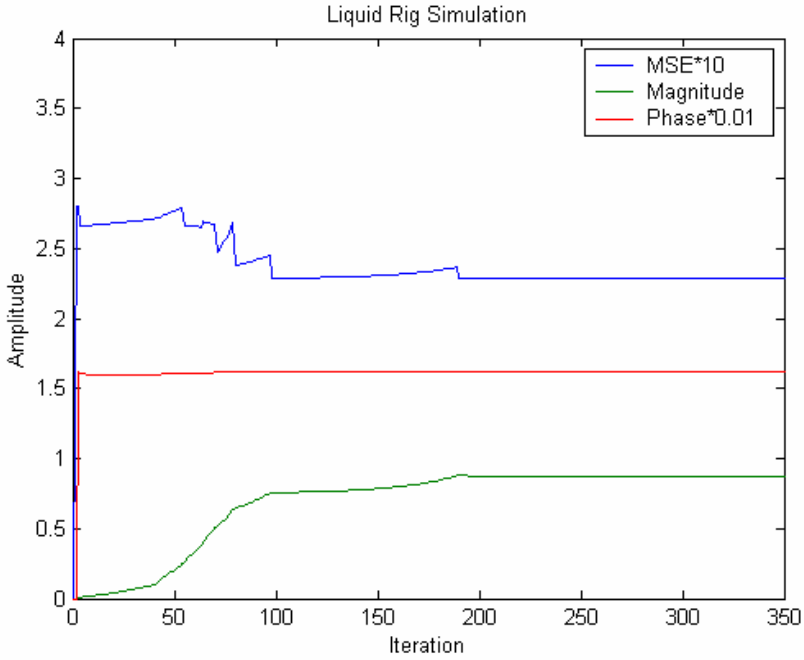

Figure 5.67 Liquid rig simulation for perturbation size = 0.4

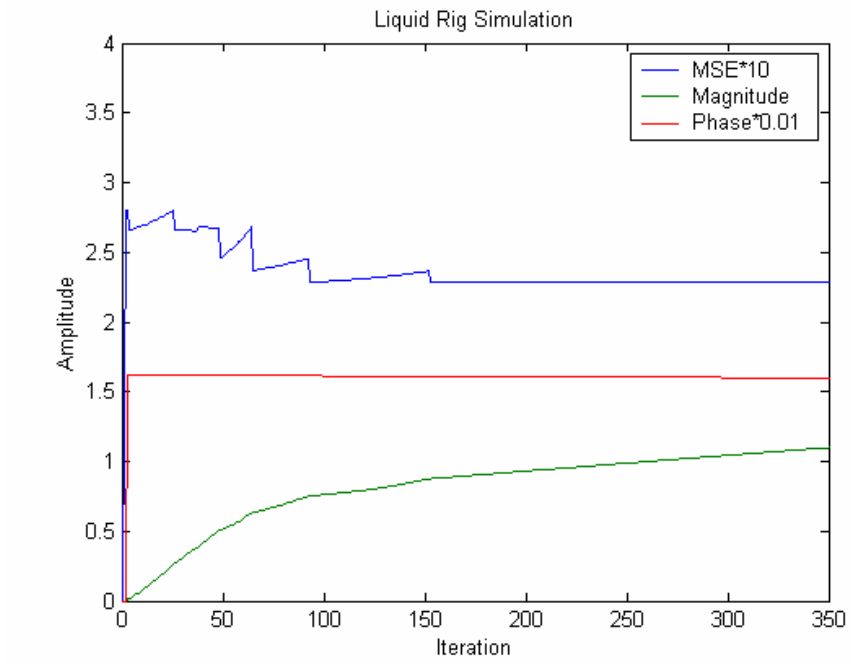

Figure 5.68 Liquid rig simulation for perturbation size = 0.8

It is possible that the algorithm was stuck in a local minimum; therefore a probing function was added to the algorithm. The algorithm proceeds as before; however, if the MSE has not changed for a specified amount of time, the probing function is activated. This function chooses random weight values and calculates the corresponding MSE value. If the new weights increase performance, the algorithm continues the algorithm from that point. If the performance is not enhanced, the probe returns to the original weights.

The addition of this probing function resulted in an increase in performance, as the algorithm converged to a filter with MSE very close to the optimal MSE. A plot of the MSE, magnitude, and phase trajectories is shown in Figure 5.69. A summary of the results from the simulation is detailed in Table 5-8.

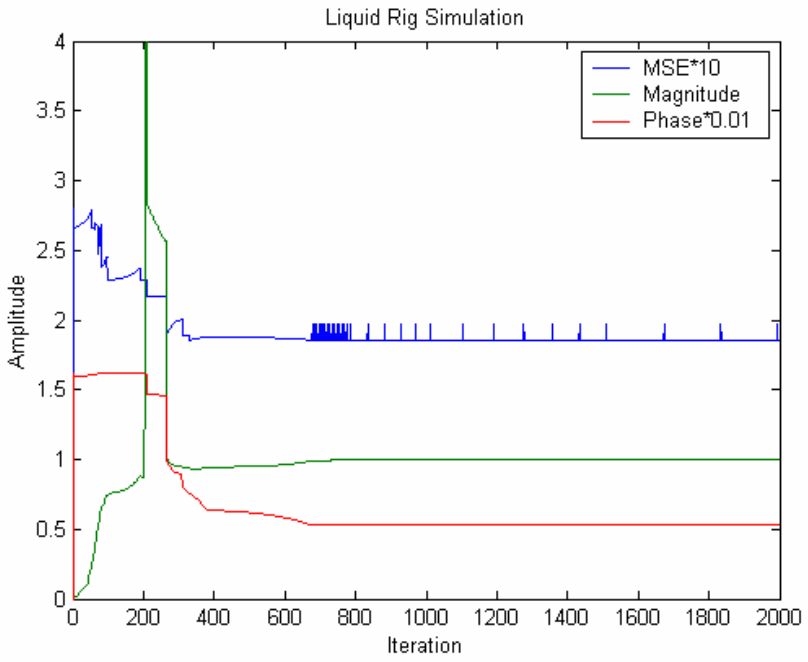

Figure 5.69 Liquid rig simulation for perturbation size = 0.4 with the probing function implemented

Table 5-8 Summary of simulation results

Perturbation Size	MSE	Phase	Magnitude
0.1	0.2655	30°	0.1
0.4	0.2283	161°	0.875
0.8	0.2281	160°	0.876
1.2	0.2282	161°	0.95
0.4 (With Probe)	0.1856	53°	1.0

The simulations have shown that an increase in the perturbation size could result in an increase in performance. This is not an absolute solution, however. The addition of a probing function may be required to prevent the algorithms from becoming stuck in a local minimum.

The implementation of the probing function on the liquid fuel combustor will present some challenges. Acceptable areas of the weight space must be chosen for the probing function to reference. Probing in a poor area of the weight space may have several ill effects. If the system is being stabilized by the current weights, probing may result in losing control. Also, a very poor combination of weights may affect the flame with respect to emissions or cause the flame to blowout. Finally, a drastic change in the control output may harm the fuel modulation system. Thus, care must be taken when implementing this function.

Chapter 6 Conclusions and Future Work

6.1 Summary and Conclusions

In this work, several adaptive algorithms were implemented for use in active combustion control. These algorithms were of two basic structures: gradient descent and pattern search.

Initially, an electronic simulator was used during coding, diagnostics, and validation of the algorithms. It was an analog electronic model of the self-excited loop formed from the acoustics and flame dynamics of the Rijke tube. The acoustics were modeled as second order, and the flame dynamics were modeled as a first order low-pass filter. Each algorithm was successful in attenuating the simulated pressure oscillations. It was concluded that the gradient descent algorithms were superior to the pattern search algorithms with respect to the converge rate. This is due to the fact that nothing prevents the pattern search algorithms from taking search steps in non-optimal directions; whereas, the gradient descent algorithms exhibited a faster and smoother convergence. This trend was again seen in the later experiments.

The adaptive algorithms were then tested on the Rijke tube combustor. Three separate operating conditions were explored. For two lower equivalence ratio cases, all of the algorithms were able to control the instability present. Again, the gradient descent algorithms exhibited a faster convergence. At the highest equivalence ratio that was tested, a bursting behavior was exhibited. It was concluded that this was due to changes in the thermoacoustic plant and resulting limitations in the authority of the acoustic actuator, [1].

Tests were also performed on the Rijke tube using pulsed actuation. It was shown that the algorithms were also successful with this type of actuation. The convergence times for the algorithms were shown to be lower than for proportional control because, due to the fixed amplitude actuation, the algorithms did not have to search for a stabilizing magnitude for the filter. Subharmonic control was also tested. It was shown that the algorithms could achieve control using second and third subharmonic actuation, and could maintain control up to the twelfth subharmonic. At each higher subharmonic, the magnitude of the control signal at the fundamental frequency decreased. Because of the fixed amplitude of the control signal, eventually the signal at the fundamental signal was not large enough to keep control.

A second combustor was also used for this work. It was a liquid kerosene fueled, swirl-stabilized tube combustor. A cost function was generated for this rig, which showed the MSE of the combustor pressure signal versus the phase and magnitude of the control filter. Tests were also run on some of the adaptive algorithms, which did not

converge upon the optimal solution as seen from the cost function data. Simulations were performed in Matlab using the TAG algorithm. The results of the simulations were consistent with the experimental data. A probing function was implemented which searched the weight space if the algorithm has stalled in a local minimum. The implementation of this function increased the convergence performance significantly.

6.2 Proposed Future Work

The current software implementation is used in conjunction with an analog bandpass filter. This limits the usefulness and versatility of the program. It would be very beneficial to incorporate a digital bandpass filter into the code. This would create a more self-contained and complete tool, and eliminate the need to transport additional equipment for testing or implementation.

Another feature that would be a useful addition to the existing code is a subroutine that automatically determines the frequency of the instability. There are features of the code, such as the magnitude and phase of the filter, which depend on the instability frequency. Currently, this information is entered manually. An automatic determination of the frequency would be very convenient.

A probing function should also be included to improve convergence of the algorithms for combustor systems that contain local minima. Currently the algorithms are susceptible to convergence upon local minima, but a probing function would begin to probe the weight space in search for a lower MSE after the algorithms have been stalled for a certain amount of time.

Due to time and hardware limitations, a complete analysis of adaptive control of the liquid fuel rig could not be accomplished. It appears from the simulations discussed in Section 5.6 that the algorithms should be able to converge upon the minimum of the system. This, however, was not the result of testing done for this work. A detailed investigation needs to undertaken to determine the reason for this unexpected outcome.

The ultimate goal of this work is an automatic adaptive controller that can be used on a variety of combustors with little interaction required from an operator. This work has made a great deal of progress towards the realization of that goal, however future work is still required to fully satisfy all of the desired features of the controller.

References

[1] M. A. Vaudrey. "Active Control Methods for Non-linear Self-excited Systems," PhD Dissertation, Virginia Tech, 2001.

[2] M. S. Bazaraa, C. M. Shetty, *Nonlinear Programming: Theory and Algorithms*, John Wiley and Sons, Inc., New York, NY, 1979.

[3] B. Widrow, S. D. Stearns, *Adaptive Signal Processing,* Prentice Hall, Inc., Englewood Cliffs, NJ, 1985.

[4] D. M. Himmelblau, *Applied Nonlinear Programming,* McGraw-Hill, Inc., New York, NY, 1972.

[5] J. M. Carson, "Subharmonic and Non-subharmonic Pulsed Control of Thermoacoustic Instabilities: Analysis and Experiment," Master's Thesis, Virginia Tech, 2001.

[6] K. McManus, T.Poinsott, S.M. Candel, "A Review of Active Control of Combustion Instabilities," Prog. Energy Combust. Sci. 19, 1993, pp. 1-29.

[7] R.L. Raun, M.W. Beckstead, J.C. Finlinson, K.P. Brooks, "A Review of Rijke Tubes, Rijke Burners and Related Devices," Prog. Energy Combust. Sci. 19, 1993, pp. 313 – 364.

[8] M. Krstic, A. Krupadanam, C. Jacobson, "Adaptive Stabilization of Nonlinear Acoustic Oscillations in Combustion Chambers," Proceedings of the 36th Conference on Decision and Control, 1997, pp. 3640-3645.

[9] Anuradha M. Annaswamy, et al. "Thermoacoustic Instability: Model-Based Optimal Control Designs and Experimental Validation," IEEE Transactions on Control Systems Technology, Vol. 8, No. 6, Nov. 2000 pp. 905-918.

[10] A. Kemal, C. Bowman, "Real-time Adaptive Feedback Control of Combustion Instability," Twenty-sixth Symposium International on Combustion, 1996, pp. 2803-2809.

[11] C. Jacobson, A. Banaszuk, Y. Zhang, "Active Control of Combustion Instabilities in Gas Turbine Engines for Low Emissions. Part II: Adaptive Control Algorithm Development, Demonstration and Performance Limitations."

[12] J. A. DeCastro, "Design and Validation of Fuel Injector Systems for Control of Combustion Instabilities," Master's Thesis, Virginia Tech, 2003.

Appendix A Simulation Results

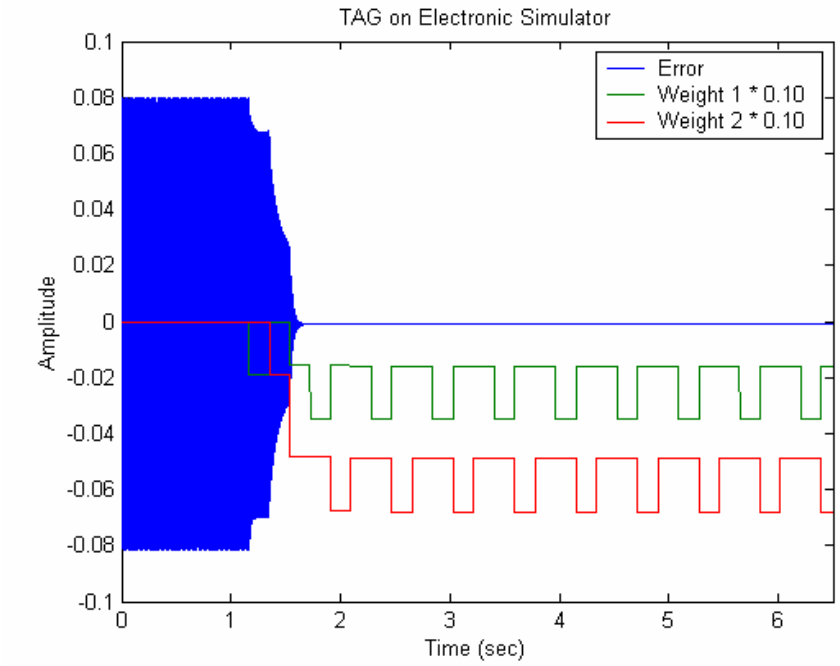

Figure A.1 Response envelope of simulator and filter weights for TAG algorithm

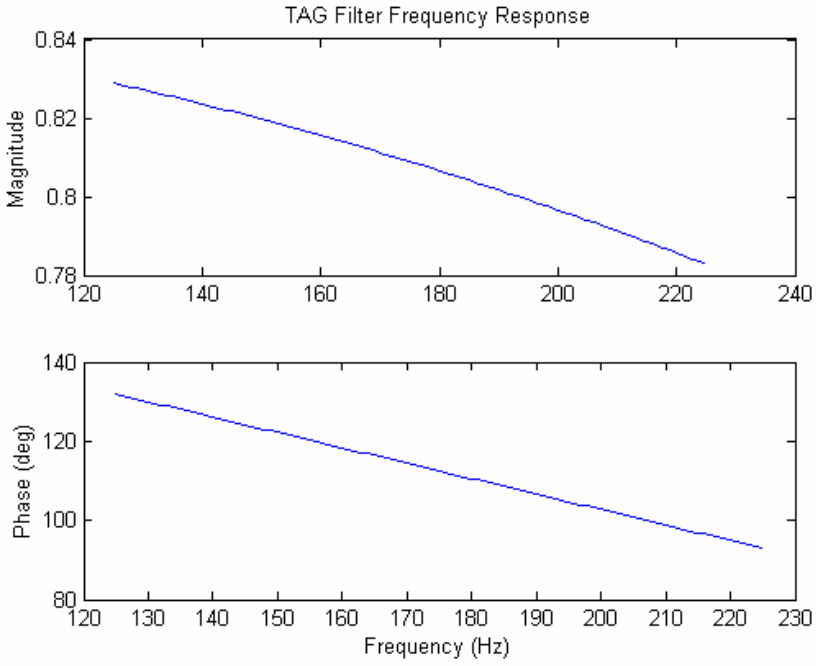

Figure A.2 Frequency response of steady-state TAG filter

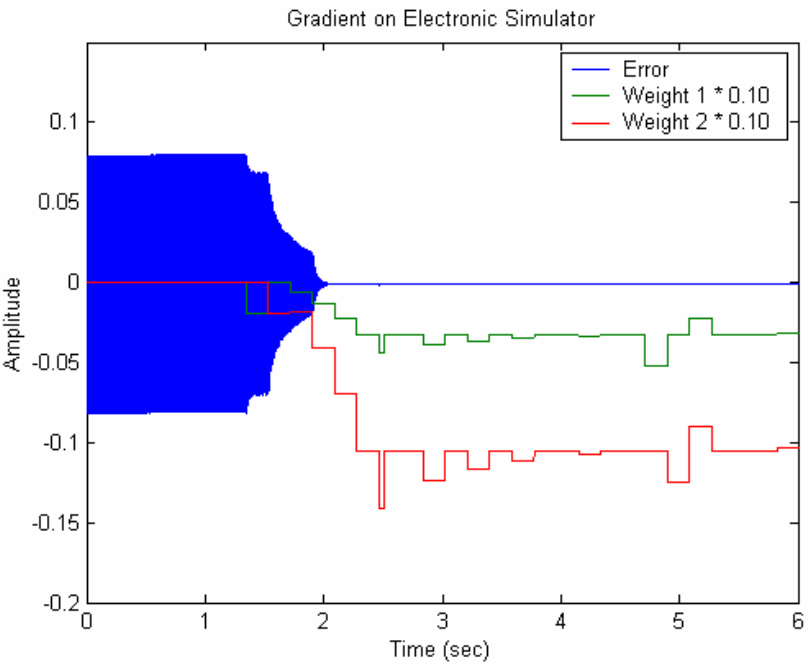

Figure A.3 Response envelope of simulator and filter weights for Gradient algorithm

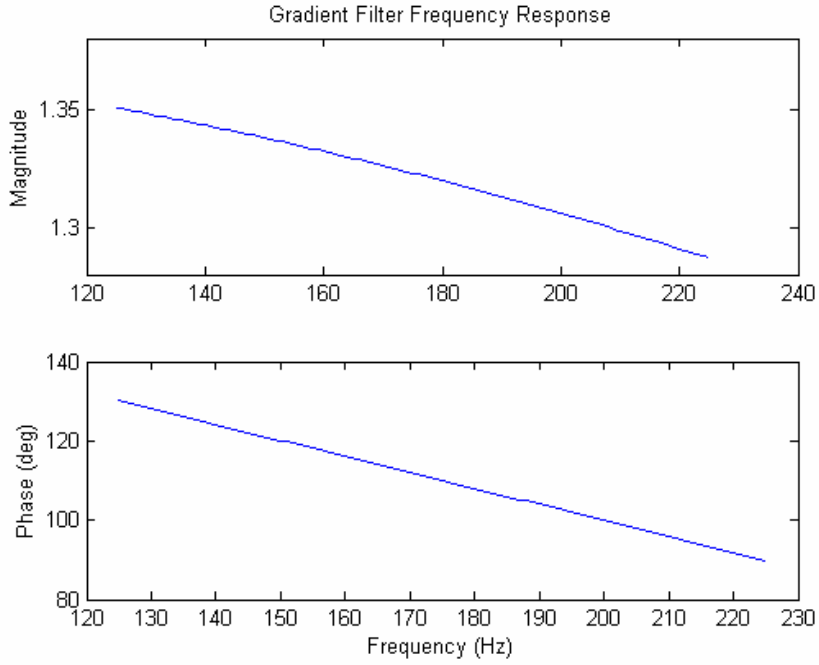

Figure A.4 Frequency response of steady-state Gradient filter

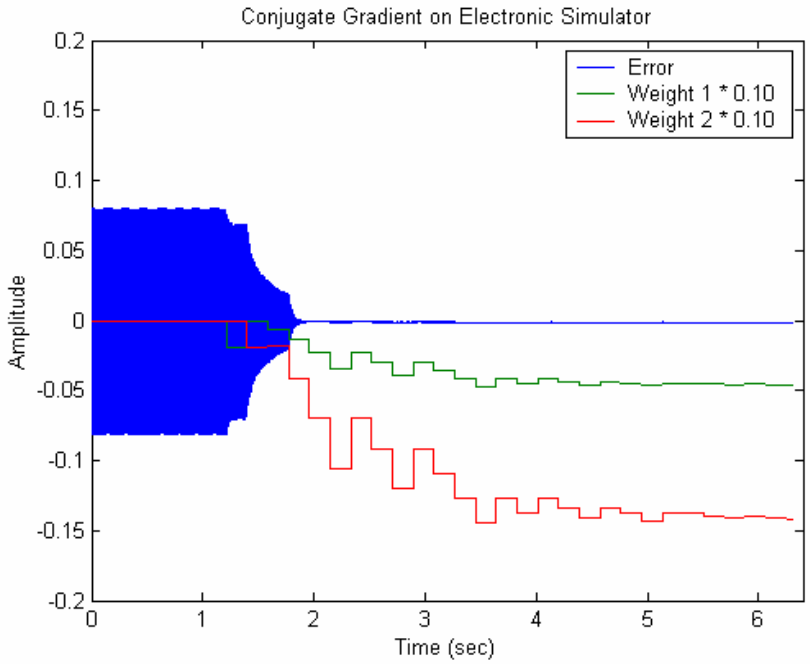

Figure A.5 Response envelope of simulator and filter weights for Conjugate algorithm

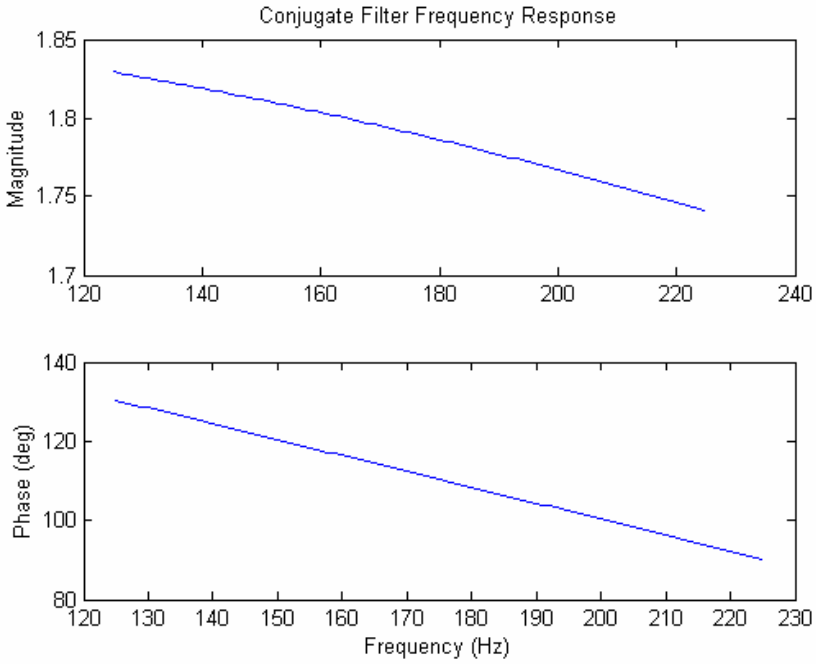

Figure A.6 Frequency response of steady-state Conjugate filter

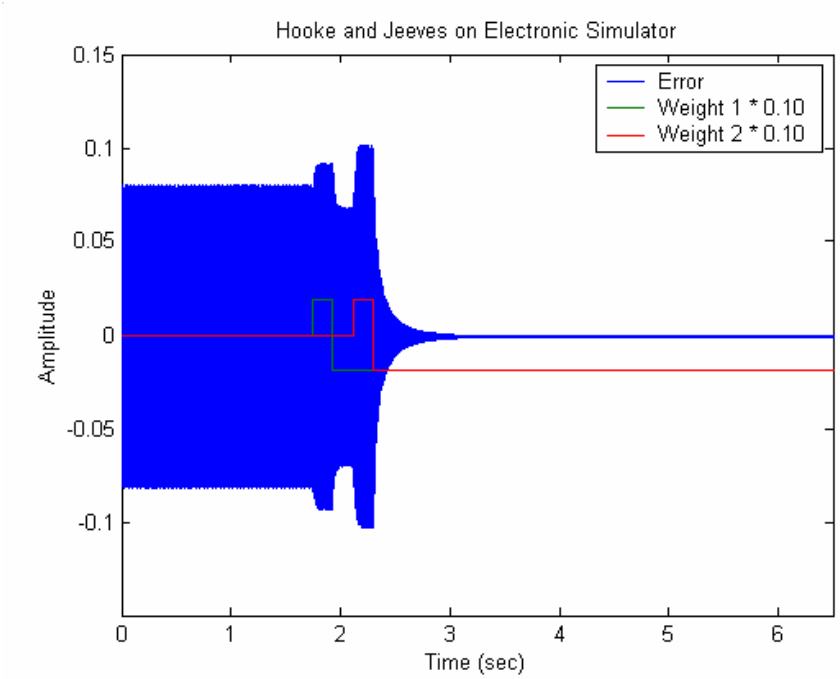

Figure A.7 Response envelope of simulator and filter weights for Hooke and Jeeves algorithm

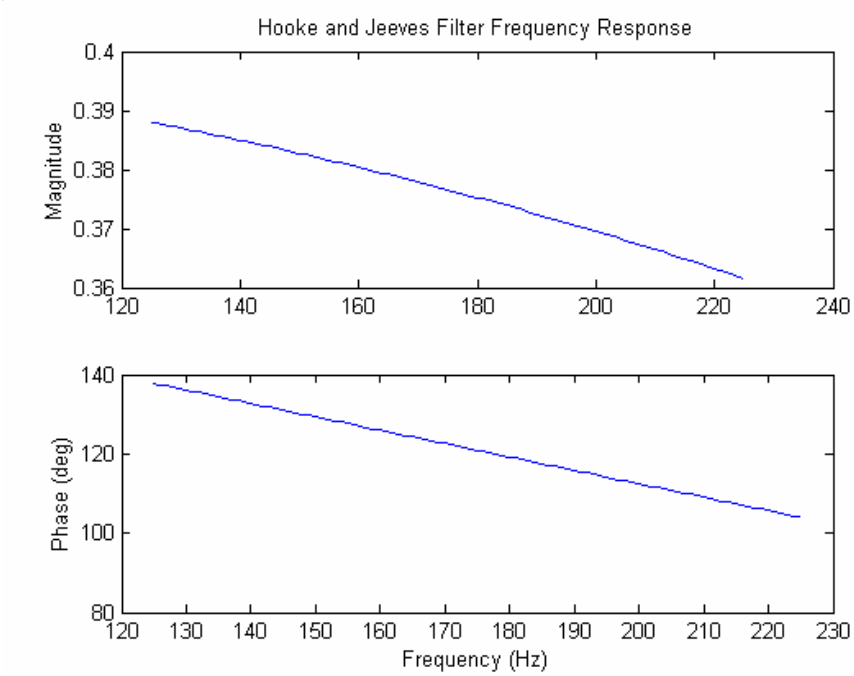

Figure A.8 Frequency response of steady-state Hooke and Jeeves filter

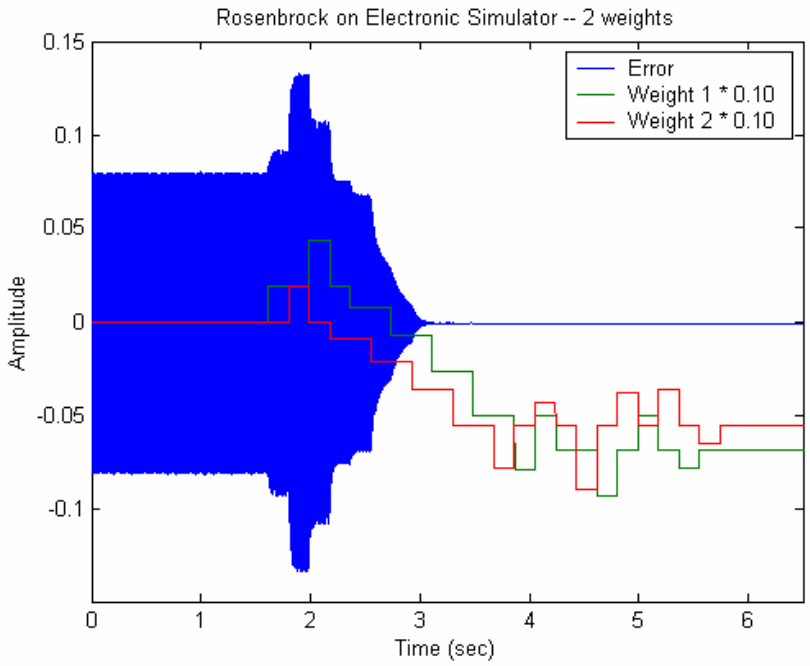

Figure A.9 Response envelope of simulator and filter weights for Rosenbrock algorithm

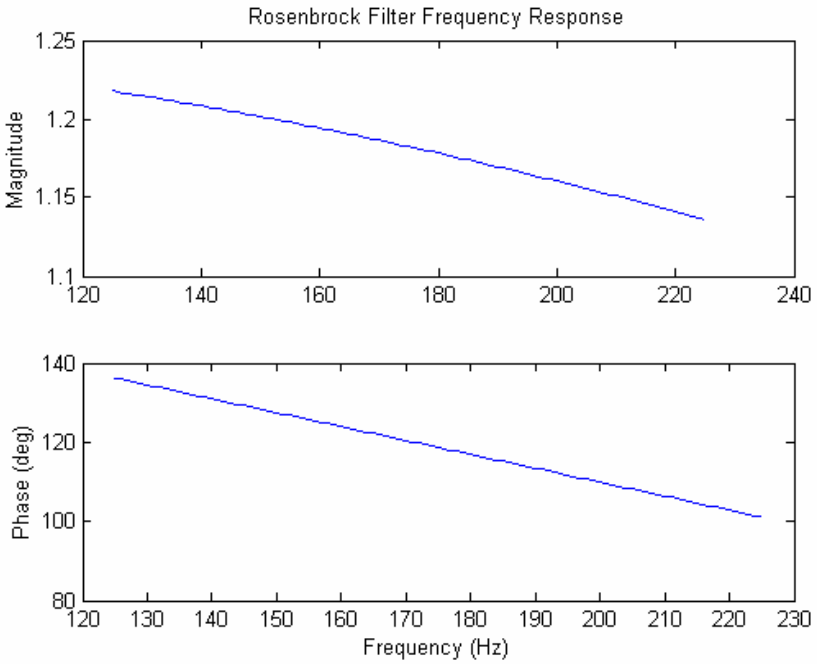

Figure A.10 Frequency response of steady-state Rosenbrock filter

Appendix B Rijke Tube Low Φ Results

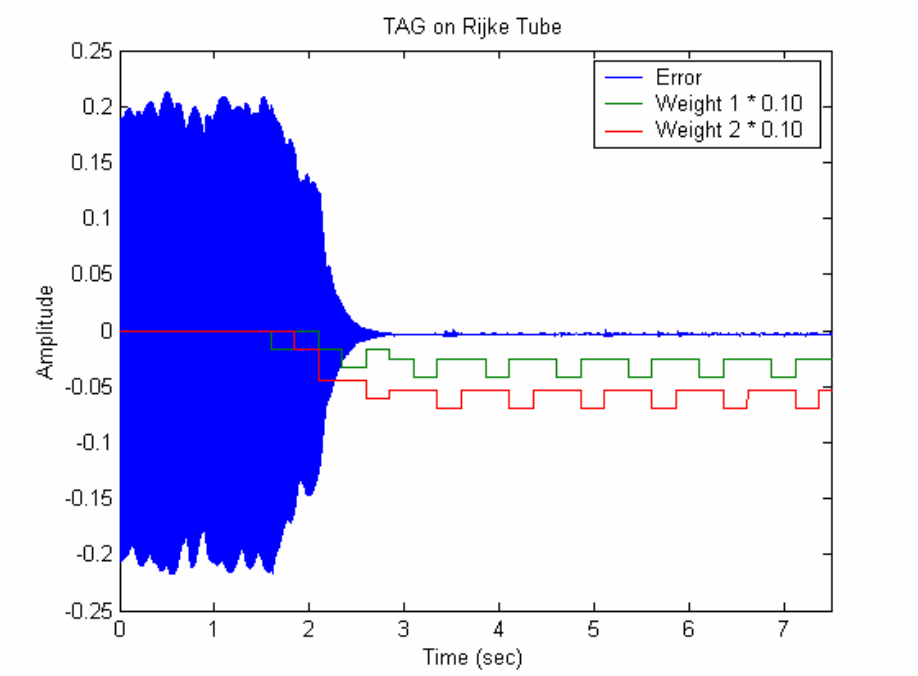

Figure B.1 Response envelope of Rijke Tube and filter weights for TAG algorithm

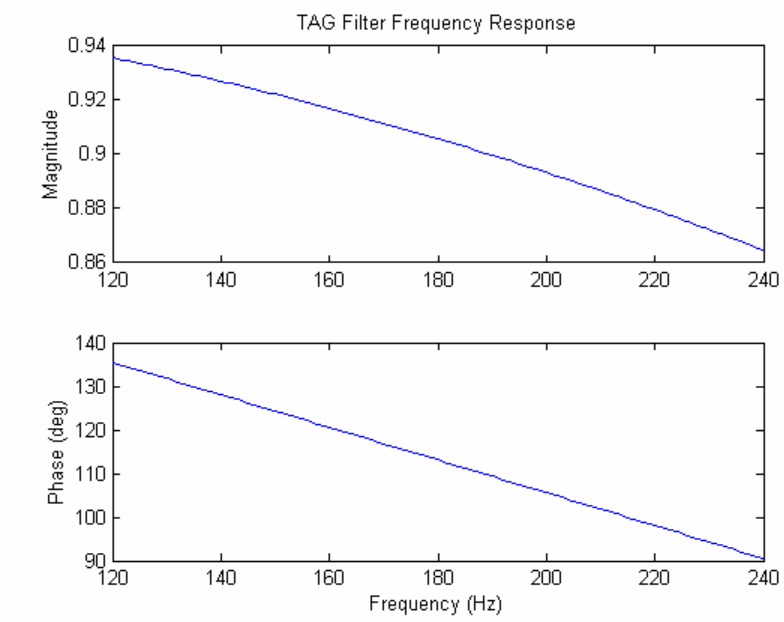

Figure B.2 Frequency response of steady-state TAG filter

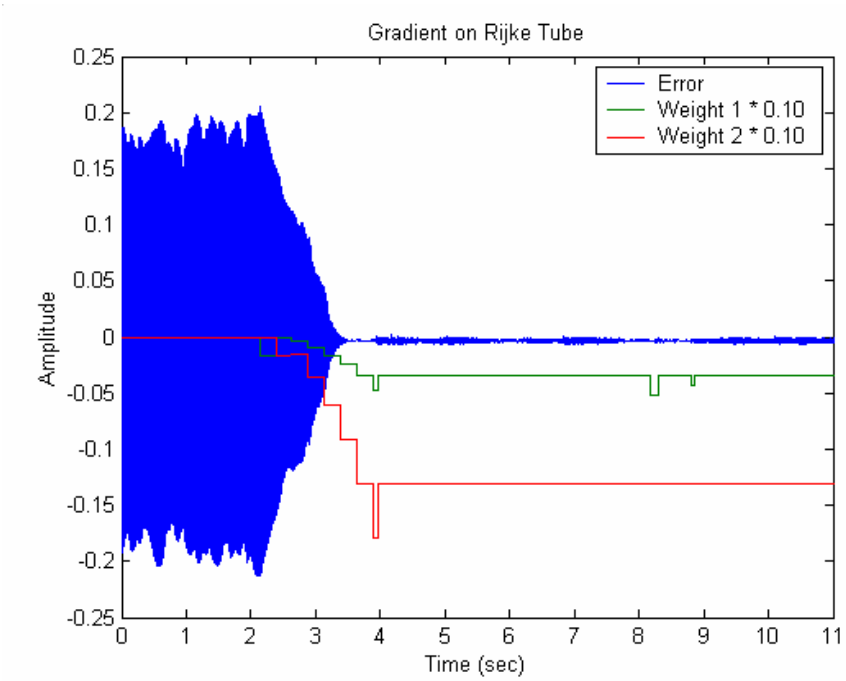

Figure B.3 Response envelope of Rijke Tube and filter weights for Gradient algorithm

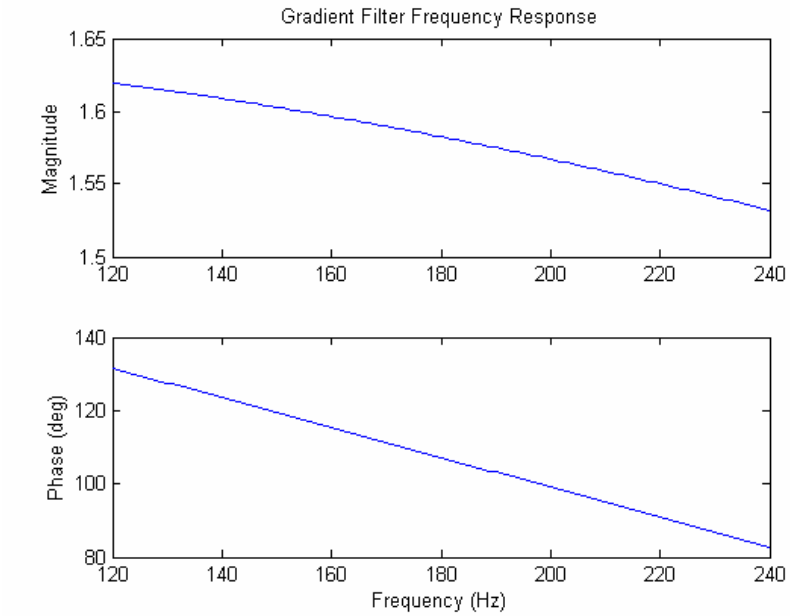

Figure B.4 Frequency response of steady-state Gradient filter

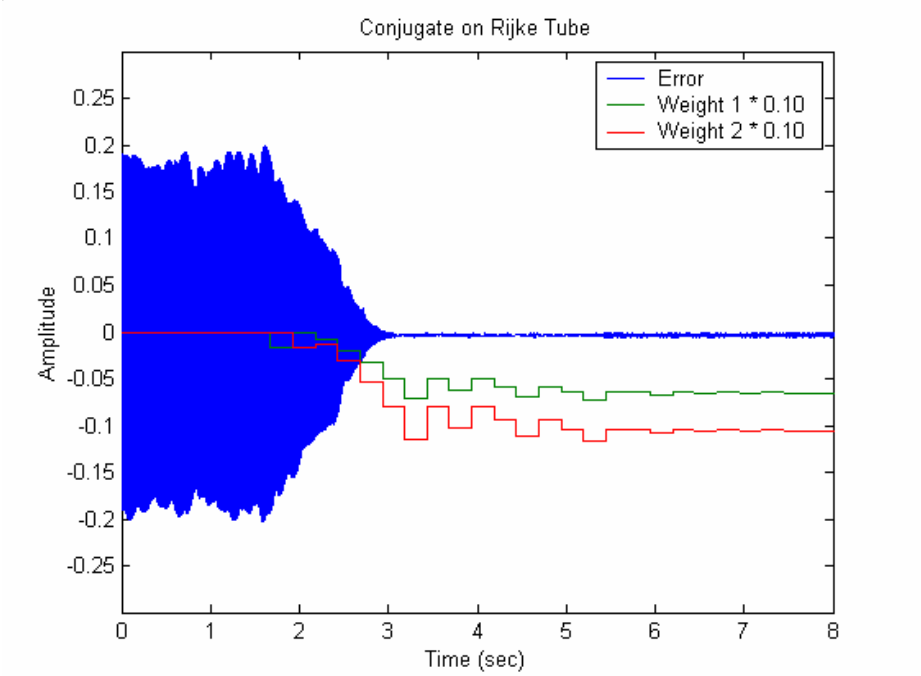

Figure B.5 Response envelope of Rijke Tube and filter weights for Conjugate algorithm

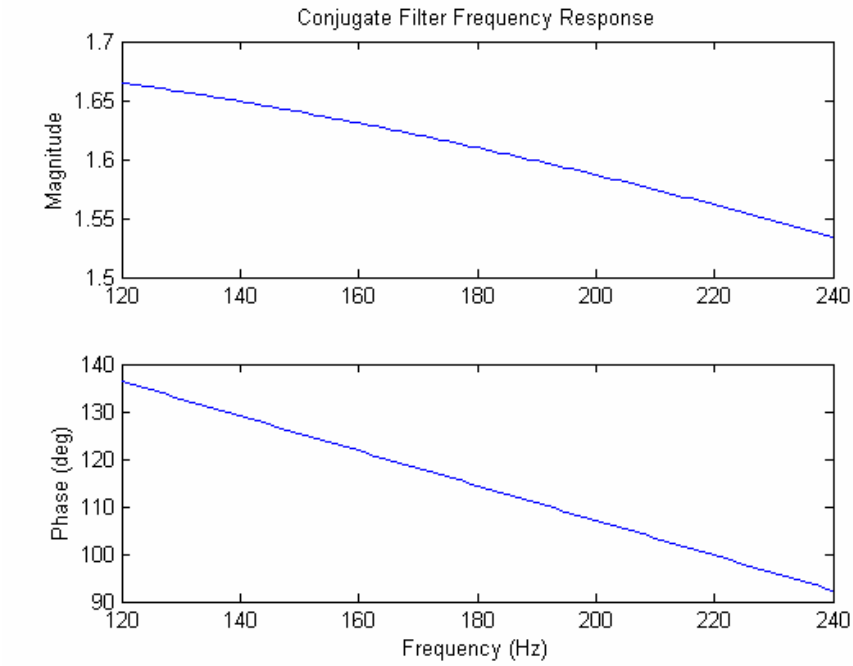

Figure B.6 Frequency response of steady-state Conjugate filter

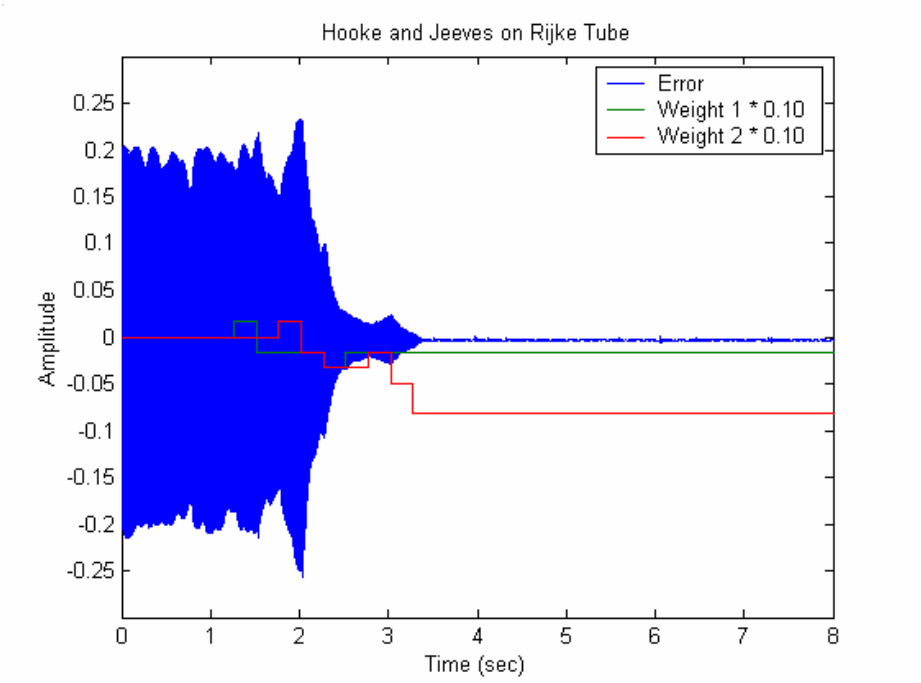

Figure B.7 Response envelope of Rijke Tube and filter weights for Hooke and Jeeves algorithm

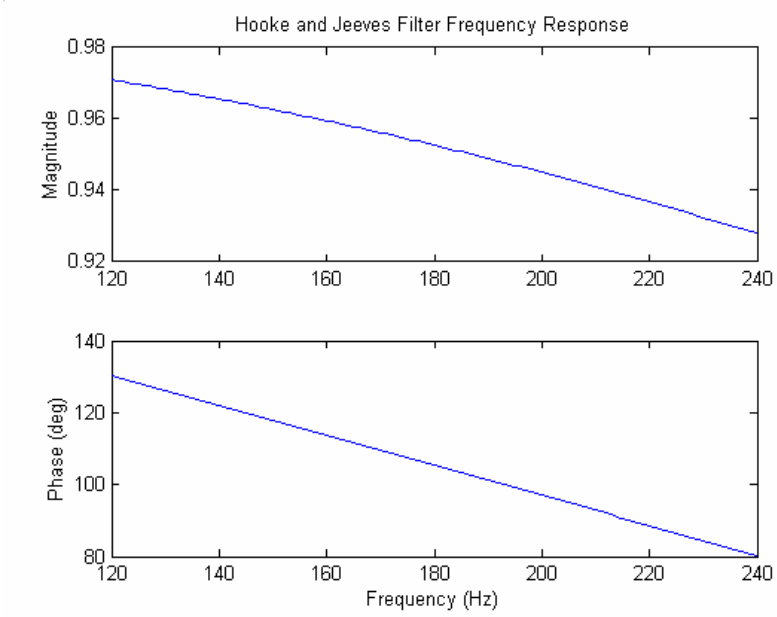

Figure B.8 Frequency response of steady-state Hooke and Jeeves filter

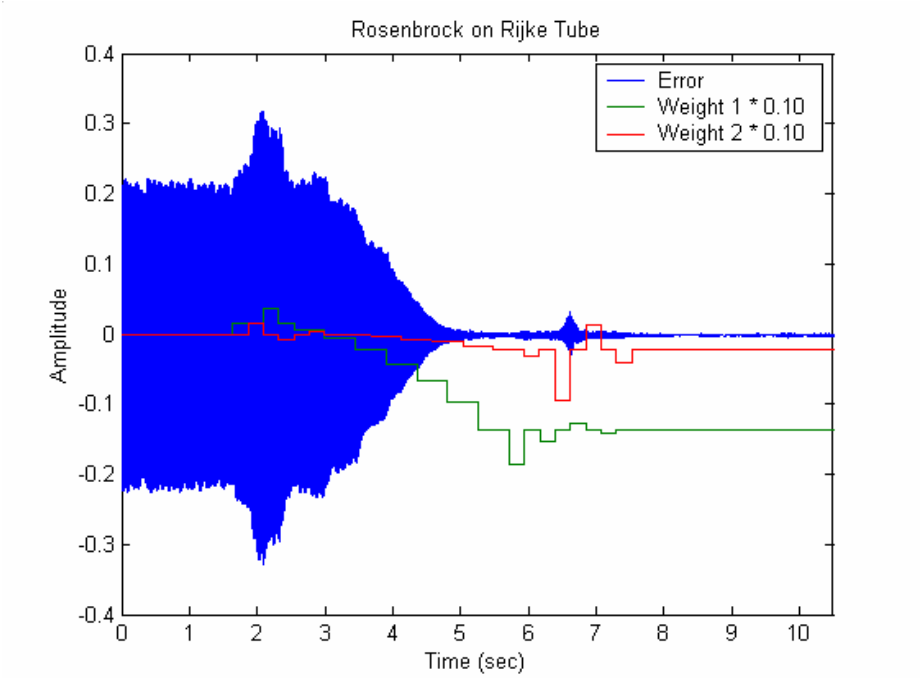

Figure B.9 Response envelope of Rijke Tube and filter weights for Rosenbrock algorithm

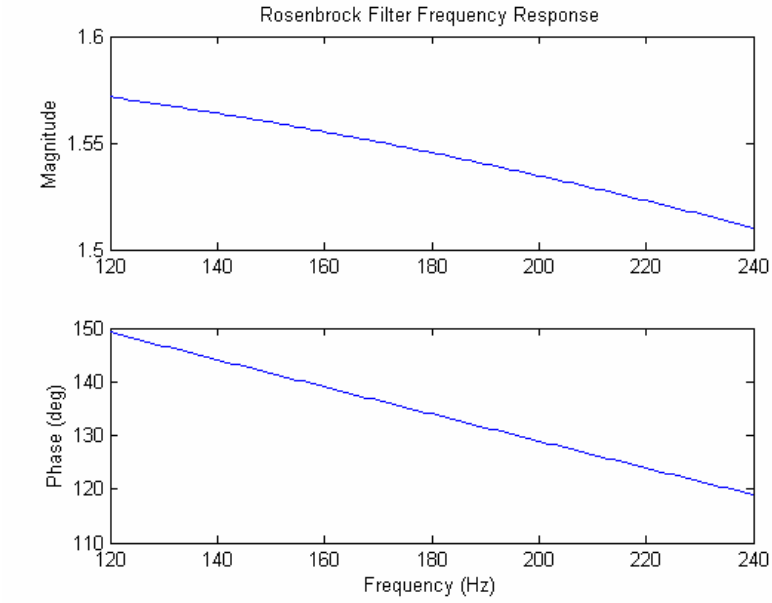

Figure B.10 Frequency response of steady-state Rosenbrock filter

Appendix C Rijke Tube Medium Φ Results

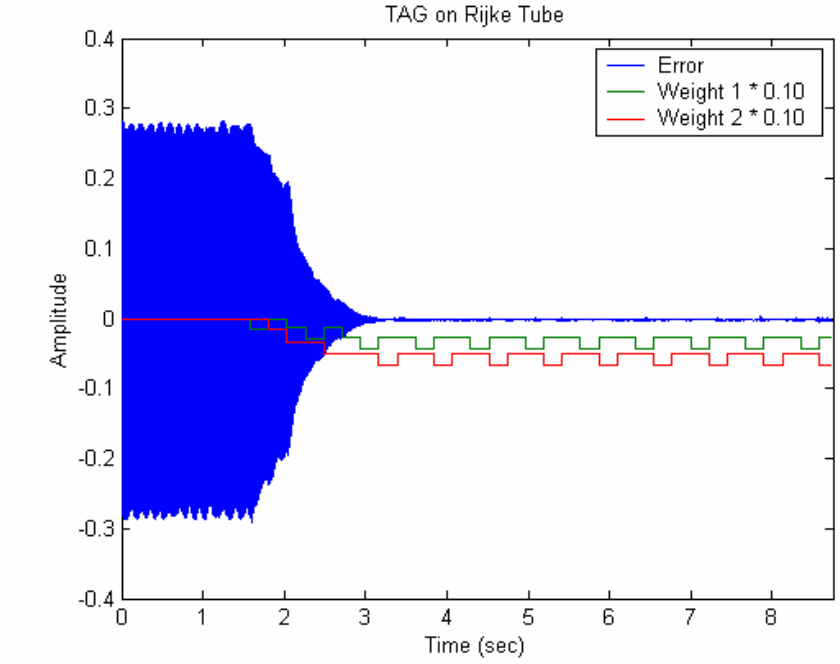

Figure C.C.1 Response envelope of Rijke Tube and filter weights for TAG algorithm

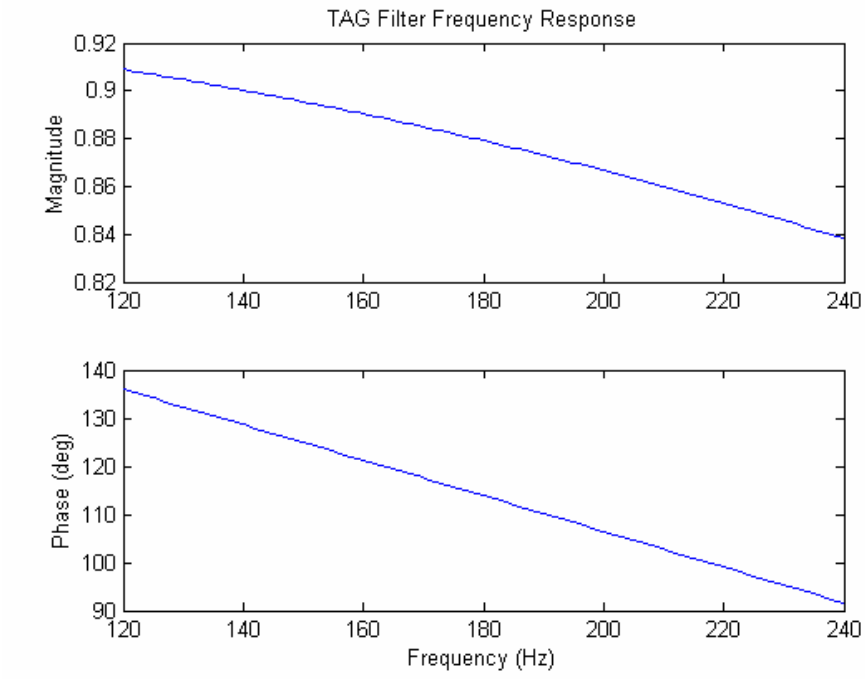

Figure C.2 Frequency response of steady-state TAG filter

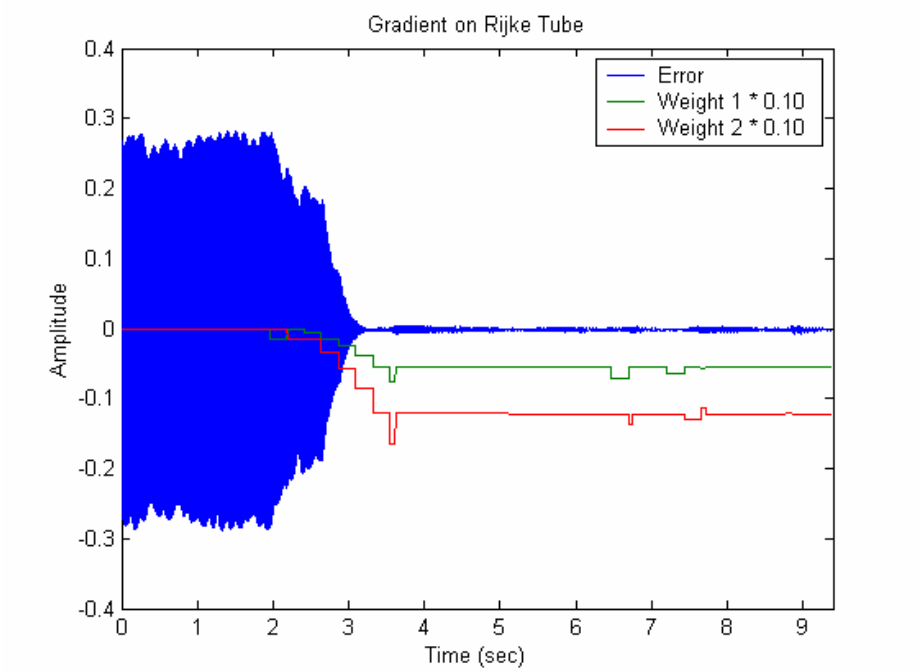

Figure C.3 Response envelope of Rijke Tube and filter weights for Gradient algorithm

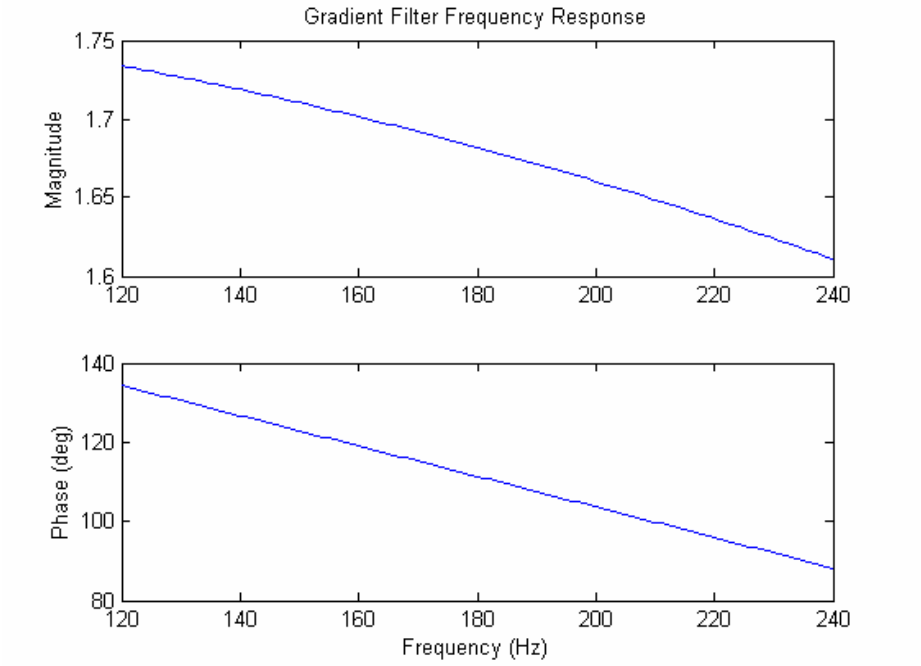

Figure C.4 Frequency response of steady-state Gradient filter

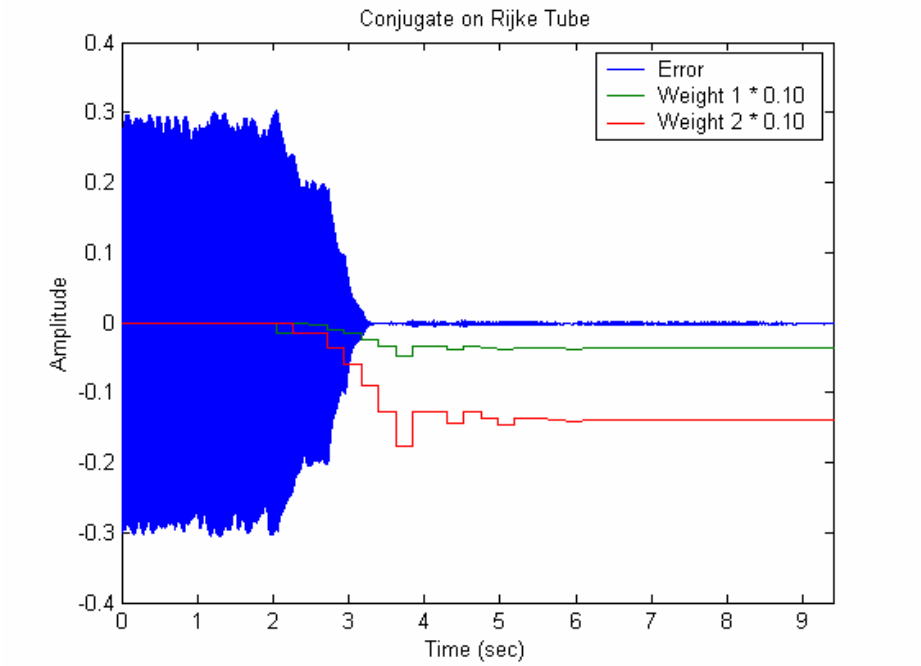

Figure C.5 Response envelope of Rijke Tube and filter weights for Conjugate algorithm

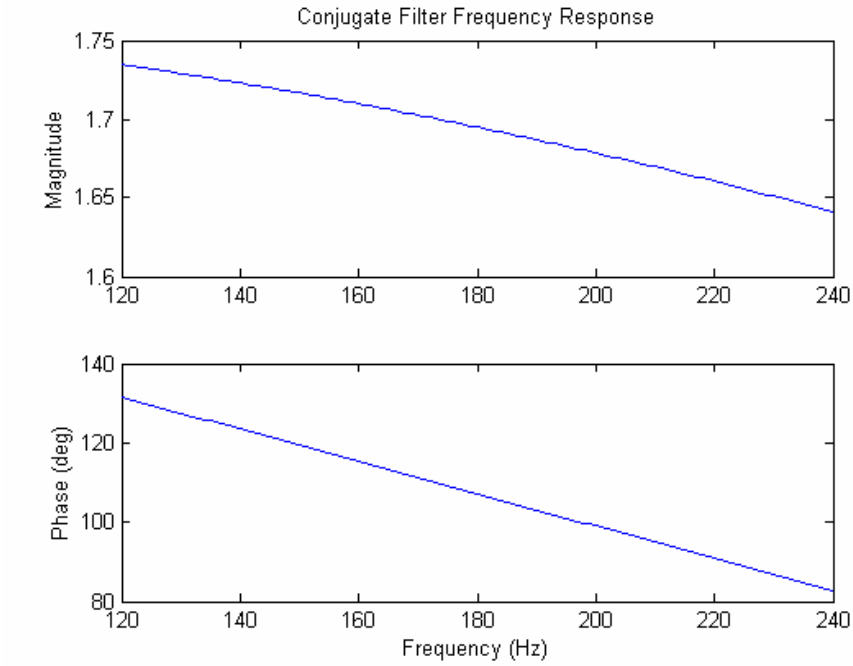

Figure C.6 Frequency response of steady-state Conjugate filter

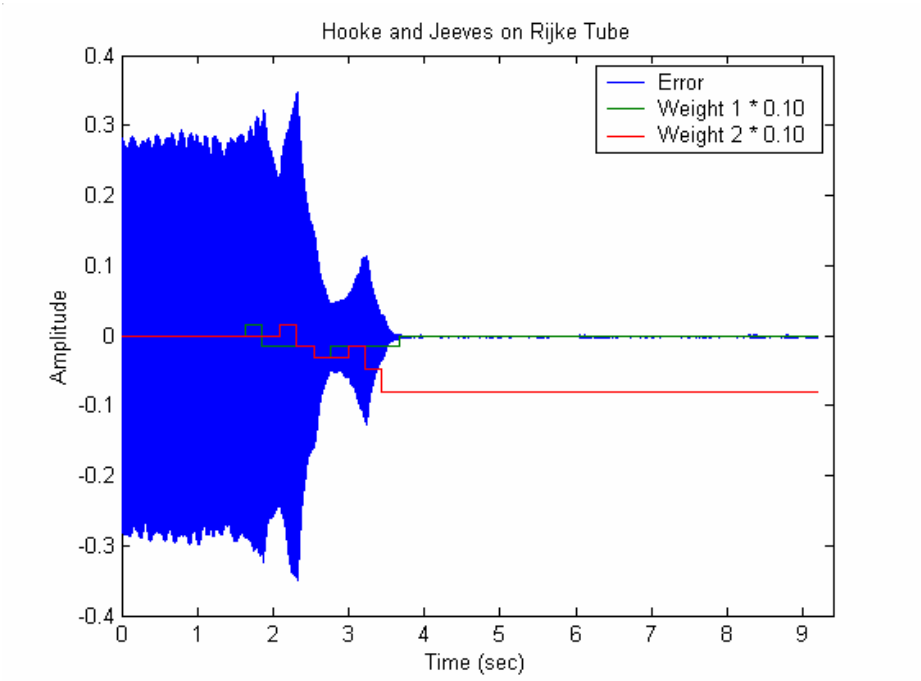

Figure C.7 Response envelope of Rijke Tube and filter weights for Hooke and Jeeves algorithm

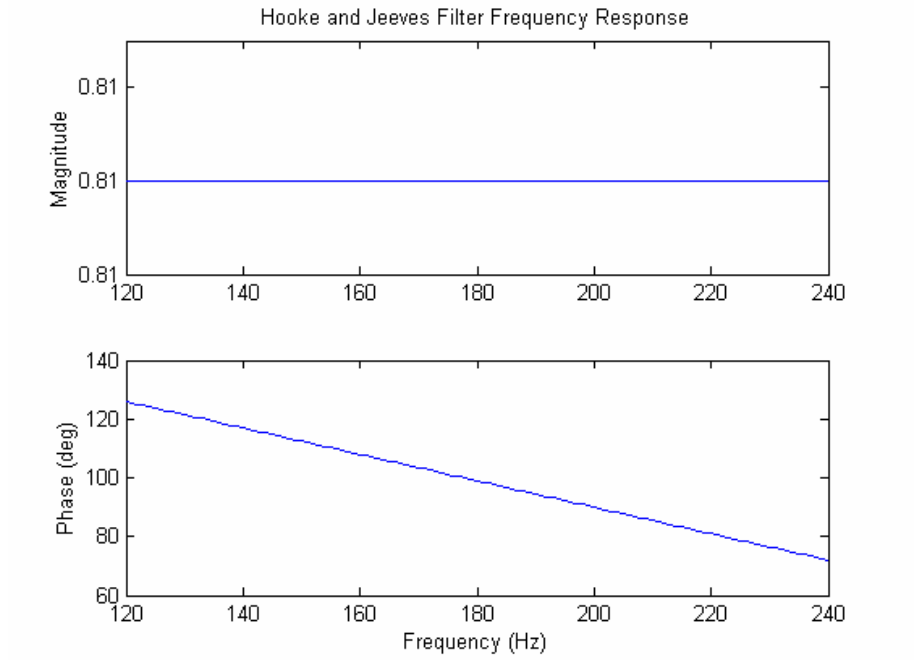

Figure C.8 Frequency response of steady-state Hooke and Jeeves filter

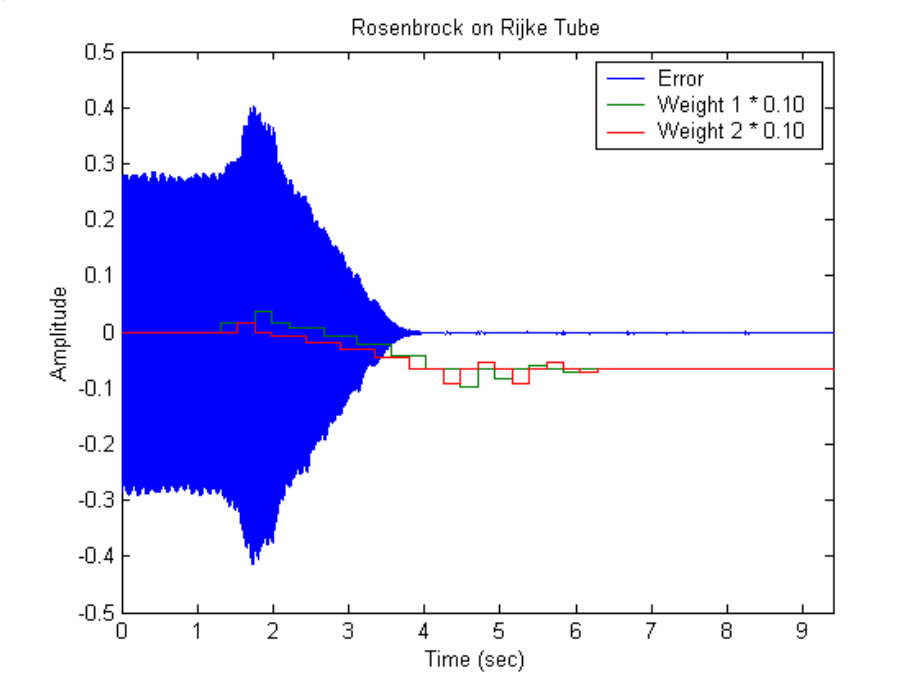

Figure C.9 Response envelope of Rijke Tube and filter weights for Rosenbrock algorithm

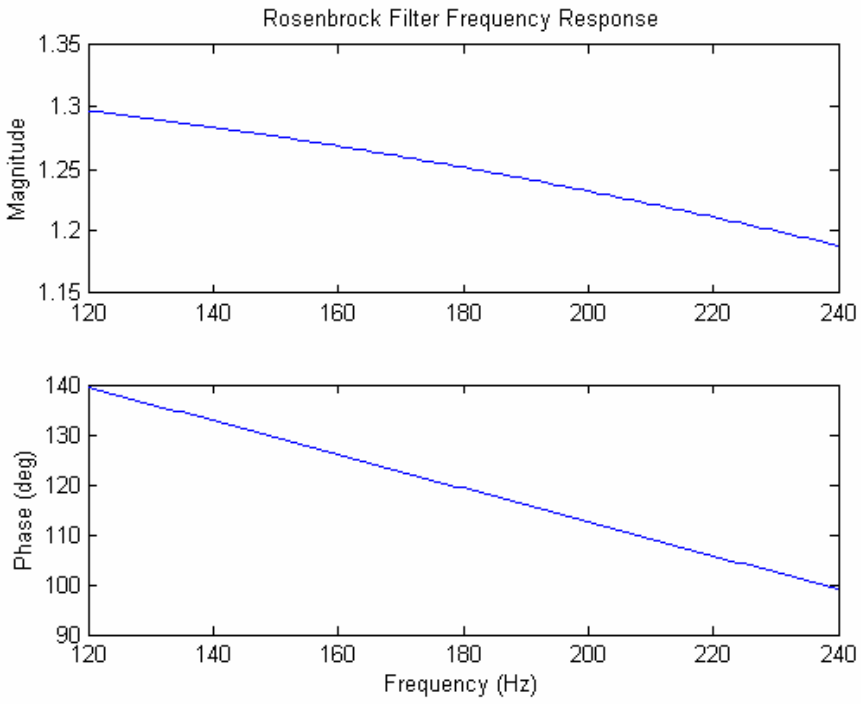

Figure C.10 Frequency response of steady-state Rosenbrock filter

Appendix D Rijke Tube High Φ Results

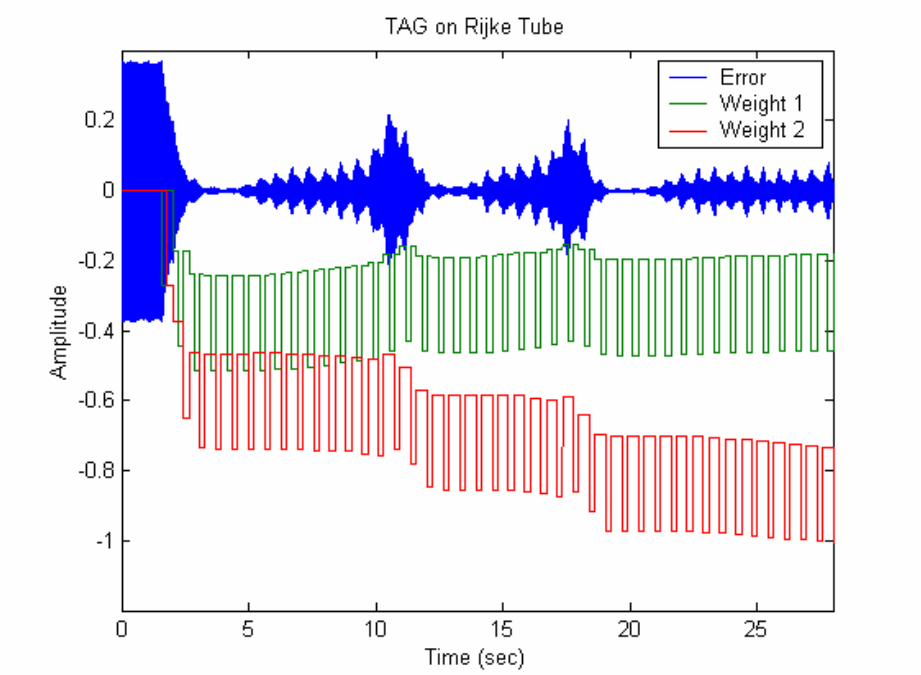

Figure D.1 Response envelope of Rijke Tube and filter weights for TAG algorithm

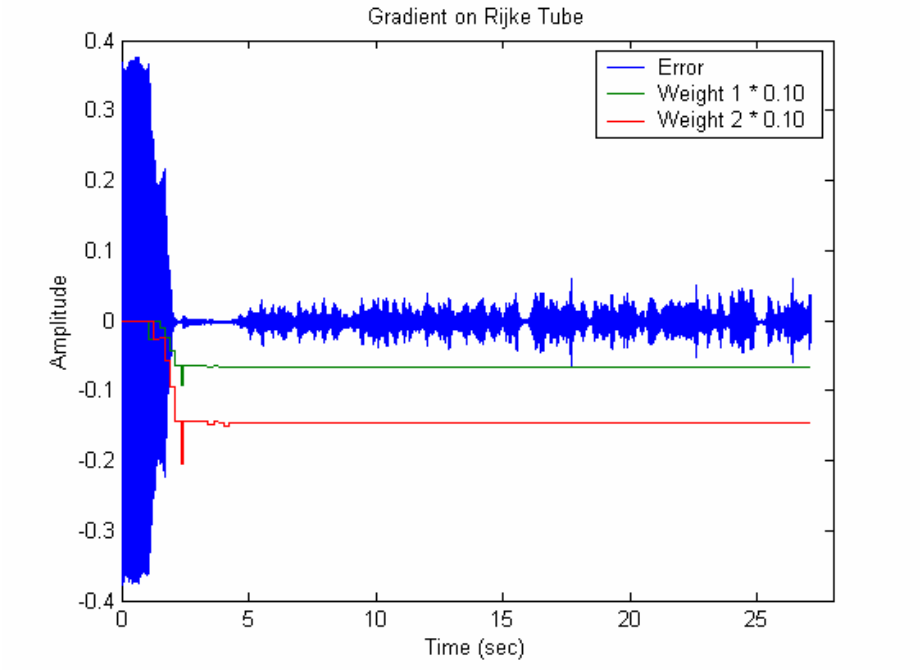

Figure D.2 Response envelope of Rijke Tube and filter weights for Gradient algorithm

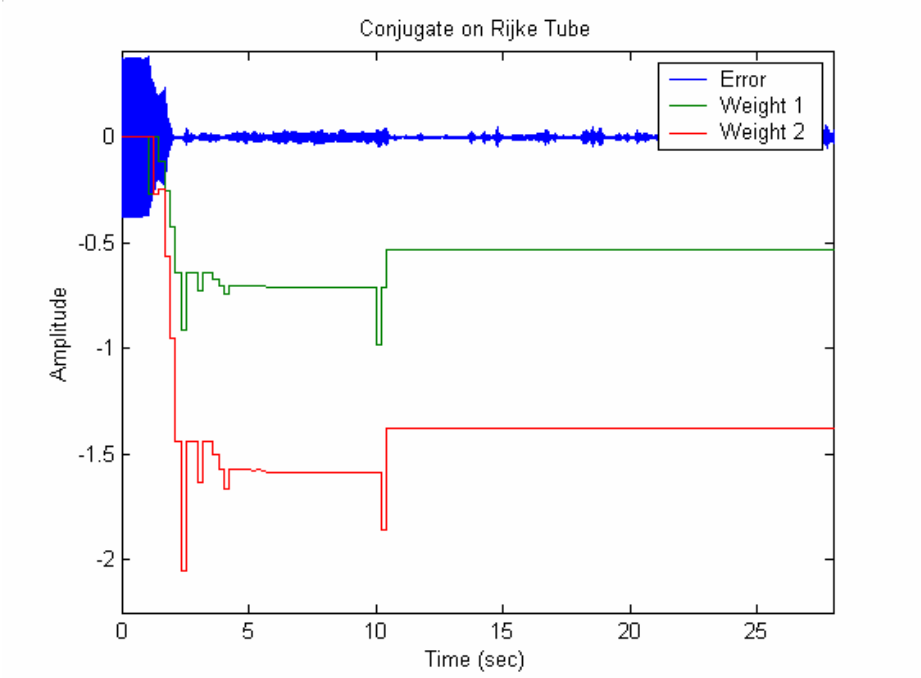

Figure D.3 Response envelope of Rijke Tube and filter weights for Conjugate algorithm

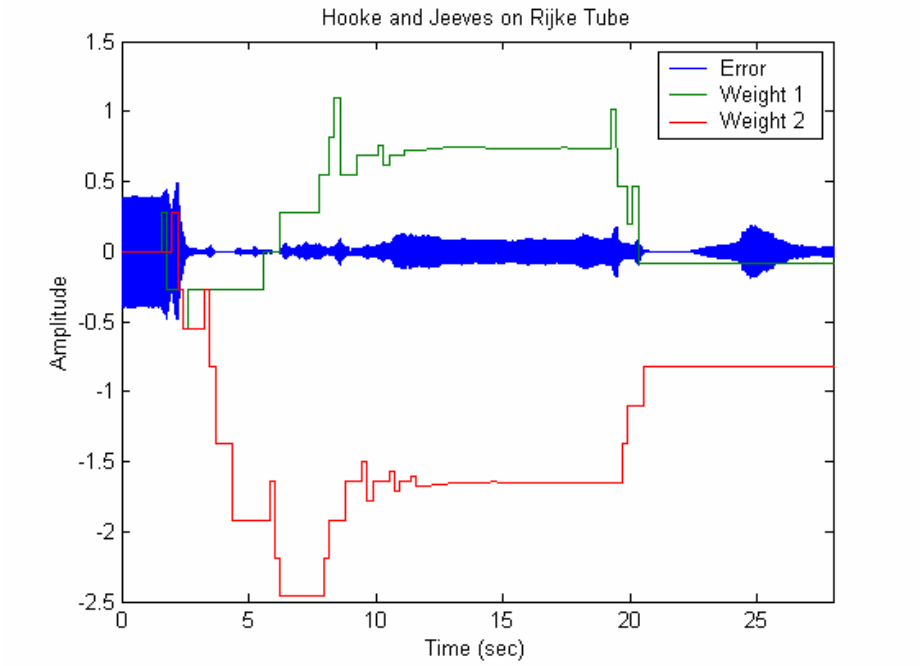

Figure D.4 Response envelope of Rijke Tube and filter weights for Hooke and Jeeves algorithm

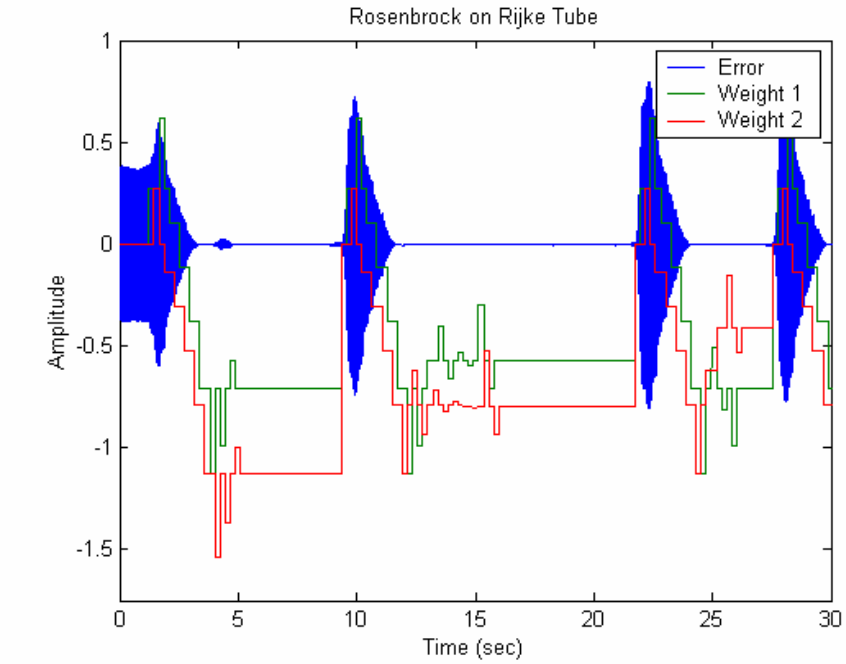

Figure D.5 Response envelope of Rijke Tube and filter weights for Rosenbrock algorithm

Appendix E Sub-harmonic Rijke Tube Results

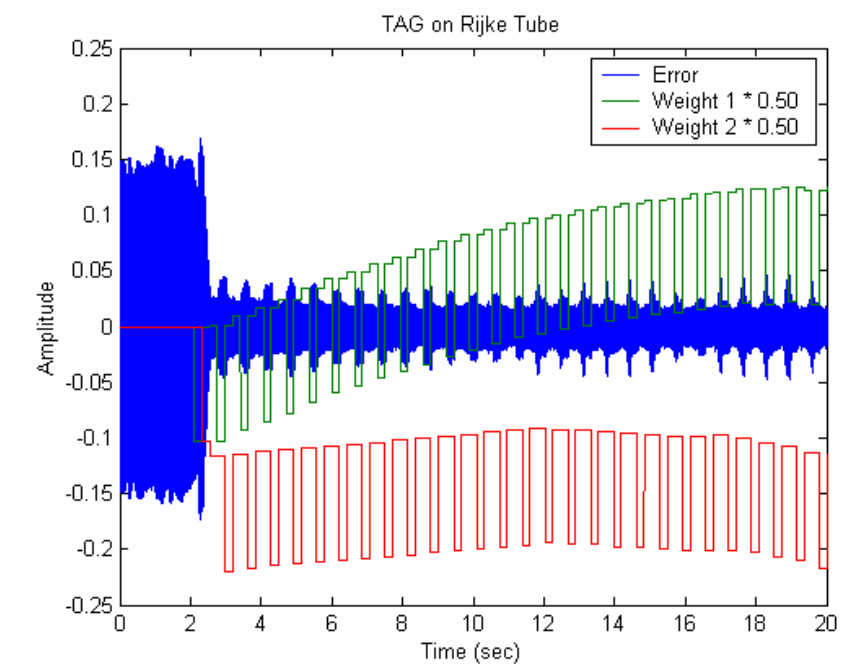

Figure E.1 Response and filter weights for TAG algorithm with pulsed actuation

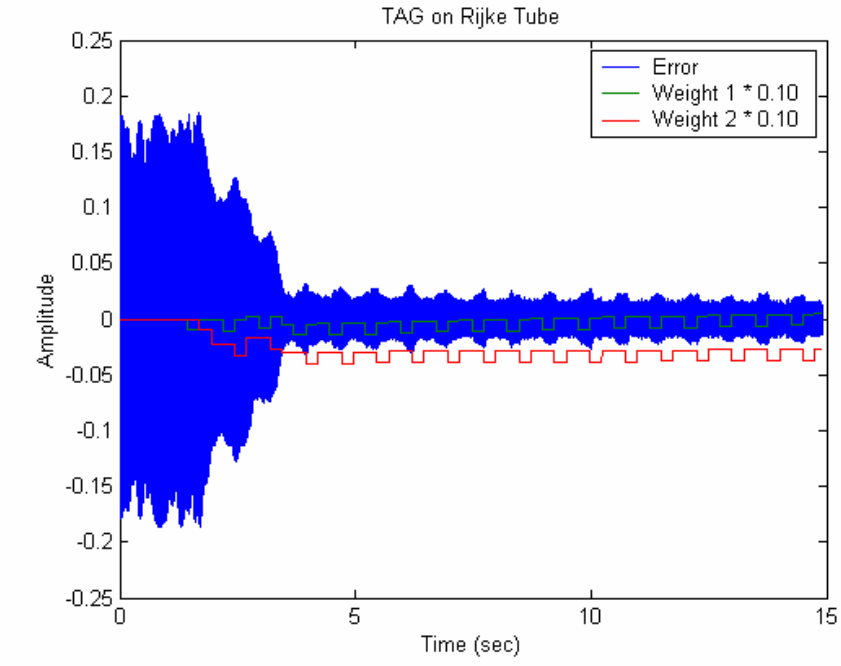

Figure E.2 Response and filter weights for TAG algorithm with 2nd sub-harmonic pulsed actuation

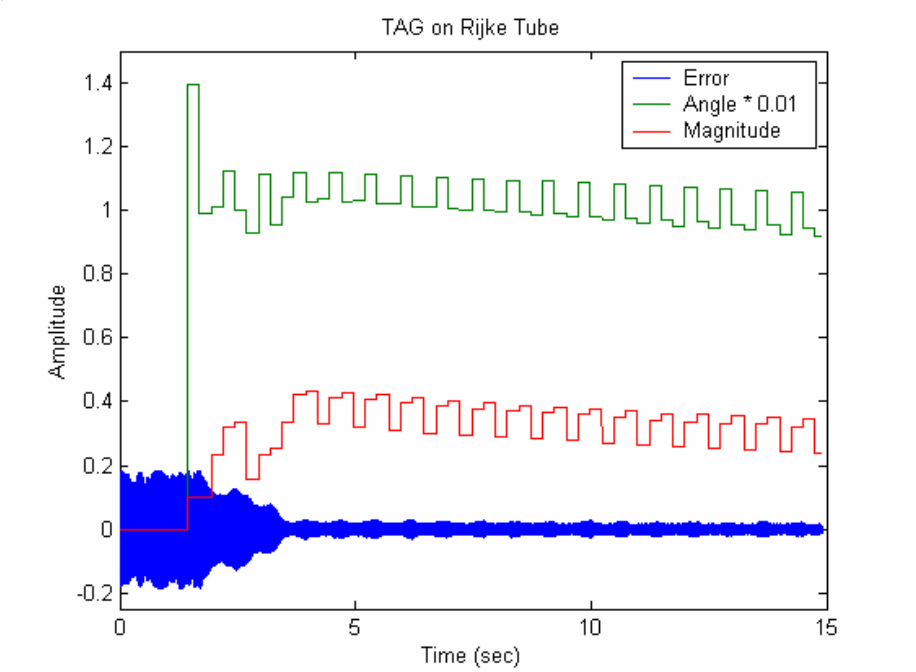

Figure E.3 Phase and magnitude of filter for TAG algorithm with 2nd sub-harmonic pulsed actuation

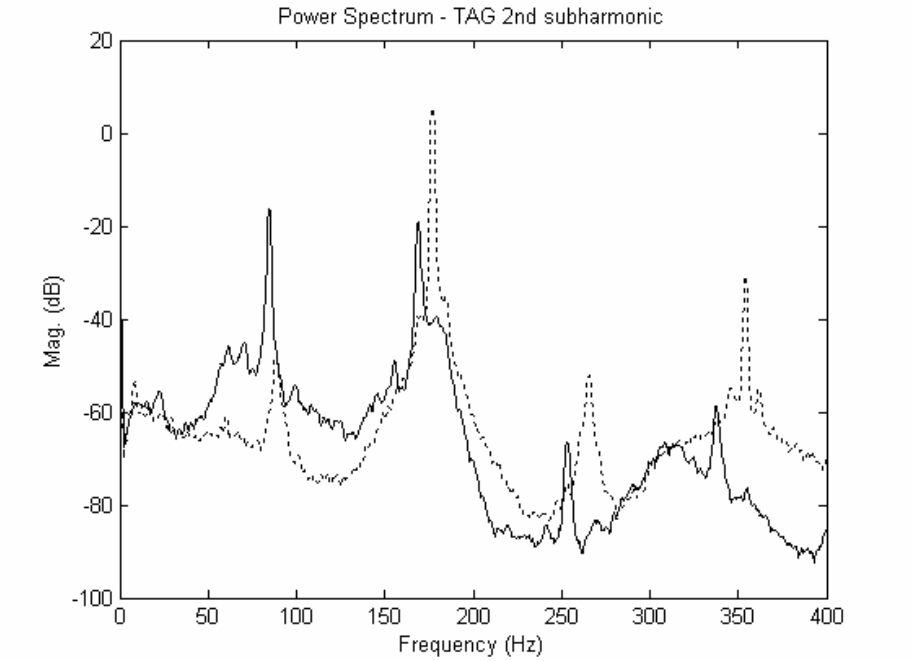

Figure E.4 Power spectrum using TAG with 2nd sub-harmonic pulsed actuation

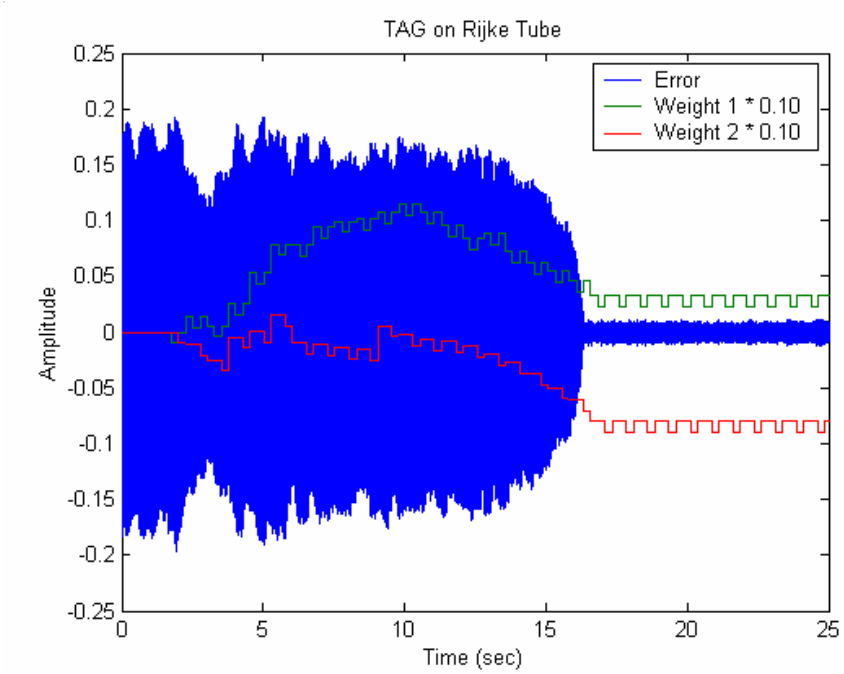

Figure E.5 Response and filter weights for TAG algorithm with 3rd sub-harmonic pulsed actuation

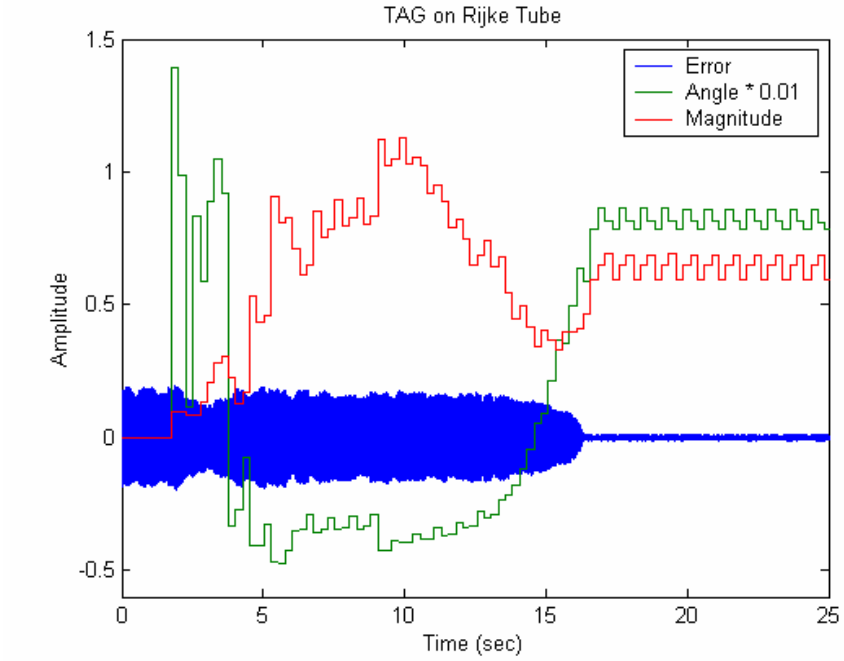

Figure E.6 Phase and magnitude of filter for TAG algorithm with 3rd sub-harmonic pulsed actuation

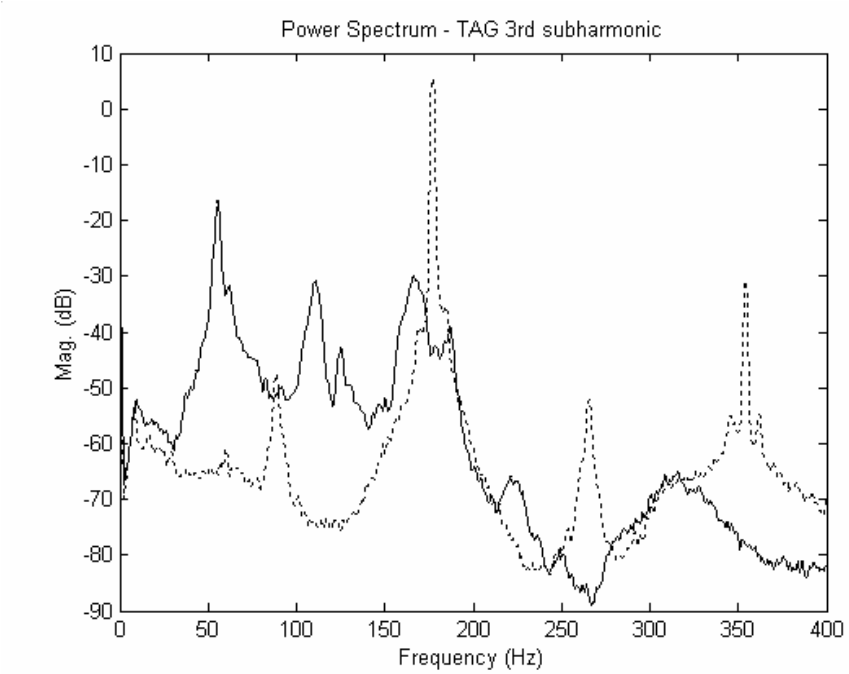

Figure E.7 Power spectrum using TAG with 3rd sub-harmonic pulsed actuation

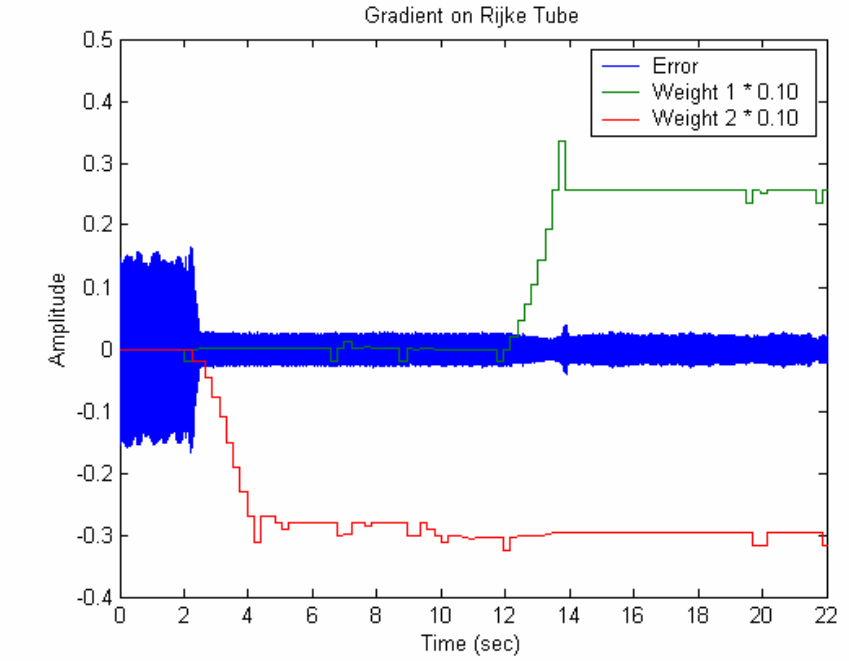

Figure E.8 Response and filter weights for Gradient algorithm with pulsed actuation

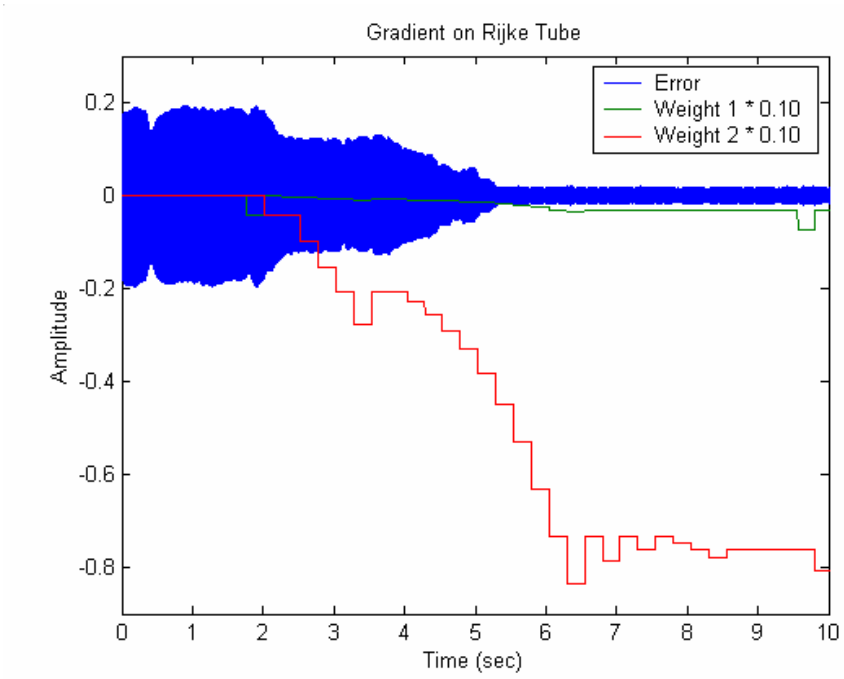

Figure E.9 Response and filter weights for Gradient algorithm with 2nd sub-harmonic pulsed actuation

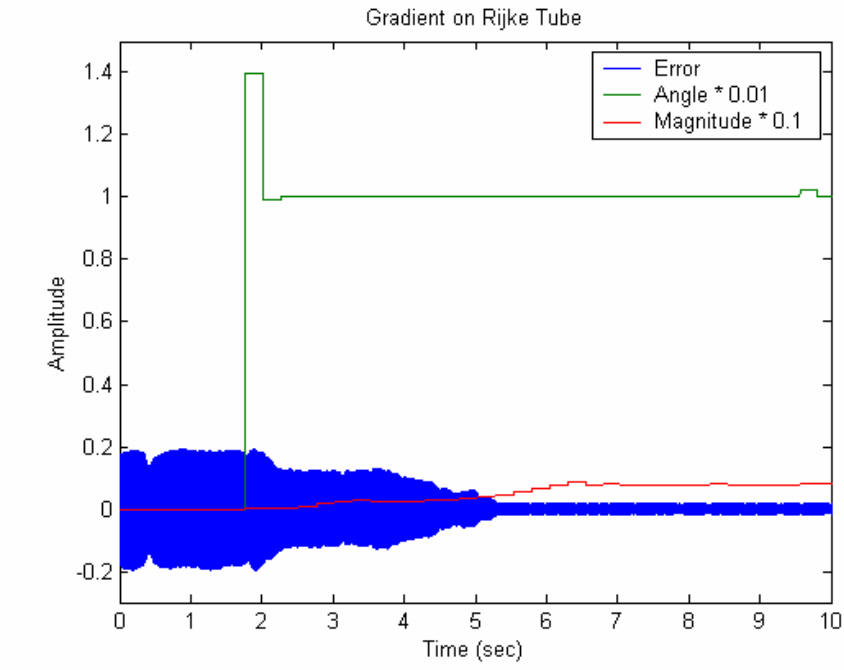

Figure E.10 Phase and magnitude of filter for Gradient algorithm with 2nd sub-harmonic pulsed actuation

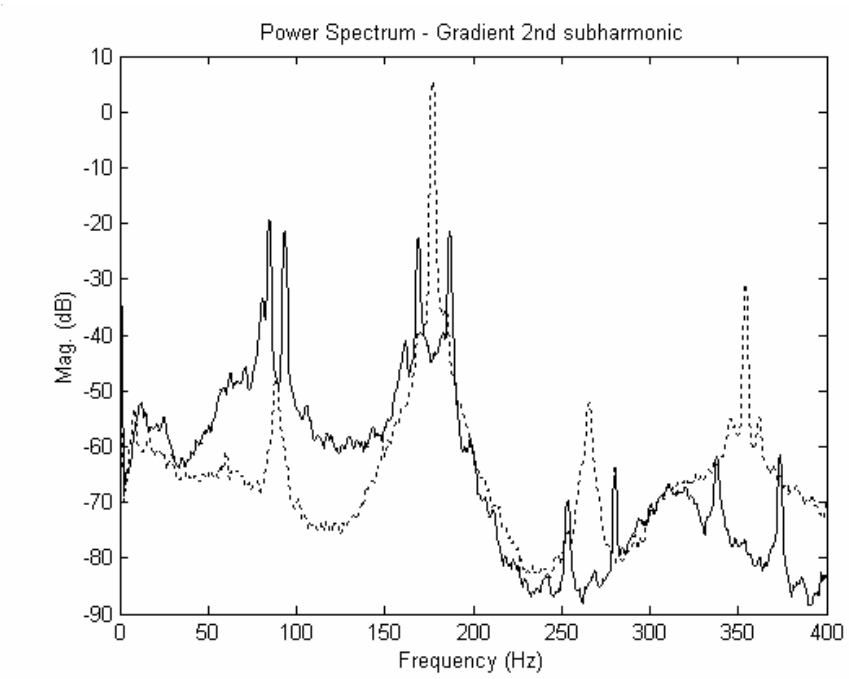

Figure E.11 Power spectrum using Gradient with 2nd sub-harmonic pulsed actuation

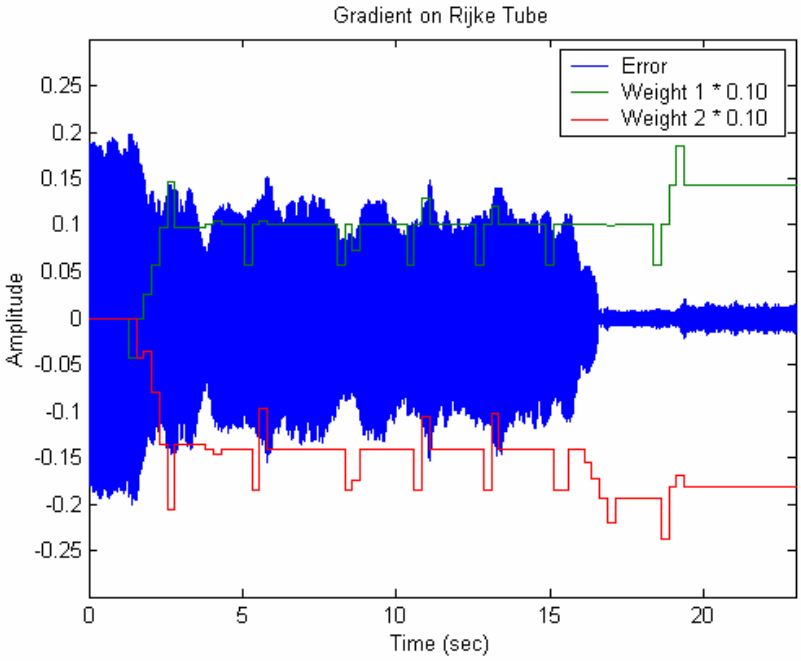

Figure E.12 Response and filter weights for Gradient algorithm with 3rd sub-harmonic pulsed actuation

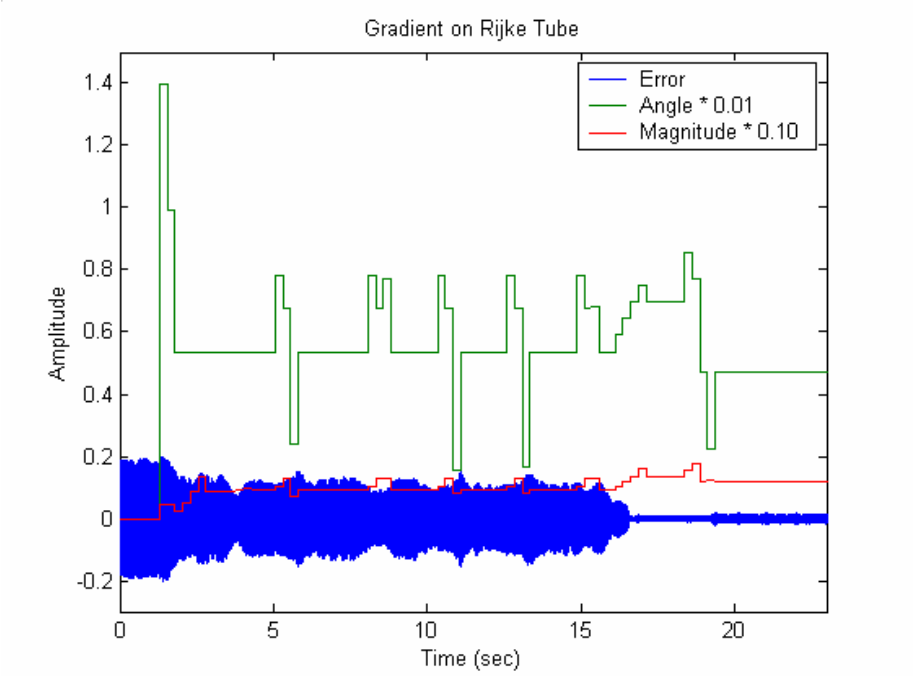

Figure E.13 Phase and magnitude of filter for Gradient algorithm with 3rd sub-harmonic pulsed actuation

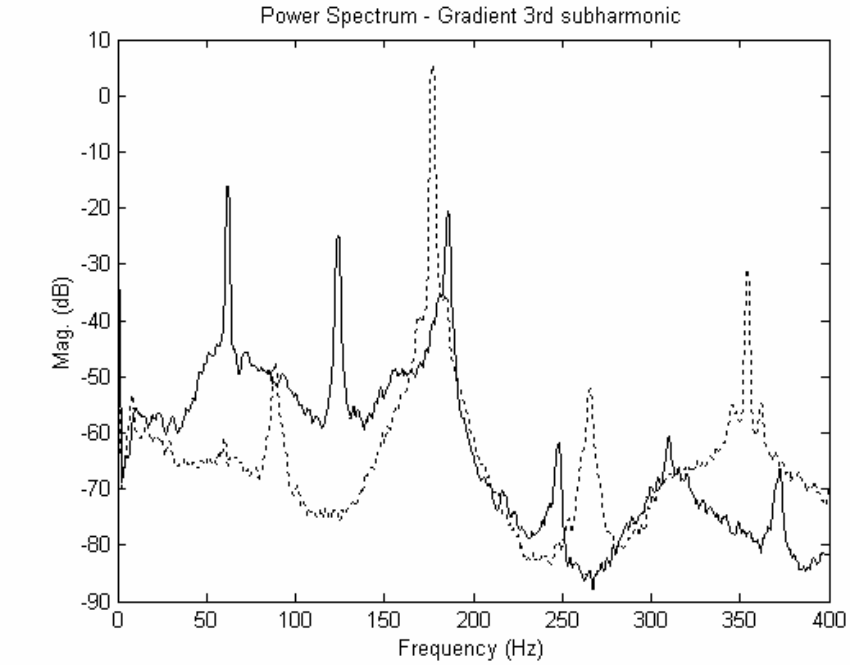

Figure E.14 Power spectrum using Gradient with 3rd sub-harmonic pulsed actuation

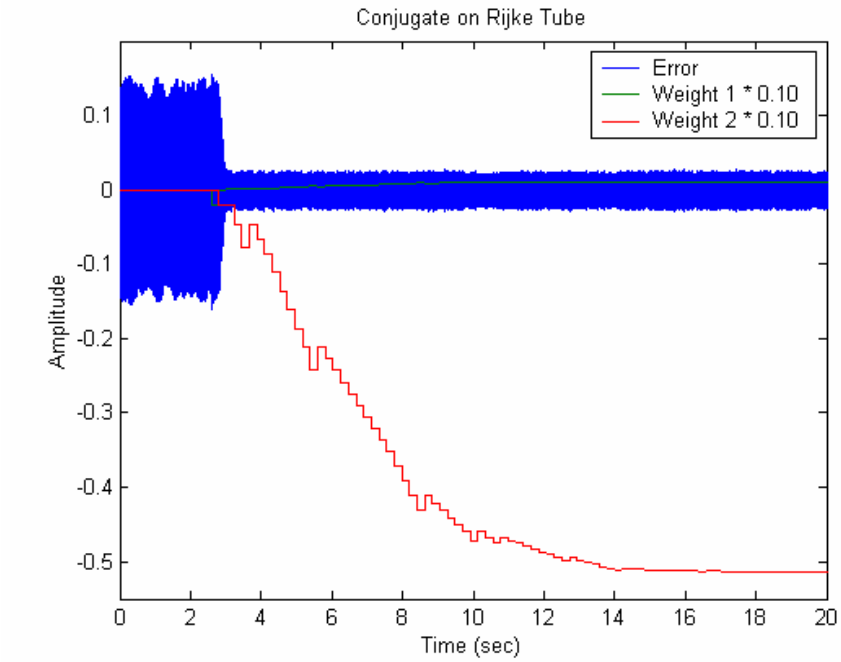

Figure E.15 Response and filter weights for Conjugate algorithm with pulsed actuation

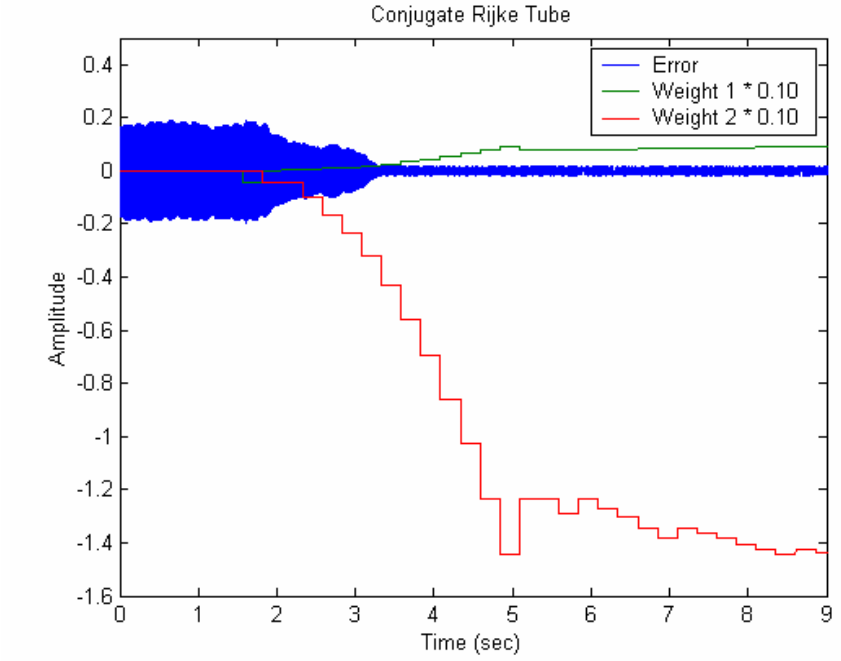

Figure E.16 Response and filter weights for Conjugate algorithm with 2nd sub-harmonic pulsed actuation

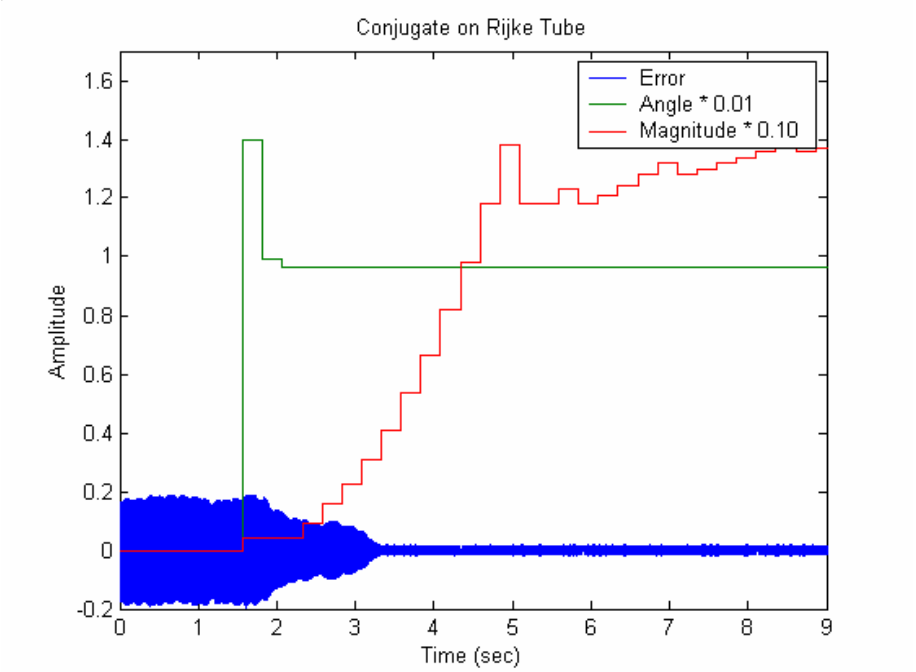

Figure E.17 Phase and magnitude of filter for Conjugate algorithm with 2nd sub-harmonic pulsed actuation

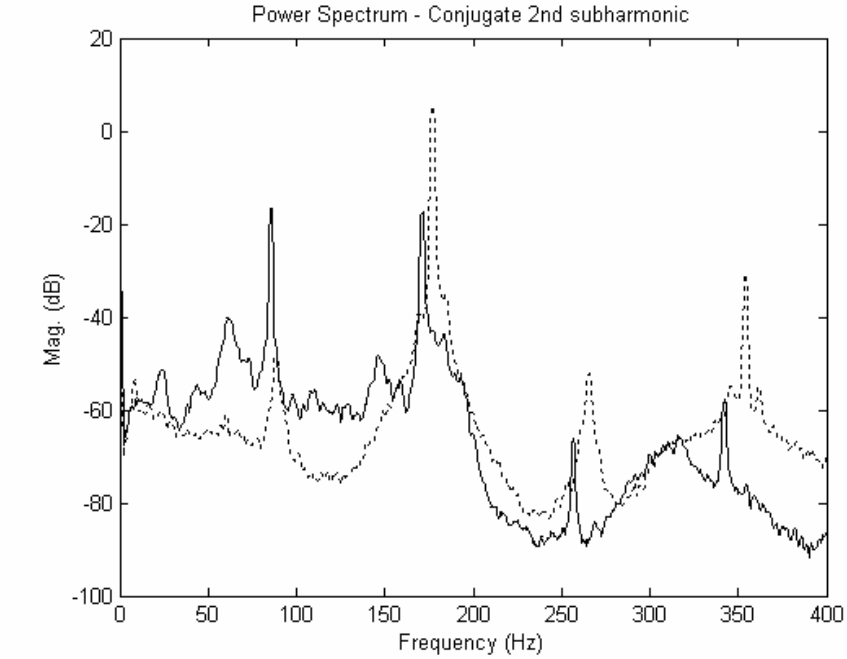

Figure E.18 Power spectrum using Conjugate with 2nd sub-harmonic pulsed actuation

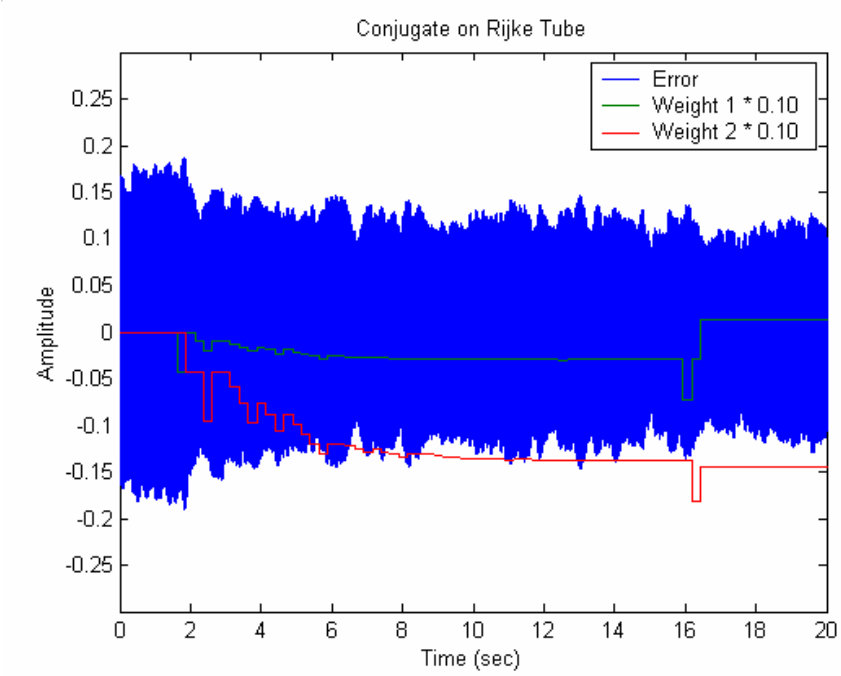

Figure E.19 Response and filter weights for Conjugate algorithm with 3rd sub-harmonic pulsed actuation

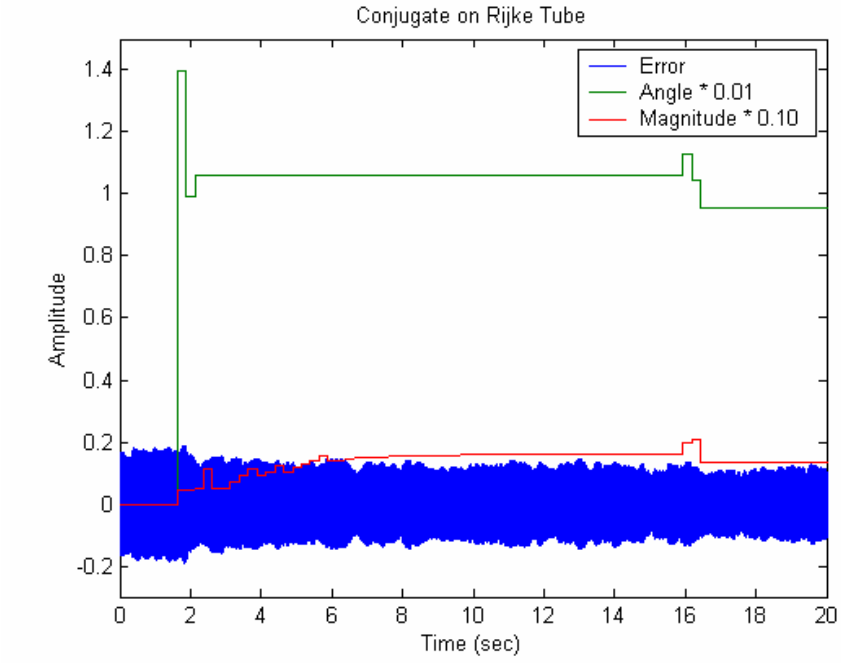

Figure E.20 Phase and magnitude of filter for Conjugate algorithm with 3rd sub-harmonic pulsed actuation

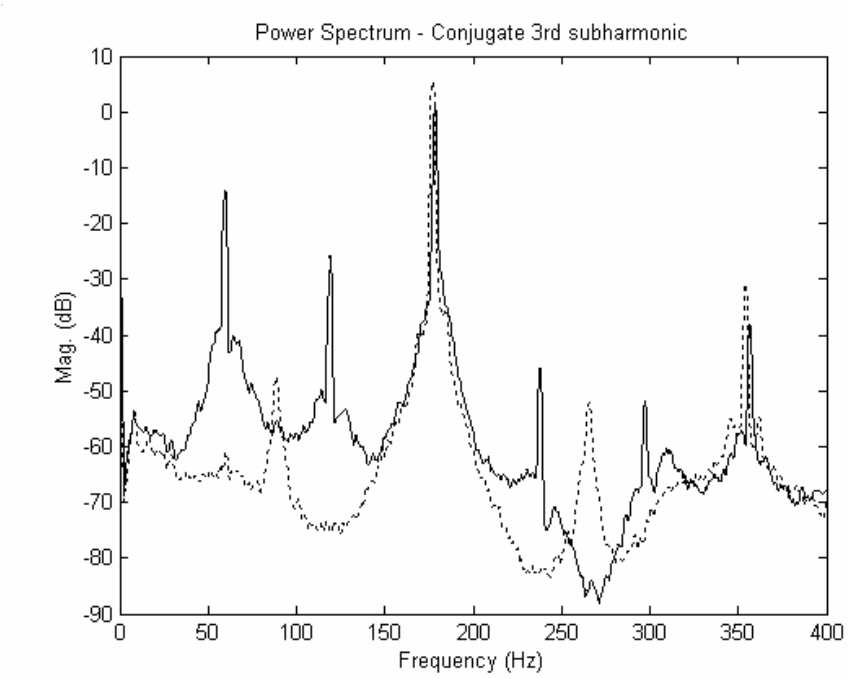

Figure E.21 Power spectrum using Conjugate with 3rd sub-harmonic pulsed actuation

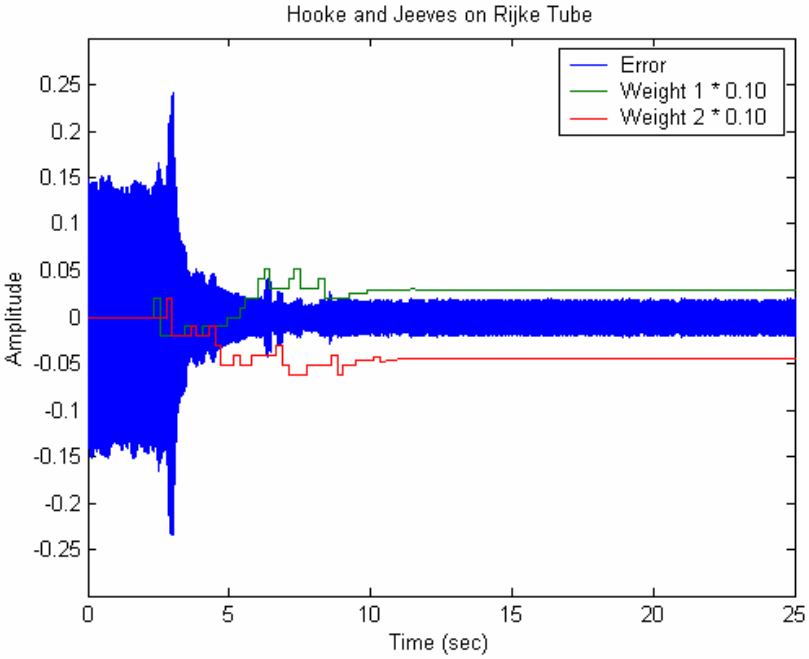

Figure E.22 Response and filter weights for Hooke and Jeeves algorithm with pulsed actuation

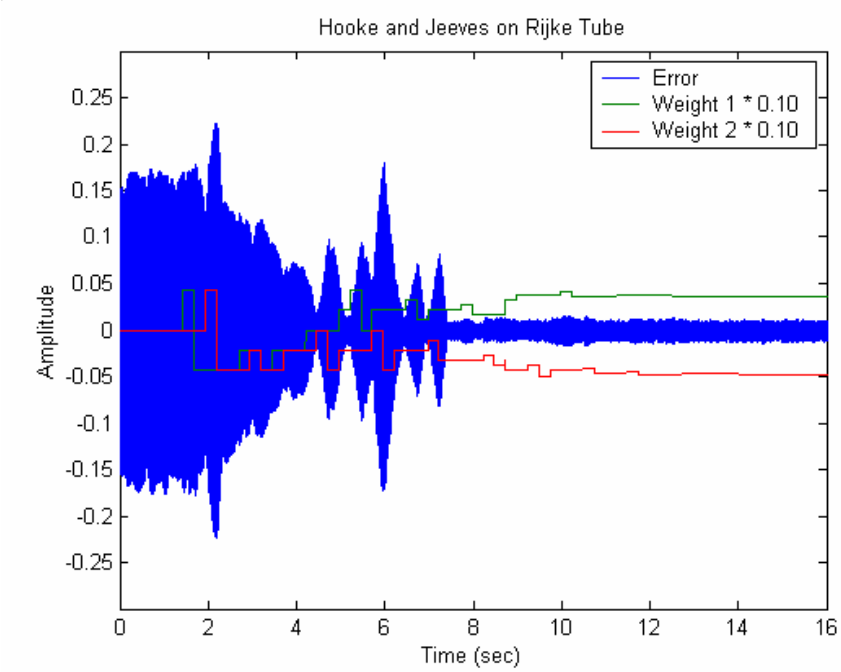

Figure E.23 Response and filter weights for Hooke and Jeeves algorithm with 2nd sub-harmonic pulsed actuation

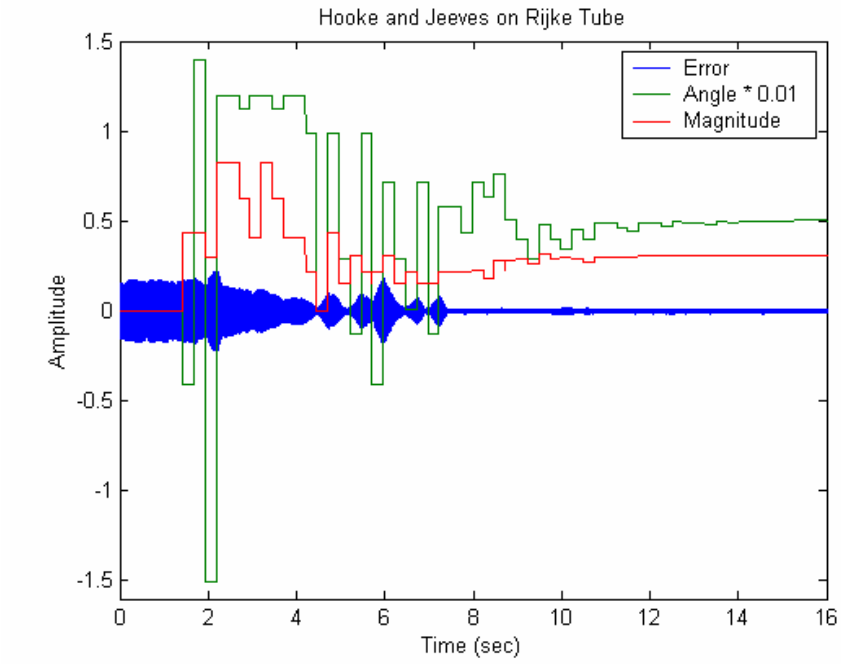

Figure E.24 Phase and magnitude of filter for Hooke and Jeeves algorithm with 2nd sub-harmonic pulsed actuation

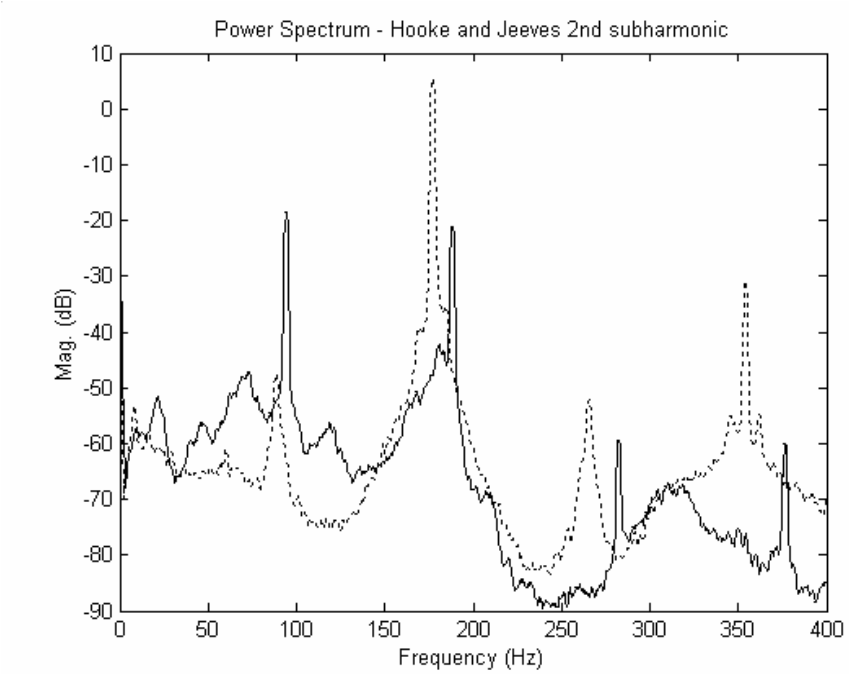

Figure E.25 Power spectrum using Hooke and Jeeves with 2nd sub-harmonic pulsed actuation

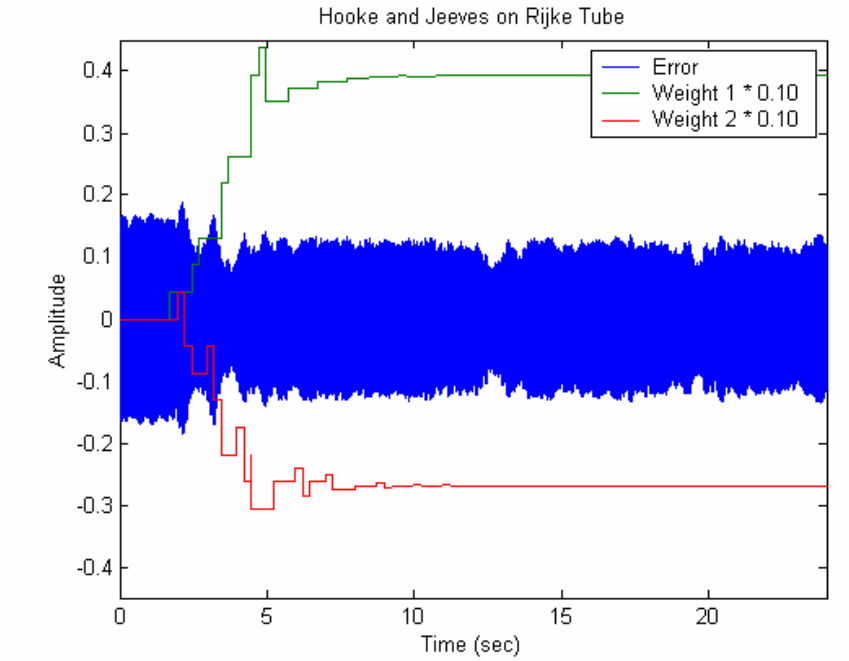

Figure E.26 Response and filter weights for Hooke and Jeeves algorithm with 3rd sub-harmonic pulsed actuation

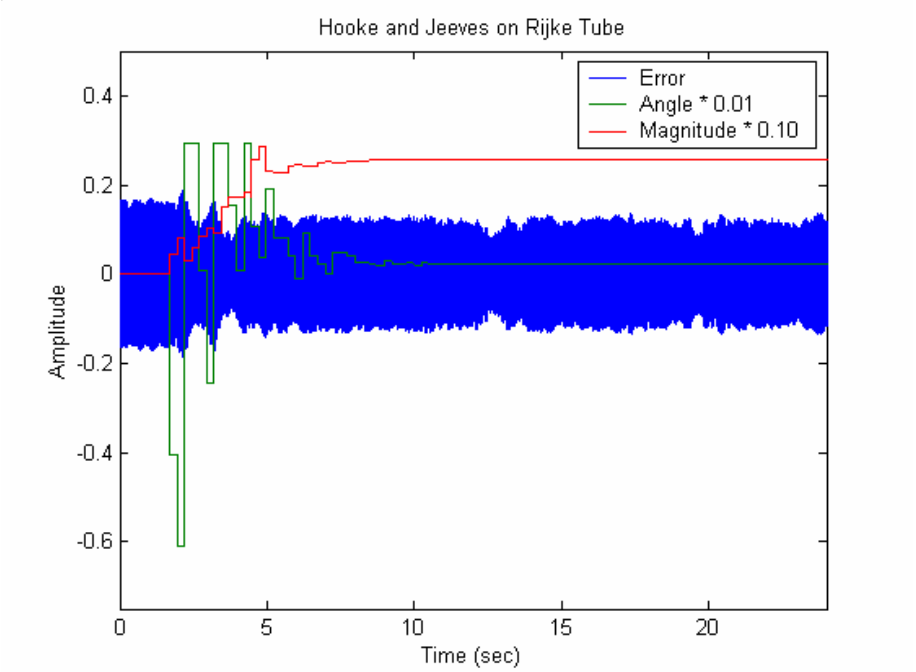

Figure E.27 Phase and magnitude of filter for Hooke and Jeeves algorithm with 3rd sub-harmonic pulsed actuation

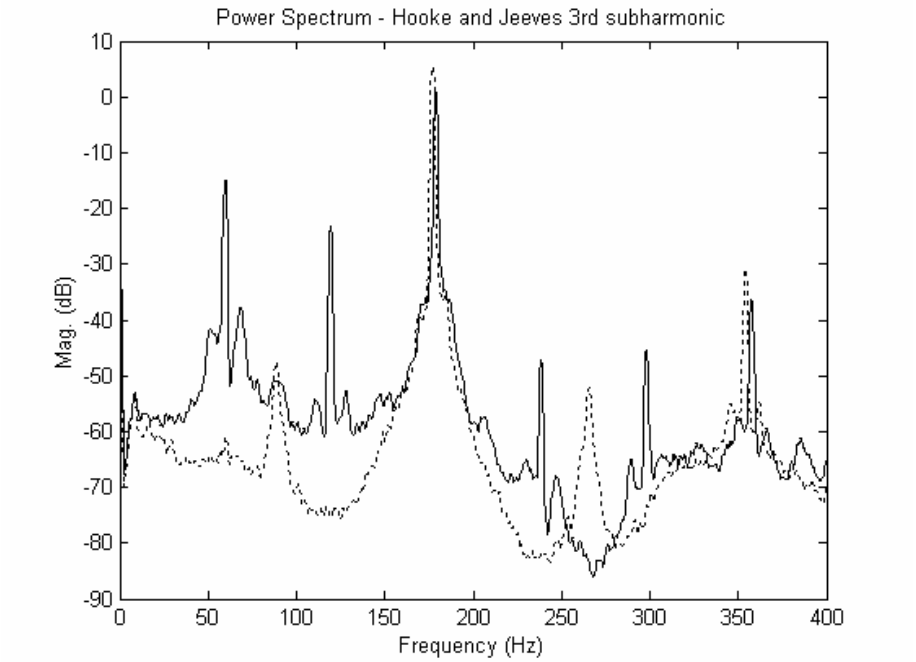

Figure E.28 Power spectrum using Hooek and Jeeves with 3rd sub-harmonic pulsed actuation

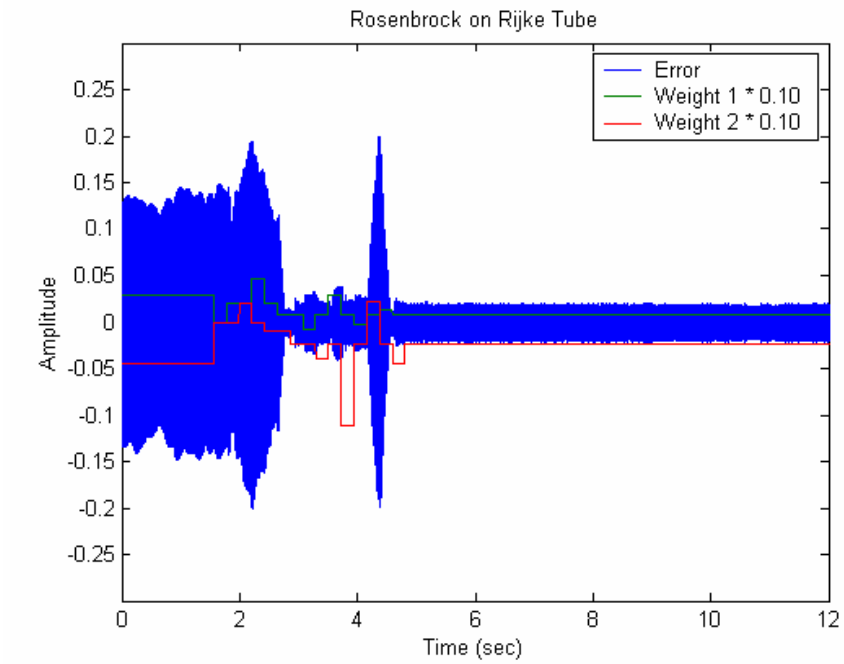

Figure E.29 Response and filter weights for Rosenbrock algorithm with pulsed actuation

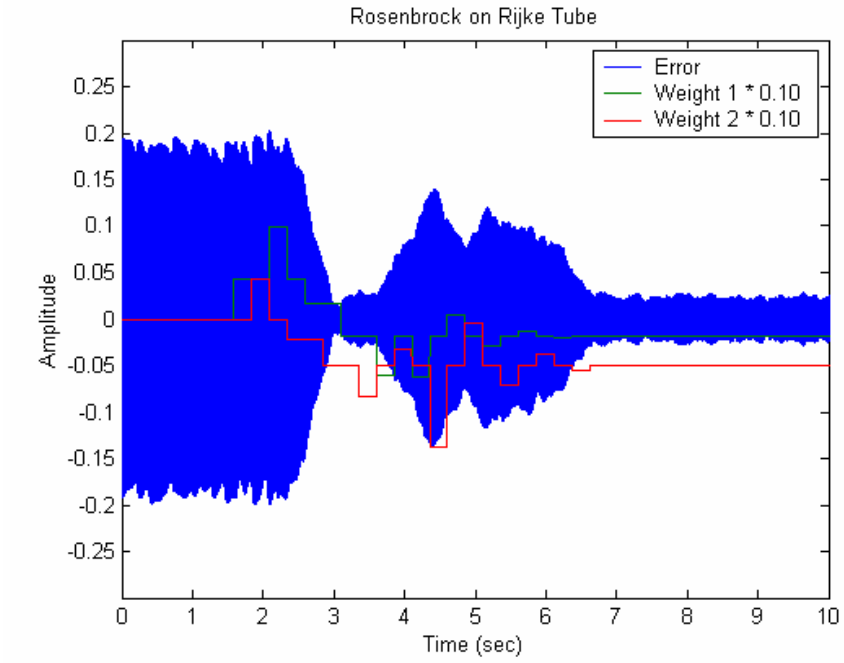

Figure E.30 Response and filter weights for Rosenbrock algorithm with 2nd sub-harmonic pulsed actuation

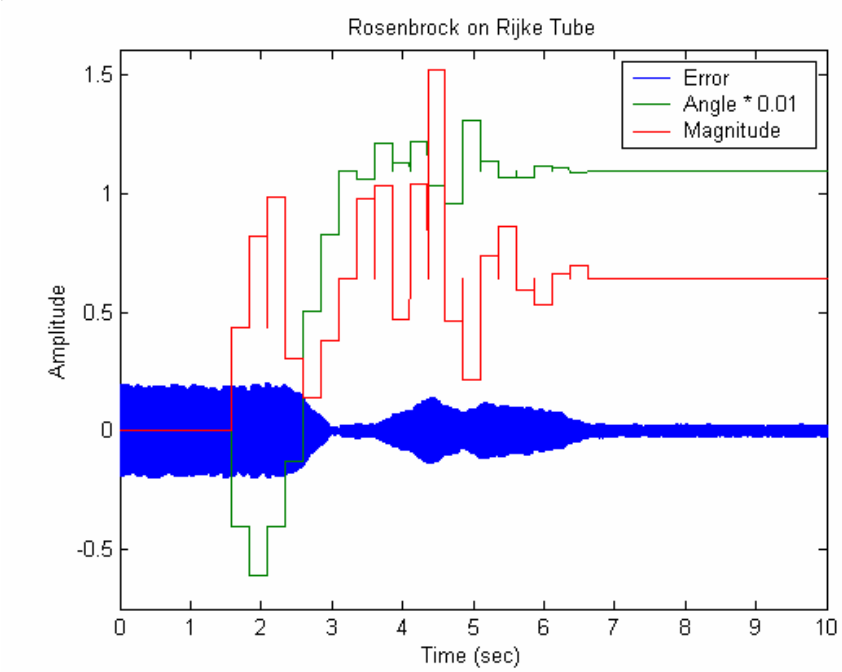

Figure E.31 Phase and magnitude of filter for Rosenbrock algorithm with 2nd sub-harmonic pulsed actuation

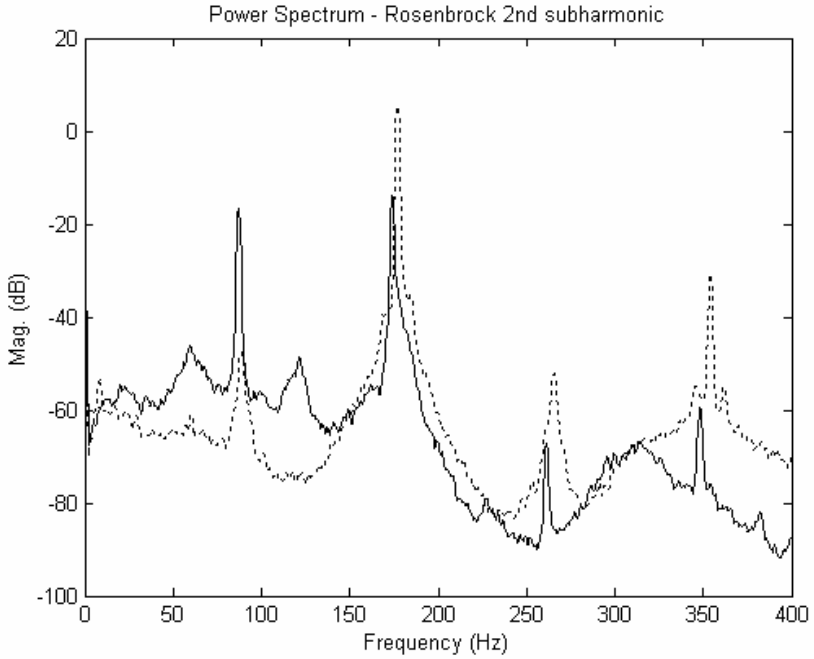

Figure E.32 Power spectrum using Rosenbrock with 2nd sub-harmonic pulsed actuation

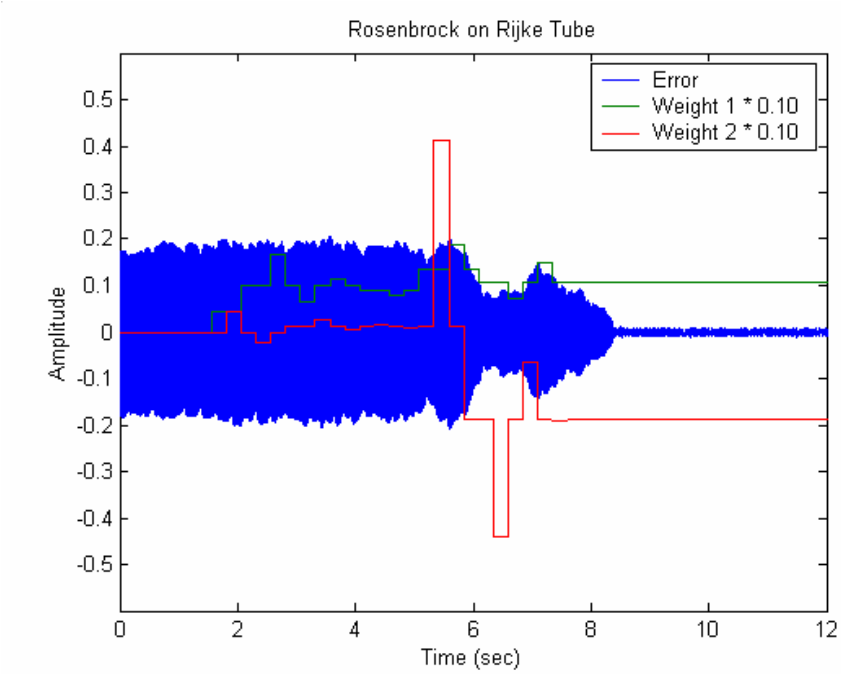

Figure E.33 Response and filter weights for Rosenbrock algorithm with 3rd sub-harmonic pulsed actuation

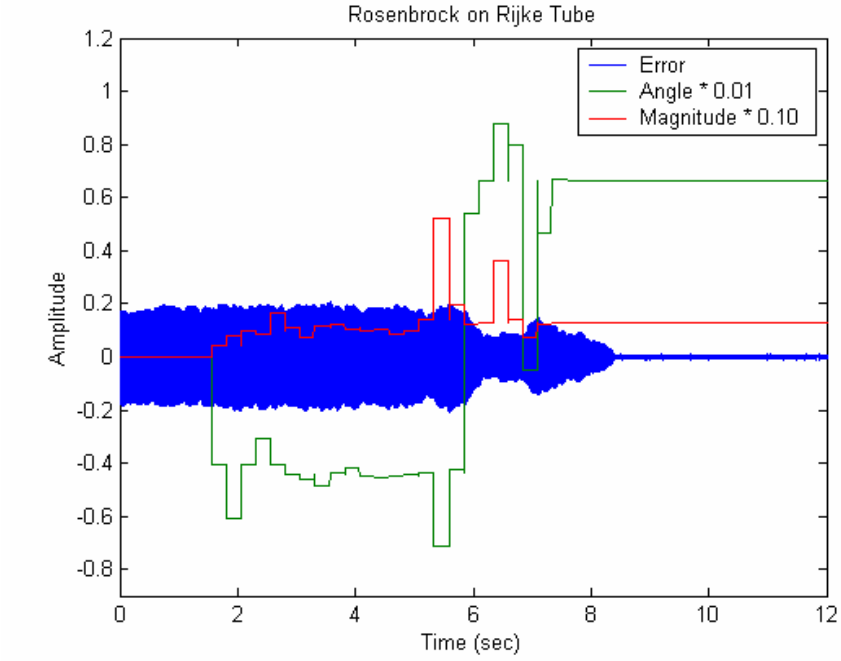

Figure E.34 Phase and magnitude of filter for Rosenbrock algorithm with 3rd sub-harmonic pulsed actuation

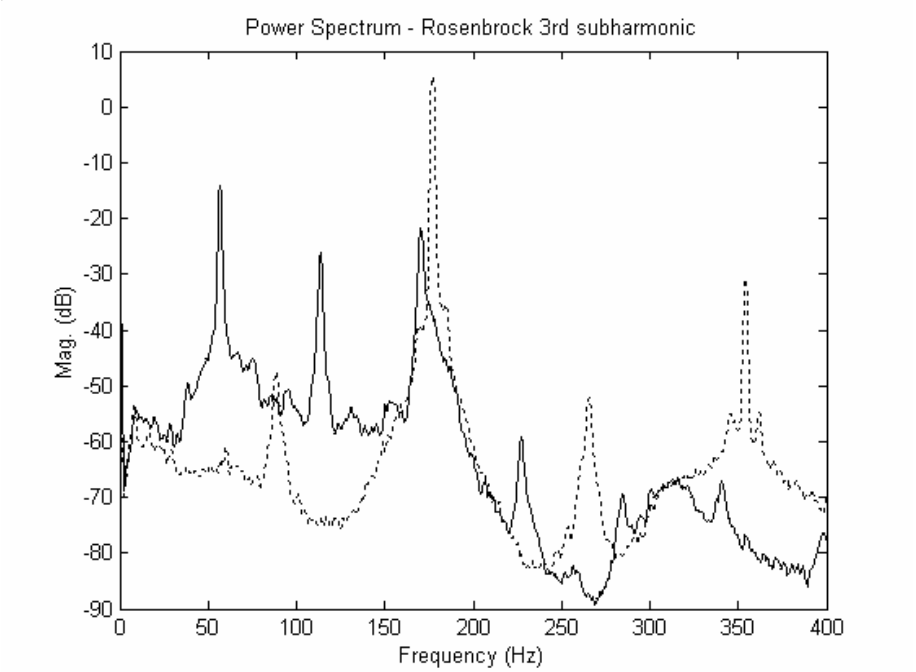

Figure E.35 Power spectrum using Rosenbrock with 3rd sub-harmonic pulsed actuation

Vita

Aaron Greenwood was born in Mount Clemons, Michigan on January 23, 1979. He graduated from Marysville High School in 1997. He received his Bachelor's Degree in Mechanical Engineering from Michigan Technological University in May of 2001. He began his Master's program in the summer of 2001 and successfully defended his thesis on February 5, 2003.